

Diss. ETH No: 26474

**Investigation of electronic structure at the
SrTiO₃/YBa₂Cu₃O_{7- δ} interface.**

A thesis submitted to attain the degree of
DOCTOR OF SCIENCES of ETH ZURICH
(Dr. sc. ETH Zurich)

presented by

Tornike Gagnidze

Msc Physics

Ivane Javakhishvili Tbilisi State University

born on January 22, 1991

citizen of Georgia

accepted on the recommendation of

Prof. Dr. Gian-Luca Bona, examiner

Dr. Dr. hc mult. Johannes Georg Bednorz, co-examiner

Prof. Dr. Hugo Keller, co-examiner

Prof. Dr. Alexander Shengelaya, co-examiner

Abstract

In-depth studies and investigations of interfaces between semiconductors and insulators resulted in a profound understanding of charge transport properties and led eventually to high performance, compact semiconductor devices. Moreover, in specific transition metal oxide heterostructures the electronic band structure allows for unexpected properties such as superconductivity. At the interface between a high-temperature superconductor (HTS) and a high dielectric constant (ϵ) material, the superconducting transition temperature (T_c) can be expected to increase due to the reduced Coulomb repulsion between localized clusters or stripes of charges.

In this thesis, we investigate interface phenomena between HTS $\text{YBa}_2\text{Cu}_3\text{O}_{7-\delta}$ (YBCO) and high- ϵ SrTiO_3 (STO). Epitaxial heterostructures of the two compounds were grown onto STO(001) substrates by the pulsed laser deposition technique. It is well known that YBCO thin films grown on STO show a drastic suppression of the superconducting transition temperature (T_c) for thicknesses below 15 nm. However, films grown in this investigation down to 10 unit cells (~ 11 nm) show consistently a drop of T_c from 90 K (bulk value) to about 86 K. This demonstrates the high quality crystal growth achieved in this work. Transmission electron microscopy (TEM) analysis, performed in our investigations, show that c-axis mismatch with substrate produces anti-phase boundary defects that could be responsible for a complete suppression of the superconducting phase in the first deposited layer. In the case of STO grown on top of the YBCO films, we observed a better quality interface, which then was investigated by soft-X-ray angle-resolved photo-emission spectroscopy (SX-ARPES) carried out at the

ADRESS synchrotron beamline of the Swiss light source at the Paul Scherrer Institute. Given the high photon energy of 800-900 eV, we could probe the electronic density of states of YBCO even in cases where the film was covered by several layers of STO (2 to 4 unit cells). The measured Fermi surfaces of the buried YBCO films show a change of symmetry compared to the bare films that can be explained by a 2 x 1 reconstruction, which takes place at the top interface. Moreover, X-ray absorption and resonant photo-emission spectroscopy across the Ti L_{2,3} edge show modification of the Ti electronic states at this interface which can be assigned as well to a 2x1 structural reconstruction. We propose that this is a general property of high- ϵ STO grown on charged surfaces, in which a distortion of the oxygen octahedron in the unit cell may compensate for the polar mismatch. Our investigations with SX-ARPES open a path-way to study electronic band states of epitaxial interfaces. All YBCO/STO heterostructures presented in this thesis were grown on TiO₂ terminated STO(001) substrates. We also investigate the possibility to use a different chemical termination by depositing a single layer of SrO onto the TiO₂ surface of STO. We performed the surface morphology and crystal structure analysis of SrO epitaxial ultrathin films ranging from 1 to about 25 layers. X-ray diffraction and transmission electron microscopy analysis reveal that SrO grows along the [111] direction with a 4% out-of-plane elongation. We found that the distance between the TiO₂ plane and the first deposited SrO layer is 0.27 nm, a value which is about 40% larger than in bulk STO. We demonstrate that a single SrO deposited layer has a different morphology compared to an ideal atomically flat chemical termination. The results show that by careful engineering of the deposition conditions with monolayer accuracy high quality heterostructures in transition metal oxides can be achieved.

Zusammenfassung

Detaillierte Untersuchungen der Grenzflächen zwischen Halbleitern und Isolatoren führten zu einem tiefen Verständnis der Ladungstransporteigenschaften und schliesslich zu hochleistungsfähigen, kompakten Halbleiterbauelementen. Darüber hinaus ermöglicht die elektronische Bandstruktur in spezifischen Übergangsmetall-oxid-Heterostrukturen unerwartete Eigenschaften wie etwa die Supraleitung. An der Grenzfläche zwischen einem Hochtemperatur-Supraleiter (HTS) und einem Material mit hoher Dielektrizitätskonstante (ϵ) ist ein Anstieg der supraleitenden Übergangstemperatur (T_c) zu erwarten, da die Coulomb-Abstoßung zwischen lokalisierten Ladungsgruppen oder -streifen reduziert wird.

In dieser Arbeit untersuchen wir Grenzflächenphänomene zwischen HTS $\text{YBa}_2\text{Cu}_3\text{O}_{7-\delta}$ (YBCO), und mit hoher Dielektrizitätskonstante ϵ SrTiO_3 (STO). Die epitaktischen Heterostrukturen der beiden Verbindungen wurden mittels gepulster Laserabscheidung auf $\text{STO}(001)$ -Substrate aufgewachsen. Es ist bekannt, dass die auf STO aufgewachsenen YBCO-Dünnschichten eine drastische Unterdrückung der supraleitenden Übergangstemperatur (T_c) bei Schichtdicken unter 15 nm zeigen. Jedoch weisen Filme, die in dieser Untersuchung bis hinunter zu 10 Einheitszellen (~ 11 nm) gezüchtet wurden, durchweg einen Abfall der T_c -Werte von 90 K (Volumenwert) auf etwa 86 K auf. Dies zeigt, dass in dieser Arbeit erreichte qualitativ hochwertige Kristallwachstum. Die in unseren Untersuchungen durchgeführte Analyse mittels Transmissionselektronenmikroskopie (TEM) zeigt, dass eine Fehlanpassung der c-Achse an das Substrat gegenphasige Grenzdefekte erzeugt, die für eine vollständige Unterdrückung der supraleitenden Phase in der ersten abgeschiedenen Schicht verantwortlich sein könnten. Im Fall von STO,

das auf YBCO-Filmen aufgewachsen ist, beobachteten wir eine qualitativ bessere Grenzfläche, die dann mit der winkelaufgelösten Lichtemissionsspektroskopie mit weicher Röntgenstrahlung (SX-ARPES) untersucht wurde, die an der ADRESS Synchrotronstrahllinie am Paul Scherrer Institut durchgeführt wurde. Angesichts der hohen Photonenenergie von 800-900 eV können wir die elektronische Zustandsdichte von YBCO selbst in Fällen untersuchen, in denen der Film von mehreren Schichten STO (2 bis 4 Einheitszellen) bedeckt war. Die gemessenen Fermi-Flächen der vergrabenen YBCO-Filme zeigen im Vergleich zu den nackten Filmen eine Symmetrieänderung, die sich durch eine 2×1 -Rekonstruktion erklären lässt, welche an der oberen Grenzfläche stattfindet. Darüber hinaus zeigt die Röntgenabsorptions- und die resonante Photoemissionsspektroskopie über die Ti L_{2,3}-Kante eine Veränderung der elektronischen Ti-Zustände an dieser Grenzfläche, die ebenfalls einer 2×1 -Strukturrekonstruktion zugeordnet werden kann. Wir interpretieren dies, als eine allgemeine Eigenschaft von STO mit hohem ϵ , wobei eine Verzerrung des Sauerstoff-Oktaeders in der Einheitszelle die polare Fehlanpassung ausgleichen kann. Unsere Untersuchungen mit SX-ARPES eröffnen einen neuen Weg zur Untersuchung der elektronischen Bandzustände von epitaktischen Grenzflächen. Alle in dieser Arbeit vorgestellten YBCO/STO-Heterostrukturen wurden auf TiO₂-terminiertem STO(001)-Substrat aufgewachsen. Wir haben auch die Möglichkeit untersucht eine andere chemische Terminierung zu verwenden, indem wir eine einzelne Schicht SrO auf die TiO₂-Oberfläche von STO aufbringen. Wir haben deren Oberflächenmorphologie bestimmt und die Kristallstrukturanalyse von epitaktischen SrO-Dünnschichten von 1 bis etwa 25 Lagen durchgeführt. Die Analyse der Röntgenbeugung und der Transmissionselektronenmikroskopie zeigt, dass SrO entlang der [111] Richtung mit einer Dehnung von 4% ausserhalb der Ebene wächst. Wir messen, dass in unseren Filmen der Abstand zwischen der TiO₂-Ebene und der ersten abgeschiedenen SrO-Schicht 0,27 nm beträgt, ein Wert, der etwa 40% größer ist als in STO-Kristallen. Wir zeigen, dass eine einzelne SrO-Abscheidungsschicht eine andere Morphologie aufweist als ein idealer, atomar flacher chemischer Abschluss. Die Ergebnisse zeigen, dass durch sorgfältige Optimierung der Abscheidungsbedingungen mit atomarer Schichtpräzision qualitativ hochwertige Heterostrukturen

in Übergangsmetalloxiden erzielt werden können.

List of Acronyms

Materials:

STO: SrTiO₃

YBCO: YBa₂Cu₃O_{7-d}

SRO: SrRuO₃

LAO: LaAlO₃

LSCO: La_{2-x}Sr_xCuO₄

Experimental Techniques:

AFM: Atomic force microscopy

ARPES: Angle-resolved photoelectron spectroscopy

PES: Photoelectron spectroscopy

PLD: Pulsed laser deposition

PPMS: Physical properties measurement system

RHEED: Reflection high-energy electron diffraction

ResPES: Resonant photoelectron spectroscopy

XAS: X-ray absorption spectroscopy

XRD: X-ray diffraction

TEM: Transmission electron microscopy

General:

1D: one dimensional

2D: two dimensional

2DES: two dimensional electron system

AB: antibonding band

B: bonding band

CH: CuO chain band

BZ: Brillouin zone

DFT: density functional theory

FS: Fermi surface

HTS: high-temperature superconductor

PSI: Paul Scherrer Institute

SC: superconductor

SLS: Swiss Light Source

SX: soft-X-ray

T_c: critical temperature

u.c.: unit cell

UHV: ultra-high vacuum

Contents

Abstract	i
Zusammenfassung	iii
List of Acronyms	vi
1 Introduction and Motivation	1
2 Growth of STO/YBCO/STO system	7
2.1 Film growth by pulsed laser deposition	7
2.1.1 PLD setup at Empa	9
2.2 PLD growth of YBCO/STO heterostructures	11
2.2.1 Substrate preparation	11
2.2.2 Deposition conditions	14
2.3 In-situ RHEED	16
3 Characterization of YBCO/STO heterostructures	18
3.1 Crystal structure of the YBCO films	18
3.2 Surface topography	24
3.3 Transport properties of the ultra-thin YBCO	26
3.4 TEM study of STO/YBCO/STO(substrate) heterostructure	29
3.5 ARPES for band structure analysis in solids	32
3.6 Synchrotron radiation for interface electronic structure investigation	36
4 Investigation of the STO/YBCO interface by synchrotron	

radiation	44
4.1 Fermi surface of the YBCO	44
4.1.1 Selection of STO/YBCO films for SX-ARPES experiments	46
4.2 ARPES on the bare YBCO film	49
4.3 ARPES on buried YBCO: STO/YBCO interface	52
4.4 DFT calculations of YBCO Fermi surface	55
4.5 ResPES and XAS across the Ti L _{2,3} absorption edge	59
4.6 2×1 reconstruction at STO/YBCO interface	67
5 Importance of controlling SrTiO₃ surface termination	68
5.1 Importance of surface termination	68
5.2 Deposition of SrO film	69
5.3 Structural properties of ultra-thin SrO	75
5.4 Summary	81
6 Conclusions and Outlook	83
Appendix I	85
Appendix II	87
Bibliography	89
Acknowledgements	102
CV	104

Introduction and Motivation

Each generation of the semiconductor transistor manufacturing process, also known as "technology node", is characterized by the minimum feature size of the electronic devices. The node is typically indicated by the gate length of the transistor, which nowadays has reached dimensions below 10 nm. It has been proposed that at this scale, transistors should experience problems of quantum tunnelling through their gate oxide layer¹⁻³. Indeed, the theoretical limit at the nanometre scale points to the fact that the major issue is not just the manufacturing process but all the interface phenomena that dominate the transport properties.

For about a half-century, the investigation of interfaces has had a huge impact on the science and application of semiconductor devices. While the trend in scaling down Si-based devices seems to approach its limit, on the contrary the multifunctional character of the transition metal oxides manifests unexpected properties related to the special interactions which take place in selected interfaces. Therefore, alternative to the scale down approach, today a new pathway in microelectronics is to study heterostructures of complex oxides and their functionalities for the next generation devices.

Perovskite transition metal (TM) oxides have attracted interest of the scientific community for several decades, because of the large variety of properties and applications, which extend over a broad range, such as solar cells, magnetic or ferroelectric memories, non-volatile resistive switching memory, energy storage devices, etc.⁴⁻⁶. These oxides are ternary compounds characterized by the chem-

ical formula ABO₃, where A and B are two cations and O is the oxygen anion (see fig. 1.1). Due to a common oxygen octahedron with a typical dimension of about 0.4 nm, some of these compounds with different cation compositions have a low lattice mismatch and can be stacked in epitaxial heterostructures. At the interfaces between these oxides, the polar discontinuity⁷⁻⁹ and the lattice strain¹⁰⁻¹⁴ can be used in order to produce self assembled nanostructures^{15,16}, selective growth¹²⁻¹⁴ or even to generate new electronic states absent in the parent compounds^{7,17,18}.

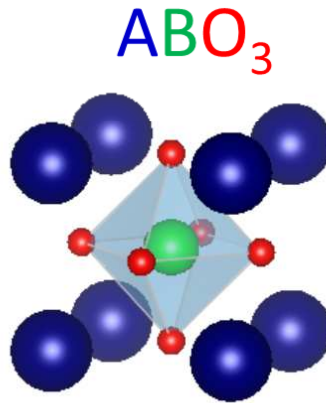


Figure 1.1: Crystal structure of ABO₃ perovskite. A and B (blue and green) are two cations, O (red) is oxygen.

For example, special interface phenomena have been observed in selected epitaxial heterostructures like LaAlO₃/SrTiO₃ (LAO/STO)⁷, GdTlO₃/SrTiO₃¹⁷, LaVO₃/SrTiO₃¹⁸ where unexpected conducting 2 dimensional electron systems (2DES) form at the interface of two insulators. The mechanism of this 2DES formation is still under debate: in contrast with the model involving the generation of the oxygen vacancy at the interface¹⁹⁻²³, it has been proposed that an intrinsic charge transfer mechanism builds up the 2DES as a consequence of an electrostatic potential at the interface due to a polar discontinuity²⁴⁻²⁶. In the case of LAO/STO interface one can observe also superconductivity (SC)²⁷ with a transition temperature T_c in the same range as in the bulk electron-doped STO^{28,29}.

Another interesting interface is the case of a superconducting FeSe monolayer grown on top of STO, which shows an enhancement of the critical temperature

of about 6 times compared to bulk T_c ^{30,31}. In this system, similarly to the LAO/STO case, it has been found that the charge carriers responsible for the superconducting phase are coupled to an optical phonon of the STO substrate^{32,33}. This result is quite intriguing in the case of FeSe where charge carriers are spatially separated from the optical phonon of the STO substrate. For this reason, some authors³⁴ refer to this long range Coulomb interaction as a mirage of STO into the FeSe. Even if Fe-based superconductors have different phase diagrams as compared to cuprate high-temperature superconductors (HTS), this result supports the idea proposed by Müller and Shenghelaya³⁵, that the interactions at the interfaces with a high-dielectric-constant insulator layer can be tailored to increase T_c ³⁵.

It is known that, in cuprate HTS, below some certain temperature, charges are self-organized into stripes or clusters³⁶. In particular, these clusters form as condensation of bipolarons³⁶⁻³⁸ which host the Cooper pairs. Upon cooling, the size of the clusters increase and due to tunnelling/percolating between them a macroscopic superconducting state is obtained^{36,39,40}. Müller and Shenghelaya have proposed³⁵ to exploit the dielectric confinement effect⁴¹ by sandwiching a superconducting cuprate film between high dielectric constant (ϵ) materials (as shown in fig. 1.2). In this nano architecture, dielectric screening could reduce the Coulomb repulsion between intrinsically present clusters/stripes of charges and eventually enhance the percolating regime, i.e. increase T_c . This effect is expected to take place in 1 or 2 layers close to the interface³⁵. Despite the simple idea behind this structure, there are several challenges for the films in the ultra-thin limit. Superconductivity at interface is sensible to many factors that can reduce T_c or even suppress the superconducting phase: ion interdiffusion, surface reconstruction caused by polar discontinuity, mobility of oxygen vacancies at the interface, structural defects, and space charge depletion.

In this thesis, we investigate interface phenomena, which take place between STO and HTS YBa₂Cu₃O_{7- δ} (YBCO). Transmission electron microscopy (TEM) analyses, performed in our investigations, show that in the case of YBCO grown onto (001)-oriented STO, c-axis mismatch between these two compounds produces anti-phase boundary defects. In the case of STO grown on top of YBCO

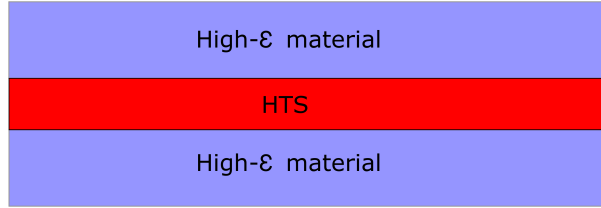


Figure 1.2: Schematic drawing of the proposed structure in which a copper-oxide high-temperature superconductor (HTS) is sandwiched between high-dielectric-constant insulator layers. (Adapted from ref. 35)

film, a better interface quality is obtained, which is then investigated spectroscopically (see chapter 4).

Soft X-ray angle resolved photo-emission spectroscopy (SX-ARPES) has been shown to be sensitive enough to investigate the band structure on the buried LAO/STO interface³³, where despite a few layers of LAO it was possible to study the 2DES which forms in STO. SX-ARPES was developed to overcome lower probing-depth (< 0.5 nm) of standard ARPES (with photon energy below 100 eV). Nowadays, many synchrotron facilities have reached a detector energy resolution of about 0.01% of the incoming photon energy. In these facilities, one can combine higher electron escaping depth with a spectrometer that can probe energy band dispersion near the Fermi level. In our investigation, we operate at the ADDRESS beam line of the Swiss Light Source (SLS) in an energy range $400 \text{ eV} < h\nu < 1000 \text{ eV}$ with a detection energy resolution of about 40 meV.

Films with 2, 4, and 10 STO layers on top of YBCO were prepared in order to be capable to detect photo-electrons emitted from the buried interface. As a first approach, we measured an uncoated film. We demonstrated that SX-ARPES can be successfully used to measure the Fermi surface (FS) of an ex-situ prepared YBCO film. Compared to low energy ARPES experiments (below 100 eV) reported previously by Sassa et al.⁴², we have an improved the signal to noise ratio in the first Brillouin zone(BZ), which allowed more accurate comparison with theoretical calculations. Moreover, thanks to the high photon energy range, we could detect the complete FS in large k -space without performing the numerical reconstruction of the acquisition range.

In the second part of our spectroscopic investigation, we measure the FS of

buried YBCO, which shows a change of symmetry. The observed signal can be explained by a 2×1 reconstruction which takes place at this interface. X-ray absorption and resonant photoelectron spectroscopy (XAS and ResPES) across Ti L_{2,3} edge show a modification of the Ti electronic states at the interface which can be assigned as well to a 2×1 structural reconstruction. This has been observed also in STO grown on the polar surface of LAO⁴³. It could be a general property of high- ϵ STO grown on the charged surfaces, for which a distortion of the oxygen octahedron may compensate the polar mismatch. Our investigation opens a new pathway to study electronic band states of epitaxial interfaces.

Structure of the thesis

The aim of this investigation was to study how the YBCO band structure evolves upon deposition of STO on top. Thin films of YBCO with and without STO cap layers were prepared by pulsed laser deposition (PLD). The experimental techniques, the performed measurements and the obtained results are described and discussed in this thesis with the following structure:

In **chapter 2**, I will describe the film deposition method used in this thesis. The PLD working principle and the set-up used in this investigation are presented. Particular attention will be given to the criteria of substrate selection and their chemical termination that allows high quality epitaxial growth.

In **chapter 3**, I will review the main experimental techniques that I used to characterize the crystal quality of the films. XRD, AFM and resistivity measurements were the main techniques used to select an ensemble of films for soft-X-ray spectroscopy investigation at PSI, ADDRESS beamline.

In **chapter 4**, I will show the results of photoelectron spectroscopy performed at the synchrotron. Apart the experimental results, here I will discuss theoretical calculations of the YBCO and STO/YBCO electronic structures.

In **chapter 5**, I will discuss the importance of STO chemical termination for the various interface phenomena. In particular, I present the case of the SrO termination and the structural properties of ultrathin SrO film deposited on a SrTiO₃ substrate.

Finally, the conclusion of the full investigations is reported in **chapter 6**.

An **appendix I** with further ARPES experimental data (which are not discussed in chapter 4), and an **appendix II** with an AFM calibration are reported at the end of the thesis.

Growth of STO/YBCO/STO system

In this chapter, I will describe the working principle of pulsed laser deposition (PLD) and the setup used in this investigation. Particular attention will be given to the criteria of the substrate selection and their chemical termination in order to achieve high quality of epitaxial growth.

2.1 Film growth by pulsed laser deposition

Pulsed laser deposition is one of the most frequently used techniques for synthesizing complex oxide films and heterostructures. Film growth occurs in a deposition chamber where the substrate and the target of the material are placed face-to-face. During the deposition, a pulsed laser is focused onto the target and ablates small amounts of the material (see schematic view of PLD in fig. 2.1). As a result, a plasma plume is created, providing the material flux toward the substrate for film growth. Typical power density for a single laser pulse with an energy density of about 2 J/cm^2 and 20 ns duration is 10^8 W/cm^2 , which is high enough to ablate nearly all perovskite oxide materials⁴⁴. Because of this high energy of the laser pulse, in good approximation, all atoms are homogeneously ablated and the stoichiometry of the materials is transferred from target to substrate. This makes PLD a very powerful technique for the deposition of complex materials, such as SrTiO_3 and $\text{YBa}_2\text{Cu}_3\text{O}_{7-\delta}$.

In most of the cases, a background gas pressure is present during PLD growth. The effect of this pressure is to reduce the kinetic energy of the ablated ions by

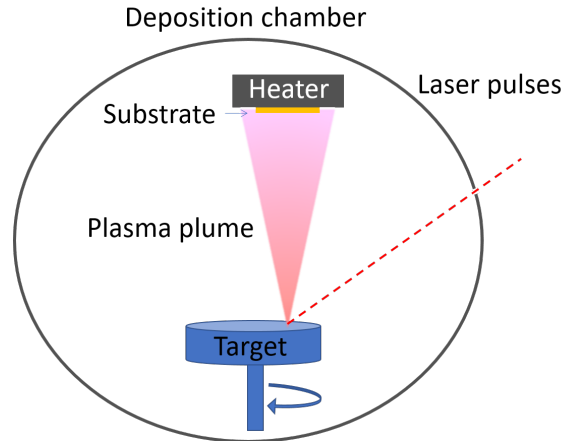


Figure 2.1: Schematic view of pulsed laser deposition. In the deposition chamber substrate and target are placed face-to-face. Laser pulses are focused onto the target and as a result a plasma plume is created, which provides the material flux toward the substrate for film growth.

scattering on gas molecules and acts as a stopping condition, which defines an optimal target to substrate distance. At pressures of about 100 mTorr of oxygen, this distance typically varies between 3-5 cm. In our experiments, the target-substrate distance was fixed at 4.5 cm for both YBCO and STO.

The film growth process can be described by the following steps: the arrival and adsorption of particles on the substrate ("ad-atom" formation), the diffusion of these ad-atoms on the surface, bonding to each other or to the substrate, then nucleation and micro-structure formation. The structure and morphology of the growing film depends on deposition parameters such as: substrate temperature, background gas pressure, target and substrate materials, laser pulse duration, power, and repetition rate, shape, and size of the focused laser irradiation spot. Basically, there are three film growth modes:

- **Frank–van der Merwe mode:** in this kind of thin film growth the ad-atoms are more attracted to the substrate than to each other and nucleation of the following layer starts only after termination of the previous one. This growth is also called layer- by-layer growth mode (fig. 2.2 (a)).
- **Volmer–Weber mode:** this growth occurs when the smallest stable clusters nucleate on the substrate and grow in three dimensions to form islands (fig. 2.2 (b)).

- **Stranski–Krastanov mode** (Figure 2.2 (c).): This mode is a combination of the two modes described above. During this mode, the film grows epitaxially on the substrate surface, as in the layer-by-layer mode, but above a critical layer thickness, it transforms to the Volmer–Weber regime.

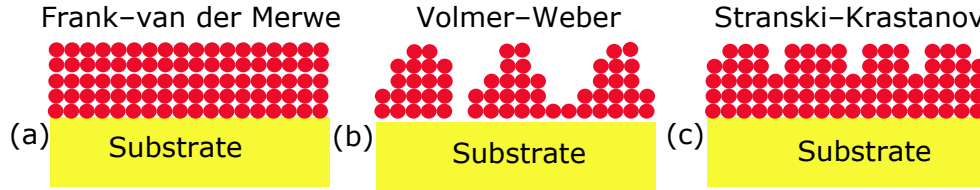


Figure 2.2: Schematic representation of three different growth modes. (a) layer by layer growth (Frank–van der Merwe mode), (b) island-like growth (Volmer–Weber mode) and (c) a combination of these two growth modes (Stranski–Krastanov).

In order to obtain high quality films with a smooth surface, a layer-by-layer growth mode should be achieved. This mode requires high surface mobility, which typically is achieved by heating the substrate up to high temperature and controlling good lattice match between the seed crystal and the growing material. In case of YBCO and STO, the lattice mismatch is 0.6% along the **a** axis and 2.2% along the **b** axis. This allows the growth of heterostructures with a coherent interface⁴⁵. Crystallographic characterizations of the YBCO/STO structures are shown in chapter 3.

2.1.1 PLD setup at Empa

The films studied in this thesis are synthesized by the PLD setup located at Empa, Dübendorf (fig. 2.3(a)). This equipment includes a KrF ($\lambda=248$ nm) excimer laser (Lambda Physik LPX300), a deposition chamber, and a load-lock with pump systems. The setup is shown schematically in fig. 2.3(b).

The laser pulse frequency can be set as high as 50 Hz, however, in order to guarantee a high film quality, typically 1÷2 Hz is used. The power of each laser pulse is tuned to about 55 mW for 1 Hz. The laser spot focused on the target has an area of about 0.25 cm², consequently a fluence of ~ 2 J/cm² is achieved. The laser is focused onto the target which is placed in the deposition chamber. Apart from the target under the laser irradiation, there are three more spare

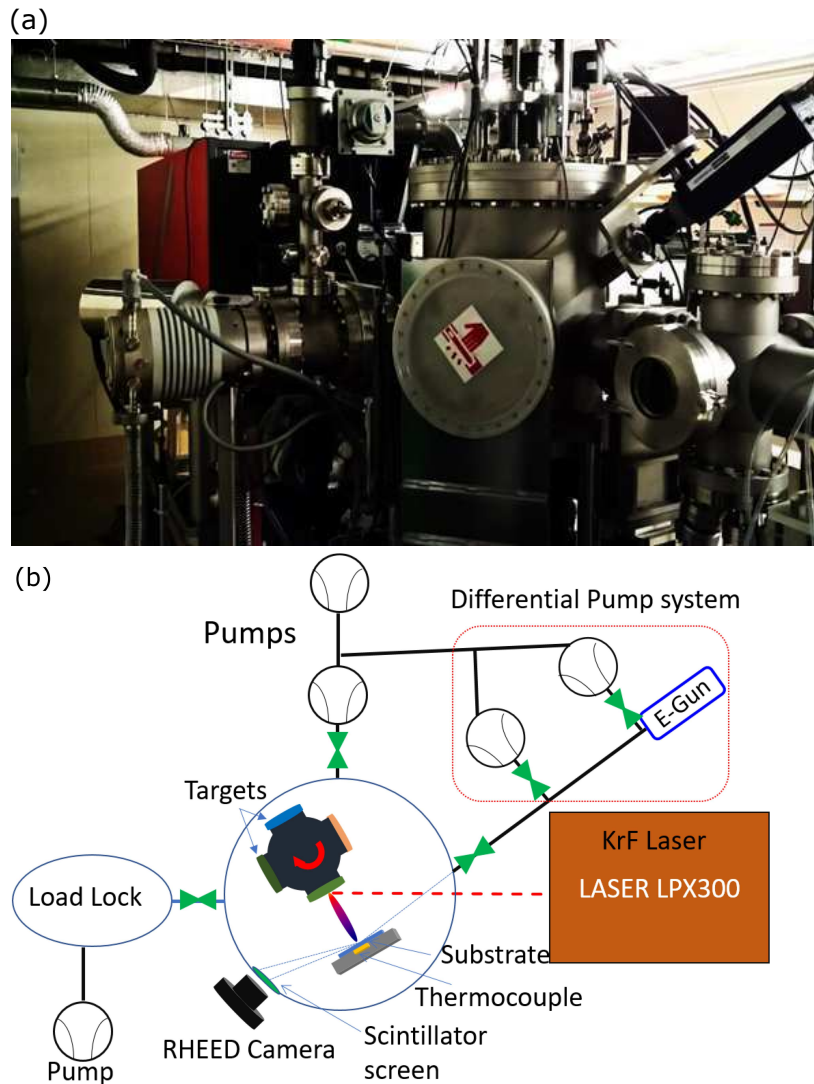


Figure 2.3: (a) PLD setup placed at Empa, Dübendorf and (b) its schematic representation. The excimer laser pulse hits the target at 45° angle. Low background pressure in the deposition chamber is achieved by the pumping system. The electron gun (E-gun) provides electron beam which hit the substrate with low angle ($< 5^\circ$) and produces a diffraction pattern on the scintillator screen. The differential pump system allows to keep the electron gun in high vacuum while the deposition pressure in the chamber is about 100 mTorr. Thanks to differential pumping, we can perform real-time monitoring of the growth condition by high-pressure RHEED.

targets mounted on the carousel which can be switched for deposition, without the need to vent the chamber. This allows the deposition of multilayers of different materials in-situ. The substrate is placed in front of the target of the depositing material and is glued to the heater by silver-paste. The temperature of the substrate is measured by a thermocouple inserted into the heater. In order to exclude errors due to poor thermal contact between thermocouple and substrate, the temperature is also measured by a pyrometer before and after deposition.

The deposition chamber is connected to two turbo pump channels: the main pump and the differential pump system for the reflection high-energy electron diffraction (RHEED). The main pump is used to create a high vacuum in the chamber. Here a mass flow controller is used for providing background gas pressure during deposition. Additionally, there is a differential pump system which allows us to keep the electron gun under high vacuum while connected to the chamber at about 100 mTorr pressure. Thanks to this differential pumping we can perform real-time monitoring of growth conditions by high-pressure RHEED⁴⁶. The RHEED system (Staib Instrumente GmbH) contains the following components: electron gun, photoluminescent detector screen, video camera for image processing, and Labview data acquisition software.

2.2 PLD growth of YBCO/STO heterostructures

2.2.1 Substrate preparation

In order to achieve a good quality interface for the deposited film, it is essential to have a clean and atomically flat substrate. One of the most frequently used substrates for epitaxial growth of complex oxide multilayers is SrTiO₃ (STO). Along its [001] direction STO is formed by stacking SrO and TiO₂ atomic planes and its top surface can be terminated by either TiO₂ or SrO. Polished STO(001) exhibits mixed termination, with a majority (~70 %-80 %) of TiO₂ (ref. 47) and therefore certain procedures are required to get a single chemical termination. In order to clean the surface of SrO and obtain TiO₂ terraces, buffered HF(NH₄F:HF) acidic etching can be used⁴⁷. Koster et al.⁴⁸ have developed a reproducible method of achieving single TiO₂ termination, using the following steps: 1) cleaning in ace-

tone (5 min), isopropanol (5 min) and deionized (DI) water (5 min), 2) etching by buffered HF(7:1, with pH = 4.5-5.5) for 20-30 sec and 3) annealing at 950°C in oxygen for 30 min. Procedures for the cleaning and etching to remove SrO and to achieve a flat surface are summarized in 4 steps in fig. 2.4

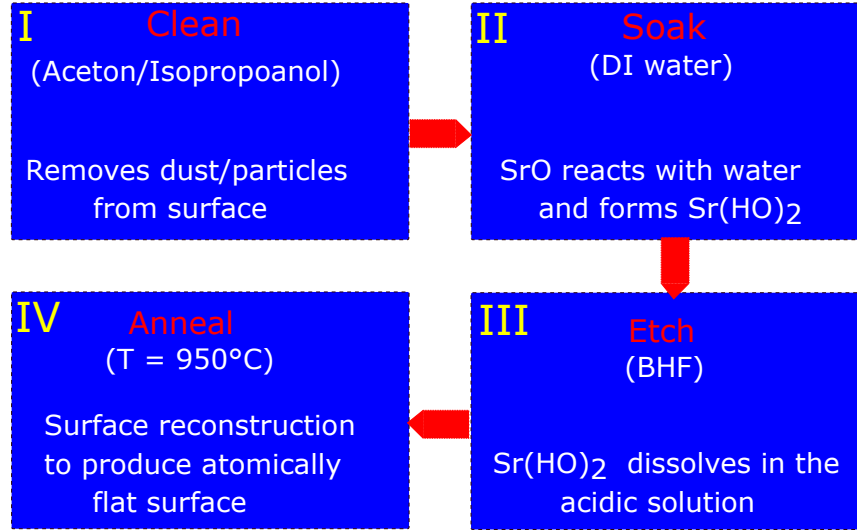


Figure 2.4: Schematic procedure of chemical etching and surface reconstruction for TiO₂ termination in STO: after cleaning in acetone, isopropanol and DI water the sample is etched by buffered HF for 25 sec, which removes Sr-hydroxide from the surface. The subsequent annealing at 950° C in oxygen for 30 min produces atomically flat and chemically uniform TiO₂ terminated terraces.

Thanks to this developed preparation recipe⁴⁸, TiO₂ terminated STO(001) substrates are commercially available. However apart from its high cost, a major issue is the ageing of the surface which degrades the quality of termination^{49,50}. Annealing of the aged substrate is not sufficient to restore a clean and flat surface, therefore the substrate should be prepared freshly before film deposition.

Figure 2.5 (a) shows AFM topographic images of a STO sample which was cleaned in acetone (5 min), isopropanol (5 min) and DI water (5 min). Substrate steps can be poorly seen compared to fig. 2.5 (b) where STO after 20 sec buffered HF (BHF) etching is shown. Here the acid dissolves strontium from the surface and produces a cleaner, step-like morphology. The final step is the annealing in oxygen, at 950°C for 30 min. At this temperature step-edges become less fragmented due to diffusion of surface atoms. The averaged root-mean-square (RMS) roughness of each terrace in the BHF etched substrate is 0.11(5) nm,

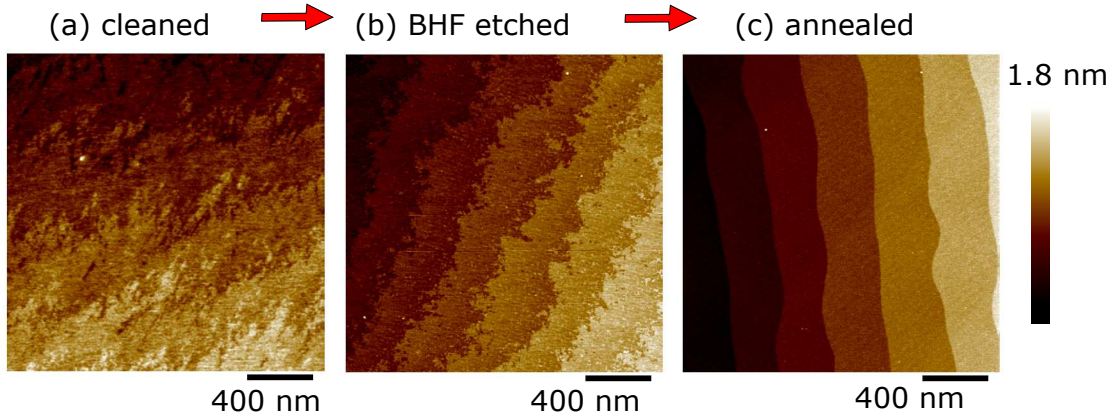


Figure 2.5: AFM topographic image of (a) cleaned (in acetone, isopropanol and DI water) STO(001) substrate, (b) after 25 sec BHF treatment and (c) after 30 min. annealing at 950° C in oxygen. The step-edge terraces clearly appear only after the last step.

while after annealing it reduces to 0.06(2) nm. The morphology of the achieved TiO₂ terminated substrate is shown in fig. 2.5 (c).

This procedure shows good reproducibility, however, the surface morphology can be strongly affected by many parameters such as the quality or concentration of BHF, crystal miscut angle, relative angle of cut, substrates principal axis directions etc. For example, some substrates have much wider steps, probably caused by a lower miscut angle. For such substrates annealing at 950°C, 30 min is not sufficient. During annealing, the step edges of the substrate change from rough to straight due to material diffusion on the surface, but when the terrace width is larger than the diffusion length, holes remain in the step-like structure (fig.2.6 (a)). In order to avoid this hole formation, we perform annealing at the same temperature for longer time. In fig. 2.6 (b) the substrate re-annealed for 10 h is shown. As a result, the number of holes are significantly reduced, and the step edges are also straighter. More drastic changes in the annealing procedures, such as 1200°C, 20 h, result in even fewer holes and straighter step-edges (fig. 2.6 (c)). However, higher temperature/longer time annealing can induce more defects⁵¹ which cannot be resolved by AFM. Additionally, for high temperature annealing, strontium segregation from bulk onto the surface is expected^{52,53}.

For our investigation, the surface topography of each substrate was systematically checked by AFM before each film deposition and only crystals with \sim

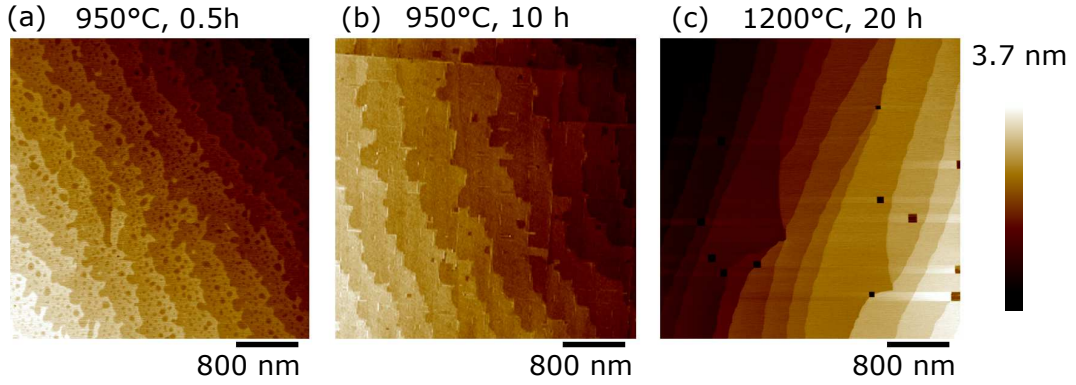


Figure 2.6: AFM topographic images of STO(001) substrate with miscut angle of about 0.05° after different annealing procedures: (a) substrate with typical thermal treatment (950°C , 0.5h), (b) re-annealed at 950°C , for 10h and (c) re-annealed at 1200°C , for 20h . After re-annealing the substrates have fewer holes and more straight step-edges.

200 nm steps were selected. An example of a typical substrate morphology is shown in fig. 2.5 (c)).

2.2.2 Deposition conditions

For film deposition we used a YBCO commercial target (HITEC-MATERIALS Dr.Ing Keschtka GmbH & Co.KG). The STO target was prepared by pressing SrTiO₃ powder (99.999% Sigma Aldrich) into $2\times 2\text{cm}^2$ pellet.

It is reported in the literature that the optimal deposition temperature for YBCO varies between 720°C , and 800°C ⁵⁴⁻⁵⁷. In general, higher deposition temperatures will increase the inter-diffusion of material at an interface and thus lower temperatures are preferred. We attempted YBCO deposition with different substrate temperatures: 700° , 750°C , 780°C and 800°C . Crystallographic and transport measurements revealed that 780°C and 800°C shows a better quality (see more details in chapter. 3). For this reason, our optimal deposition temperature was set to 780°C .

Deposition conditions for YBCO and STO films are shown schematically in fig. 2.7. Initially, the substrate is heated to 780°C . During deposition, 100 mTorr of oxygen pressure is used for both materials. The target-substrate distance is set to 45 mm and laser fluence is $\sim 2\text{J}/\text{cm}^2$. After deposition the films are cooled down to 600°C , about 400 Torr of oxygen is applied for 30 min, and then

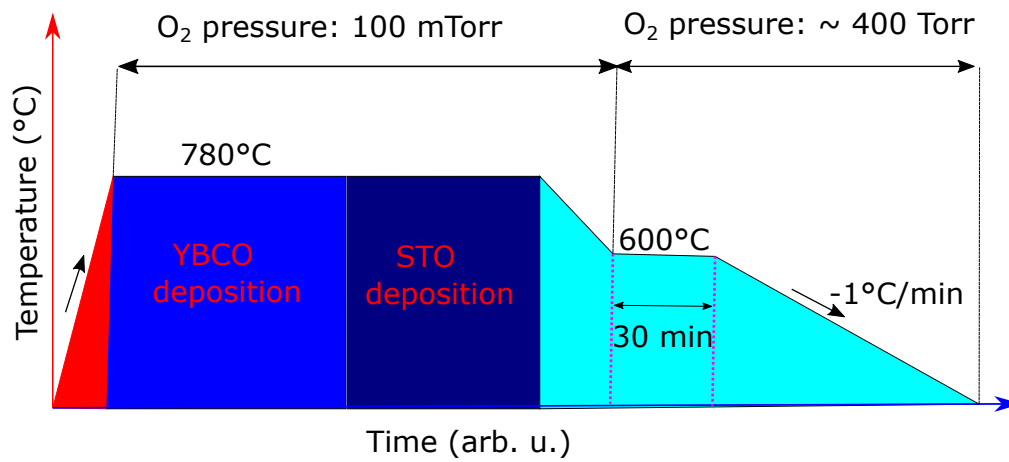


Figure 2.7: Schematic diagram of PLD grow and in-situ annealing conditions. After YBCO deposition, annealing at 600°C for 30 min in 400 Torr oxygen and slow cooling till room temperature provides optimally doped films.

extremely slowly cooled (1°C/min) in this oxygen atmosphere, in order to obtain optimal doping of YBCO⁵⁷. These growth conditions are also suitable for STO deposition^{55,58}.

2.3 In-situ RHEED

The film growth condition was monitored by in-situ reflection high-energy electron diffraction (RHEED). A typical diffraction pattern of the STO substrate before deposition is shown in fig. 2.8(a). After deposition of 10 layers of YBCO, the pattern (fig. 2.8(b)) shows multiple electron transmission spots, which is a typical sign of island-like growth⁵⁹.

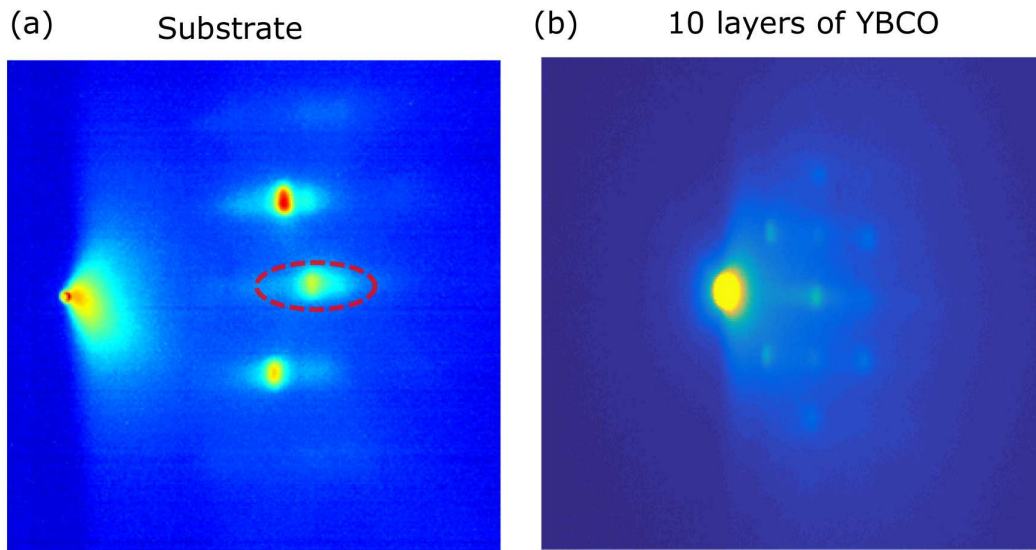


Figure 2.8: Representative examples of RHEED patterns of (a) STO substrate and (b) after deposition of 10 layers of YBCO. In order to follow the film growth dynamic the signal for a selected area indicated by the red dashed ellipsoid is integrated and monitored during the time of the growth (see fig. 2.9(a)).

An example of intensity oscillations of the specular spot of this pattern (which is indicated by the red dashed ellipsoid in fig. 2.8(a)) during the growth of 5 layers of YBCO, is shown on fig. 2.9 (a). These oscillations indicate a layer-by-layer growth mode. Damping of the oscillation amplitude can be explained by presence of 3D growth simultaneously with layer-by-layer mode^{59,60}. The oscillations can be fitted by a periodic sine function to quantify the growth rate, which typically varies between 52-55 laser pulses per layer. The number of deposited layers measured by RHEED was later confirmed by TEM for selected samples (see 3.4).

STO film deposition on YBCO also shows 2D growth. Representative RHEED intensity oscillations for 2 layers of STO deposition are reported in fig. 2.9 (b).

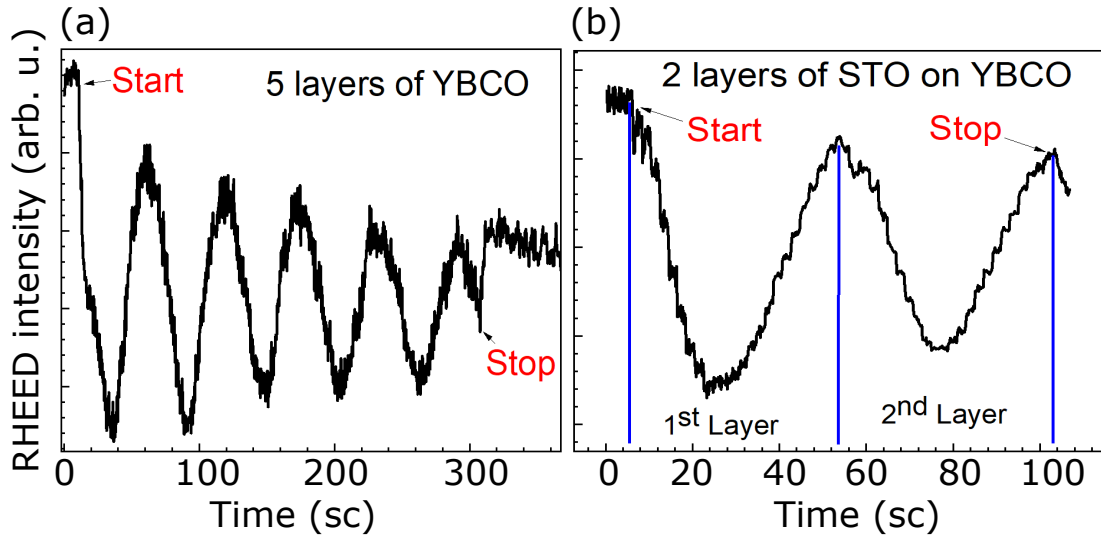


Figure 2.9: Examples of the RHEED intensity oscillations measured during the growth of (a) 5 layers of YBCO and (b) 2 layers of STO. These oscillations indicate a layer-by-layer growth mode for both materials. Each full period of the oscillations corresponds to the formation of a single atomic layer, thus precise thickness control is possible during the film deposition.

Here the laser pulse rate is 0.5 Hz, therefore the growth rate is ~ 25 pulses per layer. In order to obtain a fully completed layer at the end of the deposition, laser pulsing was stopped at the maximum of the oscillation intensity.

Characterization of YBCO/STO heterostructures

In this chapter, I will review the main experimental techniques that I used to characterize the crystal quality of the films. XRD, AFM and resistivity measurements were used to select an ensemble of samples for soft-X-ray spectroscopy investigation. At last, I will describe the ADDRESS beamline of SLS synchrotron.

3.1 Crystal structure of the YBCO films

The crystal structure of the YBCO films was studied by means of X-ray diffraction (XRD), using a Bruker D8 Discover diffractometer. The instrument is equipped with CuK_α radiation ($\lambda = 1.541 \text{ \AA}$), operating at 40 kV and 40 mA. We performed θ - 2θ scans in the Bragg-Brentano geometry to determine the crystal structure of the deposited YBCO films. In addition, texture measurements (i.e. pole figures) of YBCO {112} and STO {111} family of planes were acquired in point-focus geometry.

The typical Bragg-Brentano geometry is shown in fig. 3.1(a). Here, θ represents the incident angle of X-ray, \mathbf{Q} is the scattering vector, which has the direction along the bisection of the incoming and the scattered beam⁶¹, ψ is the tilt angle between the surface normal and \mathbf{Q} , φ is the azimuthal angle which defines in-plane rotation and ω is the angle of out-of-plane rotation.

We deposited films at different substrate temperatures (from 700° to 800°).

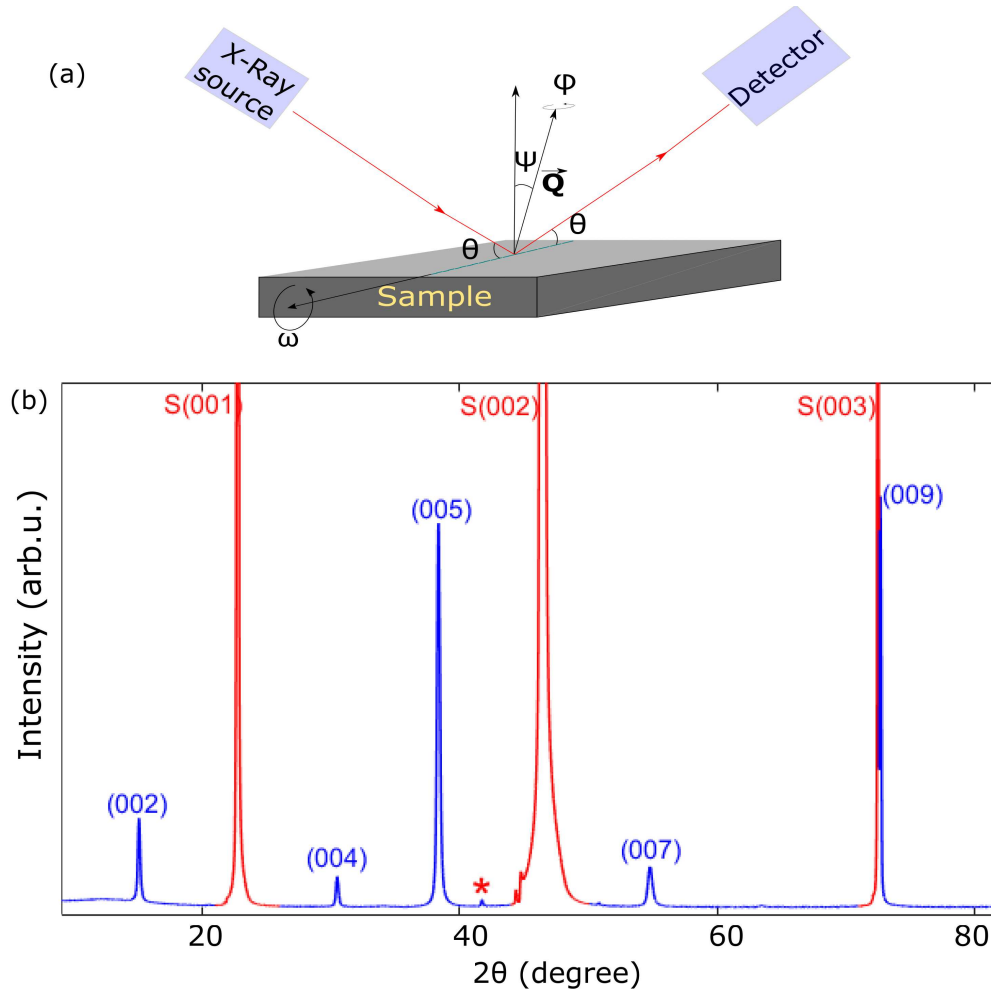


Figure 3.1: (a) Schematic of the Bragg-Brentano scattering condition (so called θ - 2θ scan). In this particular geometry the angle of the incident X-ray beam and the angle of the detected scattered beam are equal during the scan (this angle is indicated by θ). (b) XRD θ - 2θ scan of 21 u.c. of deposited YBCO. Since the film is (001) oriented with respect to the STO substrate, only (00 l) reflection peaks are visible. The additional peaks indicated by "S" belong to the substrate. The asterisk denotes reflection from the substrate due to presence of another wavelength ($k_{\beta} = 1.39225 \text{ \AA}$) in the X-ray source.

First, we measured films by the θ - 2θ scan method to study growth orientation and phase of the YBCO film. Figure 3.1(b) shows a representative XRD pattern where only YBCO (00 l) reflection lines are present, apart from substrate peaks (indicated in red and labelled with S). This indicates that the YBCO film grows along [001] direction (c-axis). The absence of other reflections in the entire diffractogram points out the existence of a single YBCO c-axis oriented phase. All films deposited in the temperature range from 700° to 800° show the same c-axis orientation.

The In-plane crystal coherence was measured by rocking curve (RC) experiments around the YBCO (005) reflection. In a rocking curve analysis, the detector is set at a specific Bragg angle (at YBCO(005) peak in our case) and the sample is tilted along ω . The RC resolves differences in the d-spacing and tilt of the crystallographic planes⁶¹. In a perfect crystal, where (00 l) planes are all parallel to the surface, RC should appear narrow with a full width at half maximum (FWHM) equal to the instrumental resolution. Deviation from perfect in-plane crystallinity makes the RC broader. Analysis of the RC for samples produced at different growth conditions represents thus a good screening experiment to select the highest quality samples with better crystallinity.

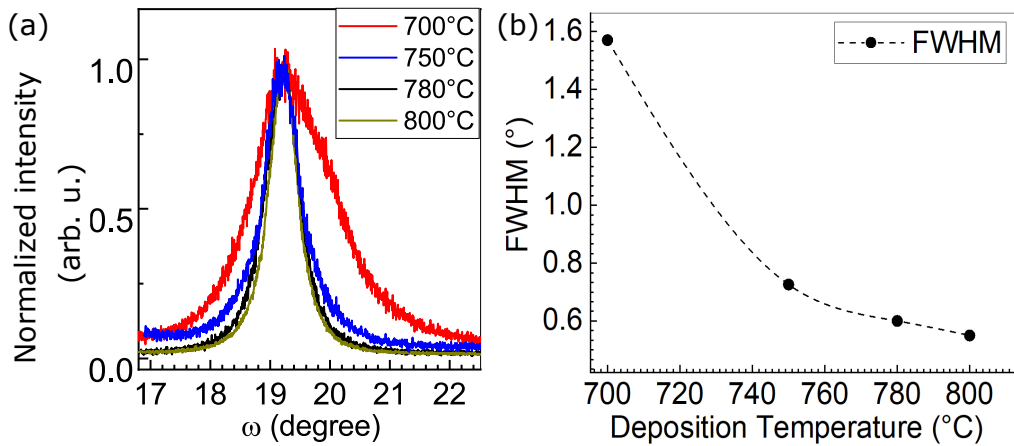


Figure 3.2: Rocking curves (RCs) of (005) reflection lines of YBCO films deposited at different temperatures. (b) Full width at half maximum (FWHM) extracted from the rocking curves as a function of deposition temperature. The film deposited at higher temperature has narrower RC denoting better in-plane crystal quality.

Figure 3.2 (a) shows RCs of YBCO(005) for samples grown at different depo-

sition temperatures. The broadest RC is found for the film deposited at 700°C, and with increasing temperature the RC broadening decreases. This tendency suggests that films deposited at higher temperature show better in-plane crystallinity with good parallelism of (00l) atomic planes. The RCs can be fitted by a Lorentzian function, with FWHM of the peak inversely proportional to the in-plane coherence length of the crystal domains⁶². Figure 3.2 (b) shows the FWHM of the RC as a function of deposition temperature. Films deposited at 780°C and 800°C evidence the best crystallinity with the narrowest RC with a FWHM of $< 0.5^\circ$. Based on this XRD characterization, all films further investigated in this thesis were deposited at higher temperature (780°C and 800°C).

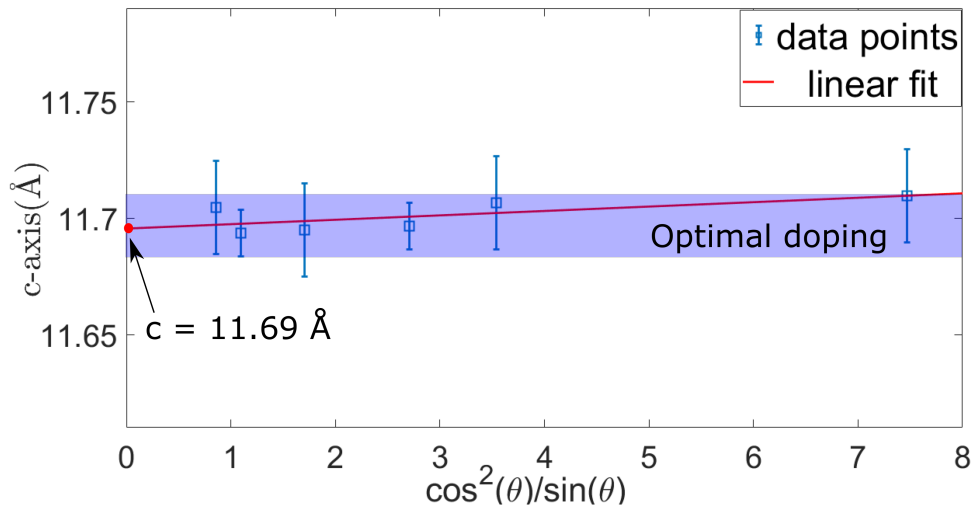


Figure 3.3: The c-axis values extracted from (00l) YBCO reflection lines (from $\theta/2\theta$ scan) plotted as a function of $\cos^2(\theta)/\sin(\theta)$. The best estimation of the c-axis value of the film can be obtained by extrapolating the intercept point with the ordinate, indicated by the arrow. The optimally doped YBCO has a c-axis in a range between 11.168Å to 11.172Å (ref. 63,64), marked by shadowed region.

XRD measurement also allowed us to estimate the doping level in YBCO films. In YBCO crystals and thin films, the value of the c-axis strongly depends on the doping, i.e. oxygen content^{63,64}. The c-axis value of the films can be calculated by the (00l) peak positions using Bragg's law. As shown in ref. 65, uncertainty in 2θ position, and therefore uncertainty in c-axis, is mainly related

to the error when mounting the sample (ΔR), and can be described by formula:

$$c = c_0 - c_0 \frac{\Delta R}{R} \left(\frac{\cos^2 \theta}{\sin \theta} \right) \quad (3.1)$$

Here c is the measured and c_0 is the actual c -axis of the film and R is X-ray source to sample distance. In order to minimize the errors caused by sample misalignment, we plot the calculated c -axis value for each peak as a function of $\cos^2(\theta)/\sin(\theta)$ (shown in fig. 3.3). The data points obtained are fitted by a linear function, where the actual c -axis value is the intercept point with the ordinate (11.69(2)Å in the figure). The range of c -axis values, where optimal doping is expected^{63,64} is highlighted in blue color in fig. 3.3. All YBCO films with post-annealing in oxygen have c -axis values of about 11.7 Å, in good agreement with that expected for optimally doped samples.

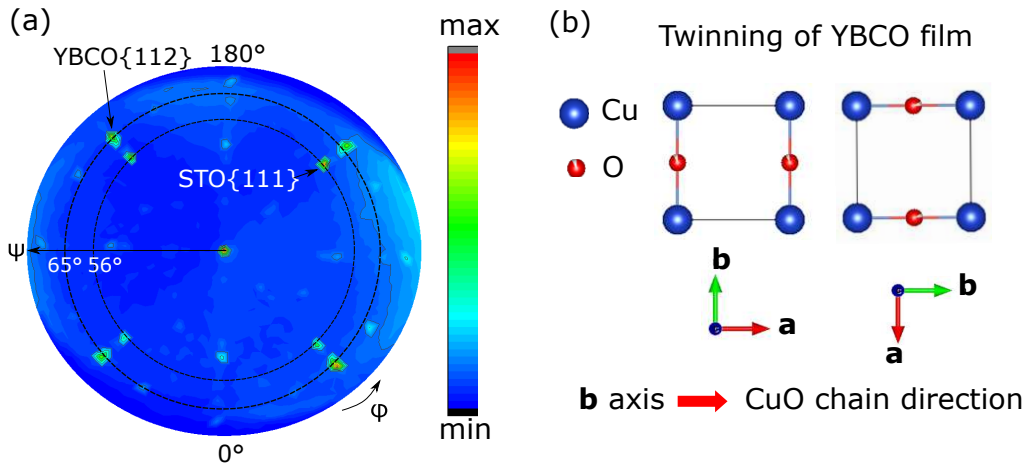


Figure 3.4: (a) Pole figure of YBCO {112}. The 4 peaks found for YBCO indicate twinning due to the cubic substrate. The fact that STO peaks are also visible is due to the close values of the 2θ of STO(111) reflection (39.96°). (b) Schematic CuO chains of two direction of 90° rotated domains.

The in-plane orientation of the YBCO films was investigated by XRD pole-figure measurement. During this measurement, the diffraction angle (2θ) is fixed at 36.33° (position of the YBCO(112)) and the diffracted intensity is collected by changing the tilt (ψ) and azimuthal (φ) angles. The measured diffracted intensity data is plotted as a function of ψ ($0^\circ \Rightarrow 90^\circ$) and φ ($0^\circ \Rightarrow 360^\circ$). Pole figure reported in fig. 3.4 (a) shows 4 peaks of YBCO(112) at $\psi=65^\circ$ and 4 peaks of STO(111) substrate at $\psi=56^\circ$. The fact that STO peaks are also visible is due

to the close values of the 2θ of STO(111) reflection (39.96°).

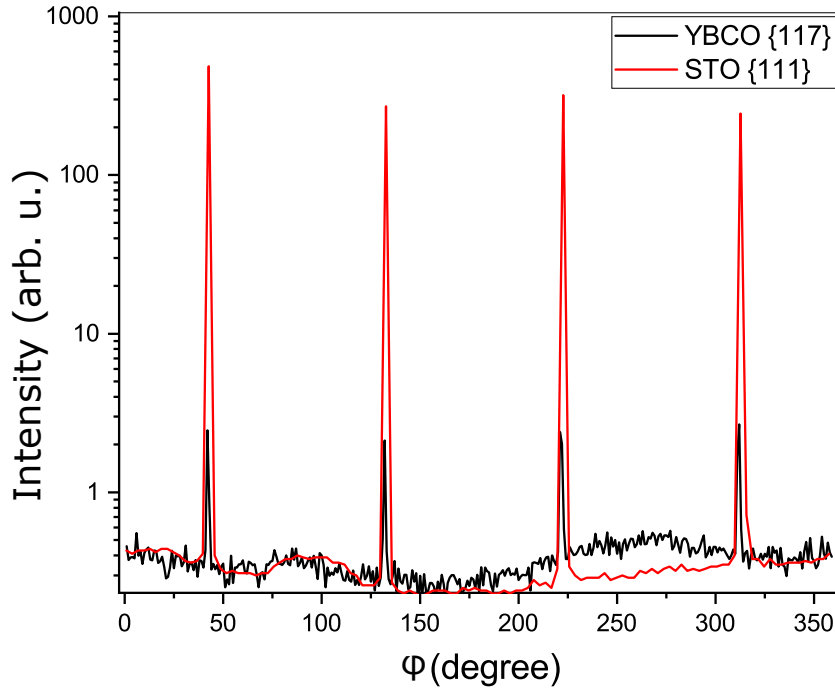


Figure 3.5: φ -scan of YBCO {117} and STO {111} reflection lines. Repetition of the lines over the 360 degree scan is connected to the crystal symmetry and textures of the film. In the case of the STO substrate, due to its cubic symmetry, the {111} reflection line repeats every 90 degree as shown in the plot. In the case of YBCO single crystal 2 peaks are expected due to its 2-fold symmetry, however 4 reflection lines are observed, which can be explained by 90 degree twinned domains in the film.

The angle where the YBCO signal is measured corresponds exactly to the angle formed between the plane (112) in the YBCO u.c. and the (001) plane. This confirms that the growth orientation of the YBCO film is along the [001] direction. Since the crystal structure of YBCO is orthorhombic ($a \neq b$), only 2 (112) poles are expected at $\psi = 65^\circ$. However, the observed 4 peaks located at 90° distance in the azimuthal plane, suggest that the YBCO film is twinned by 90° rotation of the two domains: $[100]_{YBCO} = [100]_{STO}$ and $[010]_{YBCO} = [100]_{STO}$ (see fig. 3.4 (b)). This is expected as the YBCO films are grown on a cubic substrate where lattice dimensions along **a** and **b** directions are equivalent. Moreover, we notice that the YBCO {112} planes have the same azimuthal position of the STO {111} planes indicating that the YBCO in-plane texture is inherited by the substrate underneath. This is further proven by φ -scan measurement reported in

fig. 3.5. The total preferred crystallographic orientation relationship between the substrate and the film can then be derived: STO{001} $\langle 110 \rangle$ // YBCO{001} $\langle 110 \rangle$.

3.2 Surface topography

The surface topography of the samples was characterized by means of atomic force microscopy (AFM) using a Bruker Icon3 instrument. Measured surface morphologies of YBCO films with different thicknesses are shown in fig. 3.6 (a-d). The surface is relatively flat in the case of 10 YBCO u.c., while in the case of thicker films, 3D islands start to form and increase the surface roughness. The surface morphology of 40 and 80 layers of YBCO show typical island-like growth. This kind of growth mode is typically observed for YBCO^{66,67}.

The root mean square (RMS) roughness dependence on the film thickness is shown in fig. 3.7. The roughness values were calculated for $2 \times 2 \mu\text{m}^2$ areas of different films. Averaged RMS roughness values show a monotonous increase with film thickness. The red dashed line in fig. 3.7 is drawn arbitrarily to guide the eye. In order to obtain a good quality interface in the STO/YBCO heterostructure high surface roughness should be avoided, therefore the YBCO film thickness should be as low as possible.

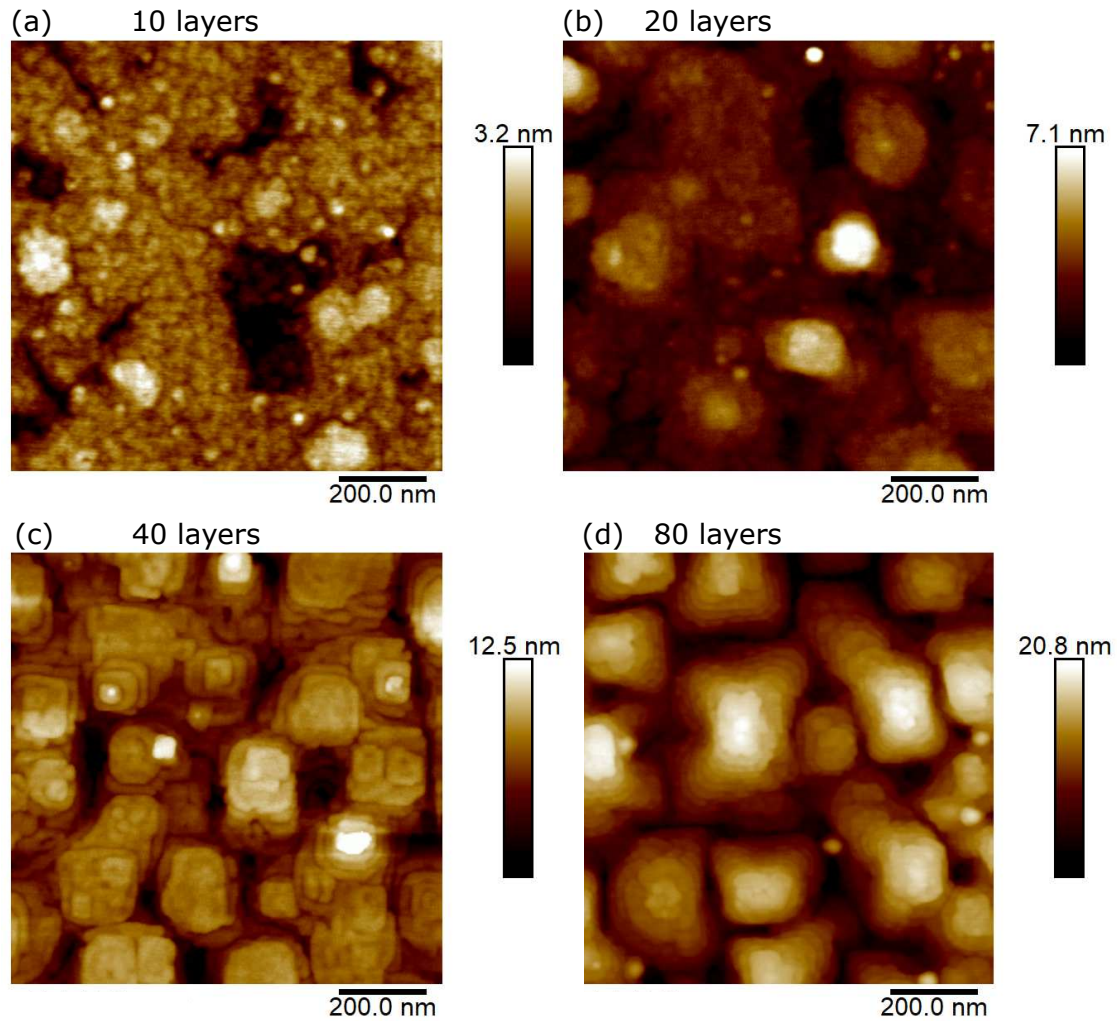


Figure 3.6: AFM surface morphology of the YBCO films with different thickness: (a) 10 u.c, (b) 20 u.c, (c) 40 u.c., and (d) 80 u.c. The surface is relatively flat in the case of the 10 u.c. YBCO, while in the case of thicker films, 3D islands start to form and increase the surface roughness. (Note the different intensity scale-bar)

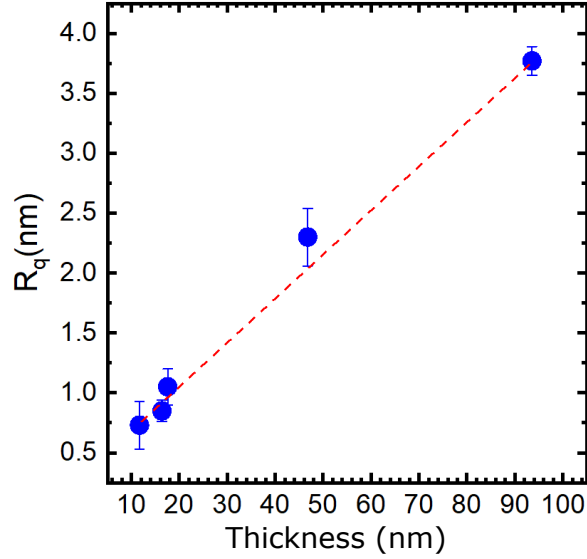


Figure 3.7: Averaged root mean square roughness (R_q) of YBCO surface calculated for $2 \times 2 \mu\text{m}^2$ areas of films with different thickness. The error bars represent standard deviation of R_q . The dashed red line in the figure is guide for the eye.

3.3 Transport properties of the ultra-thin YBCO

Transport properties of the YBCO films were investigated by a Physical Property Measurement System (PPMS) from Quantum Design. The sample holder (PPMS puck) with a mounted sample is shown in fig. 3.8 (a). A four-probe van der Pauw contact scheme was used for the resistivity measurement^{68,69}. The geometry of this contact scheme is shown in fig. 3.8 (b). Here, the applied current (I) flows between contact 2 and 1, and the voltage drop (V) is measured between contacts 3 and 4. In this scheme, resistivity (ρ) of the film with thickness t can be calculate by formula (ref. 69):

$$\rho = \frac{\pi t}{\ln 2} \left(\frac{V}{I} \right) \quad (3.2)$$

All the films of YBCO, reported in fig. 3.8 (c), having a thickness of 10 u.c., deposited at 780° or 800° show a superconducting transition temperature of ~ 86 K. It is known that achieving such a high T_c in the ultra-thin YBCO grown on STO is quite challenging and drastic suppression of the superconducting transition temperature below film thickness of 15 nm is observed^{57,70}. Only carefully

prepared substrates and precisely controlled growth conditions can avoid T_c depression in the ultra-thin YBCO films. Figure 3.9 shows T_c of YBCO film as a function of film thickness deposited on STO by different techniques: white circle - sputter deposition⁷⁰, and black circles - PLD⁵⁷. Blue squares and red circles represent films grown at Empa Dübendorf, with and without STO capping layers, respectively. Substrate preparation and film growth procedures optimized at Empa allowed us to obtain reproducible 10 u.c. YBCO films with T_c up to ~ 86 K.

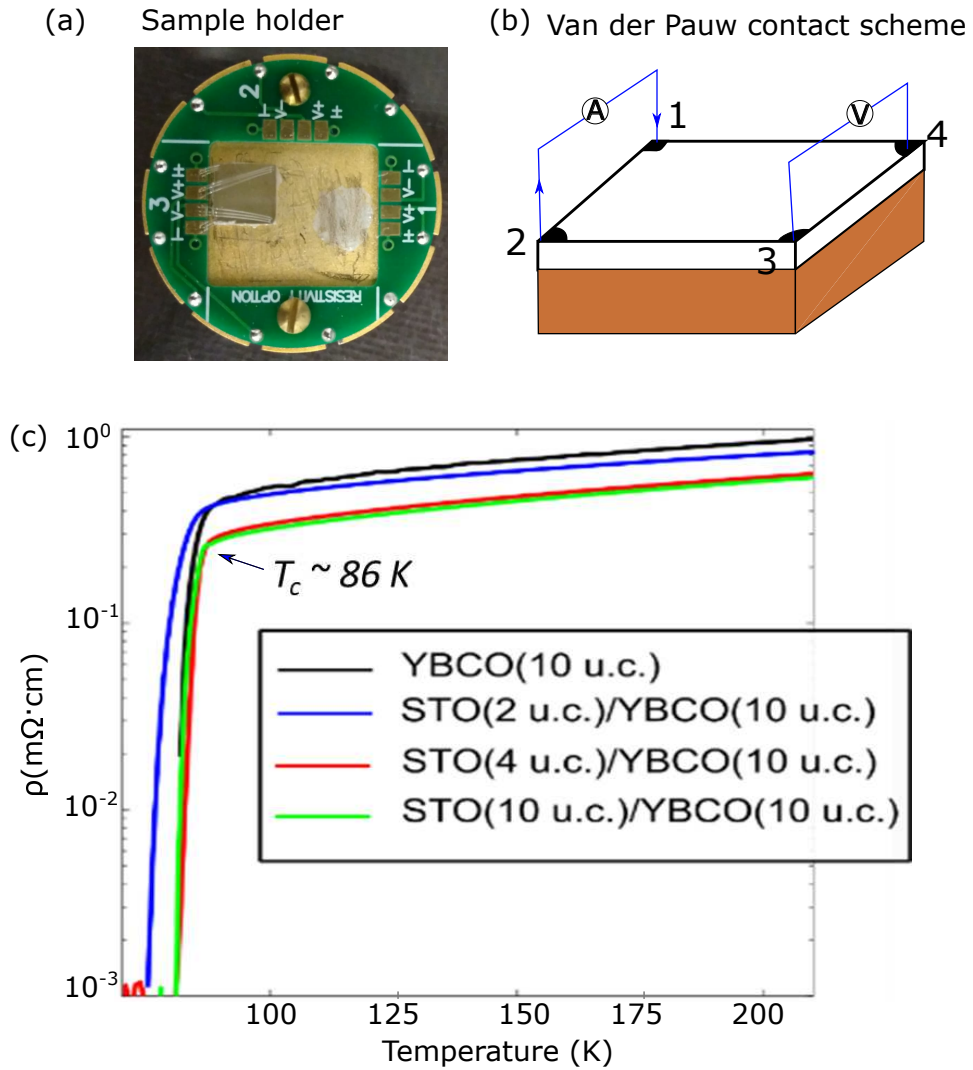


Figure 3.8: (a) PPMS sample holder and (b) van der Pauw contact scheme. Here, the applied current flows between contact 2 and 1, and the voltage drop is measured between contacts 3 and 4. (c) Resistivity of YBCO (10 u.c.) films with different thickness of STO capped layers. The superconducting transition temperature (T_c) was estimated as onset of the resistivity drop.

The origin of the T_c drop in ultra-thin YBCO films grown on STO was explained by the existence of interfacial defects induced by the out-of-plane lattice mismatch between YBCO and STO⁷⁰. The YBCO interface with substrate investigated by transmission electron microscopy (TEM) is discussed in next subsection.

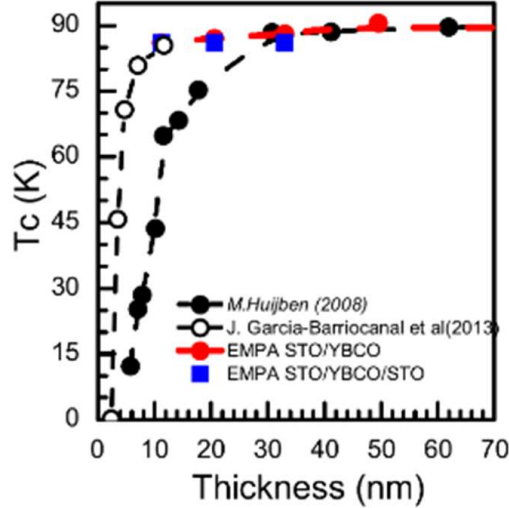


Figure 3.9: T_c of YBCO films of different thicknesses grown on STO by sputter deposition (white circle)⁷⁰, and PLD (black circles)⁵⁷. Blue squares and red circles represent films grown with our set-up. YBCO films show the same T_c with and without STO capping layers (blue and red, respectively).

3.4 TEM study of STO/YBCO/STO(substrate) heterostructure

A TEM image of our YBCO film and the STO substrate is shown in fig. 3.10(a). The TiO₂-terminated atomically flat STO presents step terraces, indicated by the red dashed line, with the height corresponding to the STO lattice parameter (3.905Å). This interface step is about 1/3 of the c-axis of YBCO and it generates anti-phase boundaries into the film. The TEM image shows these modified atomic layers in the YBCO close to the substrate. After 4 to 5 layers, the film shows relaxed continuous atomic planes indicating that the disorder at the substrate interface has healed during the YBCO growth. Schematic YBCO/substrate systems are shown in fig. 3.10(b). The green line represents the interface between the

first and second atomic layer of YBCO, where the anti-phase boundary generated due to the STO step is indicated.

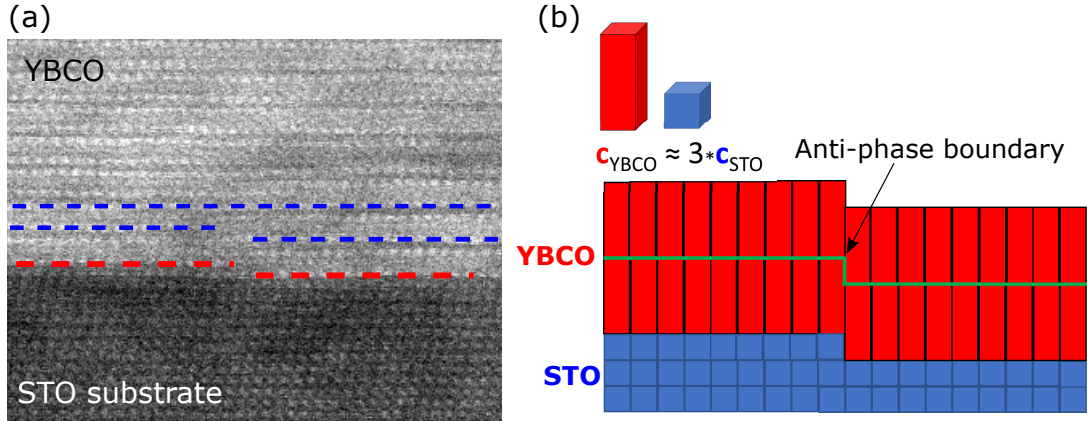


Figure 3.10: (a) TEM image of $\text{YBCO}/\text{STO}_{\text{substrate}}$ interface. (b) Schematic representation of $\text{YBCO}/\text{STO}_{\text{substrate}}$ interface: every STO surface step ($\sim 0.39 \text{ nm}$) generate defect into the next YBCO layer due to the fact that substrate step is about $1/3$ of the c -axis of the YBCO. The blue dashed lines show atomic planes of the YBCO film.

While the bottom interface ($\text{YBCO}/\text{STO}(\text{substrate})$) shows step-related defects, the top interface (STO/YBCO) exhibits good quality. In fig. 3.11 (a), a TEM image of this interface is shown which is schematically described in fig. 3.11 (b). Here, the YBCO film surface step height is equal to its c -axis value and 3 u.c. STO can adapt to each step without breaking the atomic sequence.

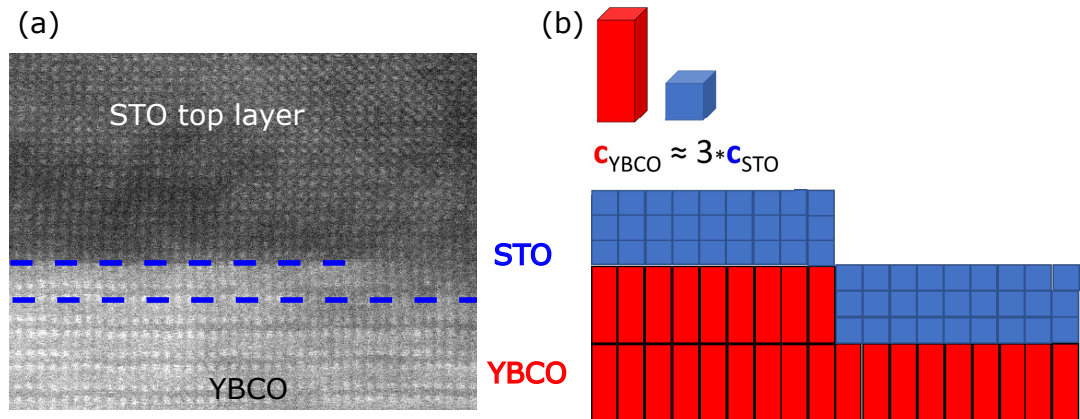


Figure 3.11: (a) TEM image of SrTiO_3 film grown on YBCO. (b) Schematic representation of $\text{STO}_{\text{TOP}}/\text{YBCO}$ interface: STO can adapt to YBCO step. The blue dashed lines show atomic planes of the YBCO film.

Further analysis of YBCO microstructure was performed by aberration corrected TEM at Electron Microscopy Center, Empa. The selected region of the

STO(4)/YBCO(10)/STO(sub.) sample is shown in fig. 3.12(a). The image shows that the first atomic layer formed during the YBCO growth is the BaO plane and then the following sequence of atomic planes will be: STO-TiO₂-[BaO - CuO₂-Y-CuO₂-BaO-CuO]. Schematic of the atomic plane sequence of YBCO is shown in fig. 3.12 (b). During PLD deposition, YBCO keeps this growth sequence and therefore, top termination of the film is always the CuO chain^{49,71}. However, in the case of the STO/YBCO heterostructure, upon deposition of STO on top, CuO chains are destroyed (due to segregation and desorption of Cu) and finally the interface lies between BaO and TiO₂ atomic planes (fig. 3.12 (c)).

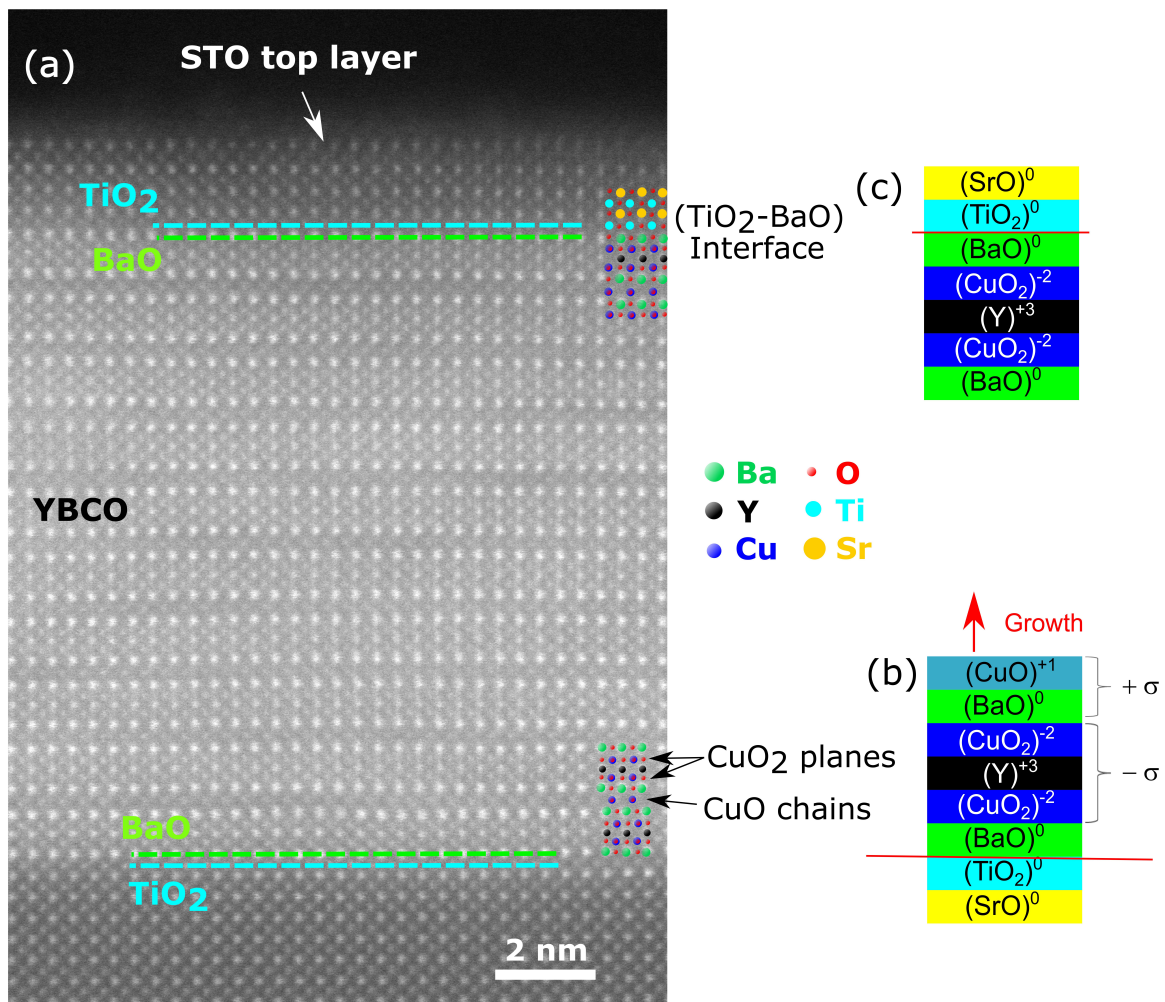


Figure 3.12: (a) Aberration corrected TEM image of STO/YBCO/STO(substrate). Top layer of *c*-axis oriented YBCO is BaO plane, on which STO is grown with TiO₂-SrO-TiO₂ sequence. (b) schematic atomic planes of YBCO(001) grown onto STO(001) substrate and (c) STO grown onto YBCO film.

Surface morphology and transport measurements show that ultra-thin YBCO (below 10 u.c.) evidences strongly depressed T_c , while thicker YBCO shows increased surface roughness, but with higher T_c . For this reason, we selected 10 u.c. YBCO films for our investigation, which show lower surface roughness and high transition temperature. The main experimental techniques used for STO/YBCO interface investigation are photo-electron spectroscopy (PES) and X-ray absorption spectroscopy (XAS), which have limited probing depth. Therefore the cap layer thickness had to be in the ultra-thin regime (1 to 4 nm). A detailed description of the sample selection can be found in **chapter 4**.

3.5 ARPES for band structure analysis in solids

Angle resolved photo-emission spectroscopy (ARPES) is a powerful technique to study the fundamental electronic structure parameters of crystalline solids^{72,73}. The Fermi surface (FS), band structure, and one-electron spectral function $A(\omega, \mathbf{k})$, all resolved in k -space, can be derived in an ARPES experiment. By the analysis of the ARPES intensity and momentum distribution, information on different electronic interactions (electron-electron, electron-phonon) can be assessed. Its working principle is based on the photo-electric effect: when the sample is irradiated by light, the photon energy is absorbed and electrons are ejected from the material with specific kinetic energy (E_k) and along specific directions in k -space. The relation between the measured E_k and the binding energy (E_b) of the electrons in the solid is given by the following formula:

$$E_k = h\nu - E_b - W \quad (3.3)$$

Where $h\nu$ is the incident photon energy and W is the work function of the material. It is then clear that if the impinging photon does not have enough energy, electrons cannot overcome the energy barrier and be emitted into the vacuum. In ARPES experiments, in addition to E_k , photo-emitted electron intensities for different emission angles are also measured. This means that in addition to the energy of photoelectrons, their momenta are also measured and mapped into band dispersion $E(k)$. In a typical ARPES set-up, photons are

produced by a monochromatic light source (gas discharge lamps, X-ray tubes or synchrotron radiation facilities). The electrons emitted due to the photoelectric effect, are then collected and analyzed with respect to their emission angle θ_e and their kinetic energy by an hemispherical electron analyzer (fig. 3.13 (a)). The analyzer is equipped with a 2D detector, where simultaneous multi-channel detection is possible. The E_k values of the emitted electrons are derived by applying a magnetic field which bend their trajectories as a result of the Lorentz force. The emission angles of the photoelectrons, directly after the emission from the solid, are projected in the entrance slit of the analyzer through electrostatic lenses. The combination of these two quantities, energy and angle, create a 2D image of photoelectron intensity as a function of E_k and θ_e in the focal plane of the hemispherical analyzer.

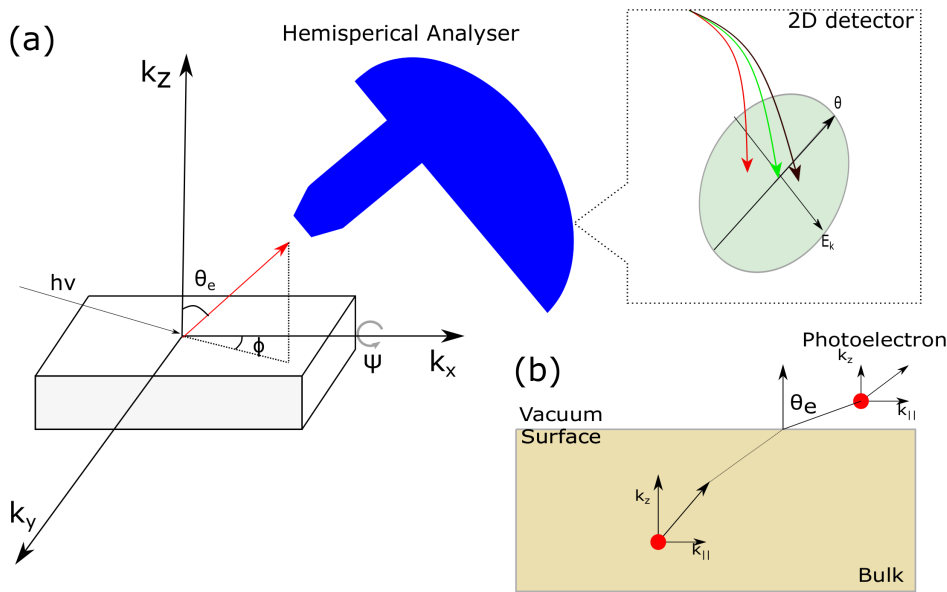


Figure 3.13: (a) Schematic diagram of the angle resolved photoemission spectroscopy experiment. When the sample is irradiated by light, photons are absorbed and electrons are ejected from the material with specific kinetic energy (E_k) along specific directions in k -space. The E_k of the emitted electrons is measured by the hemispherical analyzer. (b) Schematic representation of electron transfer from solid to vacuum: during the photoemission process, at the solid/vacuum interface the in-plane component of the electron momentum is conserved.

In the photoemission process, both energy and momentum of electrons in a solid are conserved. In particular, in crossing the solid-vacuum interface, the

photoexcited electron conserves the parallel component of the momentum (k_{\parallel}) that it has inside a solid. This is schematically represented in fig. 3.13 (b)). By measuring E_k and the emission angle, one can calculate the in-plane components of the emitted electrons' momentum with the following formulas:

$$k_x = \sqrt{\frac{m_e E_k}{\hbar^2}} \sin(\theta_e) \cos(\phi) \quad (3.4)$$

$$k_y = \sqrt{\frac{m_e E_k}{\hbar^2}} \sin(\theta_e) \sin(\phi) \quad (3.5)$$

Where k_x and k_y are the in-plane components of the vector \mathbf{k} , m_e is the electron mass, $\hbar = \frac{h}{2\pi}$, is the reduced Planck constant, and ϕ is the angle between the in-plane component of momentum and k_x . The perpendicular component of \mathbf{k} is not conserved as it is distorted by the crystal potential change at the surface. However, it can be recovered by assuming free-electron dispersion of the photoexcited electron states^{74,75}.

The intensity (I) of the collected photoelectrons as a function of E_k and \mathbf{k} can be expressed as follows⁷⁵:

$$I(\omega, \mathbf{k}) = |M_{f,i}|^2 F(\omega) A(\omega, \mathbf{k}) \quad (3.6)$$

Where $F(\omega)$ is the Fermi-Dirac electron distribution of the occupied states in the solid, $\hbar\omega$ is the electron energy with respect to the Fermi level and $M_{f,i}$ is the photoemission matrix element. This last one couples the final state with the initial electronic state and is defined as $M_{f,i} = \langle f | \mathbf{A} \cdot \mathbf{p} | i \rangle$. This component strongly modulates and affects the final measured photoemission intensity and results in some cases in non-symmetric signals in different Brillouin zones (BZ) or even in the same one. The experimental geometry, the photon energy, the polarization and the sample symmetry all influence the $M_{f,i}$ values. Tuning the light polarization and photon energy allows $\langle f |$ and its overlap with $|i\rangle$ to be modified, which results in either the suppressing or the boosting of the photoemission response of certain valence states.

In a typical ARPES experiment, 2D images of the ARPES intensity are collected at different values of θ_e and tilt angles Ψ (see Fig. 3.13(a)). Each image is a matrix of photoelectron intensity as a function of E_b and in-plane momentum.

The variation of the photoemission signal in this matrix gives the band dispersion and structure inside the solid. Mapping the photoemission intensity at the Fermi level E_F as a function of the 2 angles θ_e and Ψ will produce the 2 in-plane components of \mathbf{k} mapping the Fermi surface contour.

Soft X-ray ARPES

One big limitation of ARPES is represented by the low escape depth, or inelastic mean free path (IMFP) of photoelectrons. The standard laboratory source for the ARPES experiments is a Helium ultraviolet lamp which produces He I (21.2 eV) and He II (40.8 eV) photons. For these two energies, the IMFP value is below 1 nm (fig. 3.14 (a)), which indicates that the ARPES signal is limited only to the top most layer. For our investigation, where the aim is to study the STO/YBCO buried interfaces, this photon energy range is not appropriate. Moreover, lab-based ARPES facilities do not allow to tune photon energy and no photoemission signal optimization (for specific materials and elements) is possible. In order to increase the electron escape depth, we have to increase the photon energy towards the soft-X-ray (SX) range. This will result in a higher IMFP of photoelectrons, increased by a factor of two to five, compared to the conventional low photon energy ARPES (see universal curve, fig. 3.14 (a)). Using the SX range, therefore enables experimental studies of ex-situ prepared samples and even buried interfaces.

The major drawback of SX-ARPES is that the photoexcitation cross section Ω of the valence states reduces compared to that in the UV energy range, by several orders of magnitude. This is shown in fig. 3.14(b), where Ω is plotted as a function of $h\nu$ for the Cu 3d and O 2p states⁷⁷. Moreover, the SX-ARPES energy resolution is towards a few tens of meV, compared to UV photoemission of few meV. Such a drastic loss of photoelectrons signal has to be compensated by a high flux of incoming photons, to keep an appropriate signal intensity. In order to overcome all these problems, synchrotron radiation and facilities are needed.

For this purpose, during the PhD research, we wrote several proposals to have access to "ADvanced RESonant Spectroscopy" (ADDRESS) beamline at the Swiss Light Source (SLS), Paul Scherrer Institute (PSI) to perform our photoemission

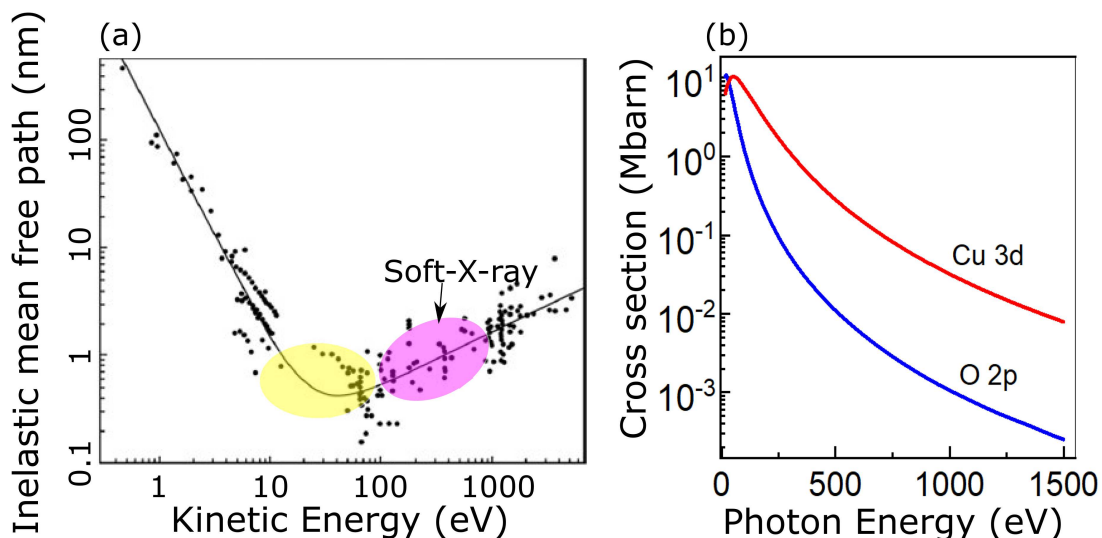


Figure 3.14: (a) Universal curve of photoemission with different energy ranges. Standard UV and soft X-ray energy ranges are marked by yellow and pink regions, respectively (adapted from ref. 76.) (b) Photoexcitation cross sections of the Cu 3d and O 2p states as a function of photon energy (from ref. 77).

experiments. This beamline delivers SX synchrotron radiation with one of the best energy resolution in the world (~ 0.05 eV in the soft X-ray regime). In the next section, we provide a brief description of the synchrotron radiation and the ADDRESS line.

3.6 Synchrotron radiation for interface electronic structure investigation

The principle of synchrotron radiation is based on the fact that the electrons accelerated radially close to the speed of light emit photons in the direction of their velocity (perpendicular to acceleration)⁷⁸. The synchrotron sources consist of:

- A source of electrons (electron gun).
- A linear accelerator to accelerate electrons.
- A booster ring where electrons are injected and further accelerated.

- The storage ring which contains and maintains the electrons on a closed circular path.
- Beamlines which run off tangentially to the storage ring.

A schematic planar view of the a synchrotron radiation source facility is shown in fig. 3.15. Electrons produced by the electron gun (E-gun) are accelerated in a linear accelerator (linac) up to MeV energy range and transferred to the Booster - the circular accelerator where they gain energy up to GeV range. (This values is 2.4 GeV for SLS, PSI). The electrons are transferred from the booster to the circular accelerator, called storage ring. The synchrotron ring is a structure containing bending magnets and straight sections used for insertion devices which generate intense synchrotron radiation. The magnets are used to deflect the electrons around the arced sections that connect the straight parts. The insertion devices consist of a series of magnets (wigglers or undulators) that turn the electron to the left and to the right resulting in emitting high intensity radiation.

The remarkable advantages of synchrotron radiation are high intensity and brightness of the beam, narrow angular collimation, and high stability. Moreover, it allows to tune the photon energy with precise steps. These key factors make synchrotron radiation a very powerful tool for ARPES experiments.

In our investigation, the aim was to probe the electronic states of YBCO below the STO cap layers, which can be realized by SX-ARPES. For this purpose, we selected the ADDRESS beamline at SLS (fig. 3.16). This line provides SX radiation with photon energies from 300 to 1600 eV. The important performance feature of this line is the high photon flux of up to 10^{13} photons s^{-1} (0.01% bandwidth)⁻¹ near 1 keV. As described in section 3.5, the high photon flux is essential in SX-ARPES because of the reduction of photoexcitation cross section with photon energy. A detailed description of the ARDESS beamline can be found in Strocov et al.⁷⁹

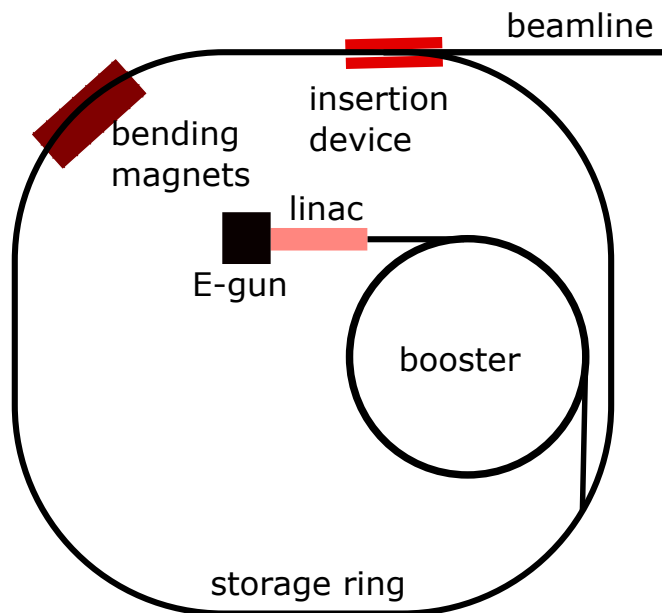


Figure 3.15: Schematic view of a synchrotron radiation source. Electrons produced by an electron gun (E-gun) are accelerated in a linear accelerator (linac) up to MeV energy. After, the electrons are transferred to the booster and they are further accelerated where they gain energy up to GeV. Finally, the electrons are transferred to circular accelerator, called storage ring. The beamline which runs tangentially of the ring, uses the radiation emitted from insertion device (wigglers or undulators) and from the bending magnets. For simplicity we show bending magnets and the insertion device only once.

ARPES end-station at ADDRESS line

The ARPES facility at the ADDRESS beamline is composed by four ultra-high-vacuum chambers: Load Lock (LL), transfer (TC), preparation (PC) and analysis (AC) chamber. (See fig. 3.17). The ARPES experiments are performed in the AC, which is directly connected to the beam and equipped with an electron energy analyzer. During the analysis, the sample is mounted on the manipulator where tilt and inclination angles can be changed. A cold finger cools the sample down to ~ 11 K (using liquid He). The endstation is equipped with the CARVING manipulator⁷⁹ providing three translational and three angular degrees of freedom (primary, tilt, and azimuthal rotations). The photoelectron analyzer is the PHOIBOS-150 from SPECS GmbH. Its angular resolution ($\delta\theta \sim 0.07^\circ$) is better than typical planarity errors of cleaved surfaces⁷⁹.

In order to investigate k -space of the sample and map the Fermi surface, we



Figure 3.16: ADDRESS line of the Swiss light source (SLS) at the Paul Scherrer Institute (PSI), Switzerland.

need to measure the photoelectron intensity for different emitted angles. The geometry of ARPES experiment is shown in fig. 3.13 (a). Here we indicated two important angles: the emission angle θ_e and the tilt angle (Ψ).

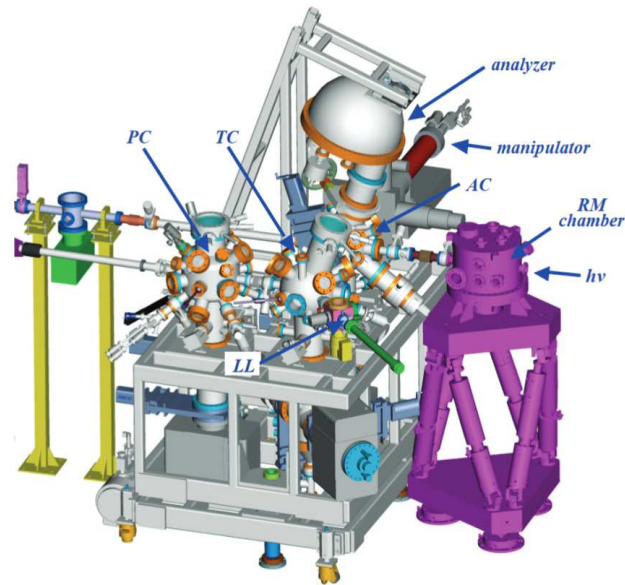


Figure 3.17: Schematic experimental layout of the ARPES set-up at ADDRESS beam line (extracted from ref. 80). The set-up is composed by four ultra-high-vacuum chambers: Load Lock (LL), transfer (TC), preparation (PC) and analysis (AC) chamber. The RM chamber contains the refocusing mirror which shapes the incoming photon beam.

The detector aperture angle (± 8 degrees) will provide at one time, information about the different k_x values of photoelectrons covering an entire range of the BZ in one measurement, while k_y is fixed. By changing the tilt angle, we could change the angle between the surface normal and the analyzer's optical

axis. Therefore, we can measure photoelectrons with different k_y values and map an entire BZ in the k_x - k_y plane. The measured angle (θ_e) and the tilt (Ψ) are related to k_x and k_y by equations 3.7 and 3.8.

$$k_x = \sqrt{\frac{2m_e}{\hbar^2}} * \sin(\theta_e * \frac{\pi}{180}) * \sqrt{h\nu - W}; \quad (3.7)$$

$$k_y = \sqrt{\frac{2m_e}{\hbar^2}} * \sin(\Psi * \frac{\pi}{180}) * \sqrt{h\nu - W}; \quad (3.8)$$

The work function (W) which is for our system 4.5 eV.

A correct sample alignment is an important step before the Fermi surface measurement. To achieve this, previous XRD characterization, which provides information about the samples crystal orientation, is crucial. It is also important to know the expected shape of the FS, which makes the alignment procedures easier. An example of the bare YBCO film alignment sequence is shown in fig. 3.18. Figure 3.18(a) shows a schematic FS of YBCO, adapted from ref. 81. The center of the first BZ, where these double lines cross each other is the Γ point. The edge of the first BZ, at ($k_x=1$, $k_y=0$), is indicated by X. (Further details of this FS will be discussed in section 4.1). Since we know that YBCO grows along the [001] axis on STO(001) (see chapter 3), we can assume that the samples edges (STO [100] and [010]) are parallel to the [100] and [010] directions of YBCO, and we can mount the sample to be nearly aligned with respect to the detector. After this we perform a rapid scan, which gives a first image of the FS with low signal-to-noise ratio. Figure 3.18 (b) shows the measured FS plotted along “Angle” and “Tilt”, which are proportional to k_x and k_y , respectively, for low angles. The x-axis represents the angular aperture of the analyzer and it is centered at the θ_e value. The y-axis is the Ψ tilt angle used to map the k_y direction. The measured FS shows horizontal and vertical lines, rotated 90° with respect to each other, which can be assigned to the expected CuO-chains. The most intense signal, where these lines cross each other is the Γ point. Our alignment, shown in fig. 3.18 (b) is performed by 840 eV photons. For this energy, $\sim 3.13^\circ$ corresponds to half u.c. of the BZ (Γ -X distance), and we can also estimate the location of the X-point on the FS. Different from the expected FS (3.18(a)), the CuO-chain related signal (highlighted by yellow dashed line) is not parallel to k_x

and k_y directions, which indicates misalignment of the sample with respect to the x-y plane of the detector.

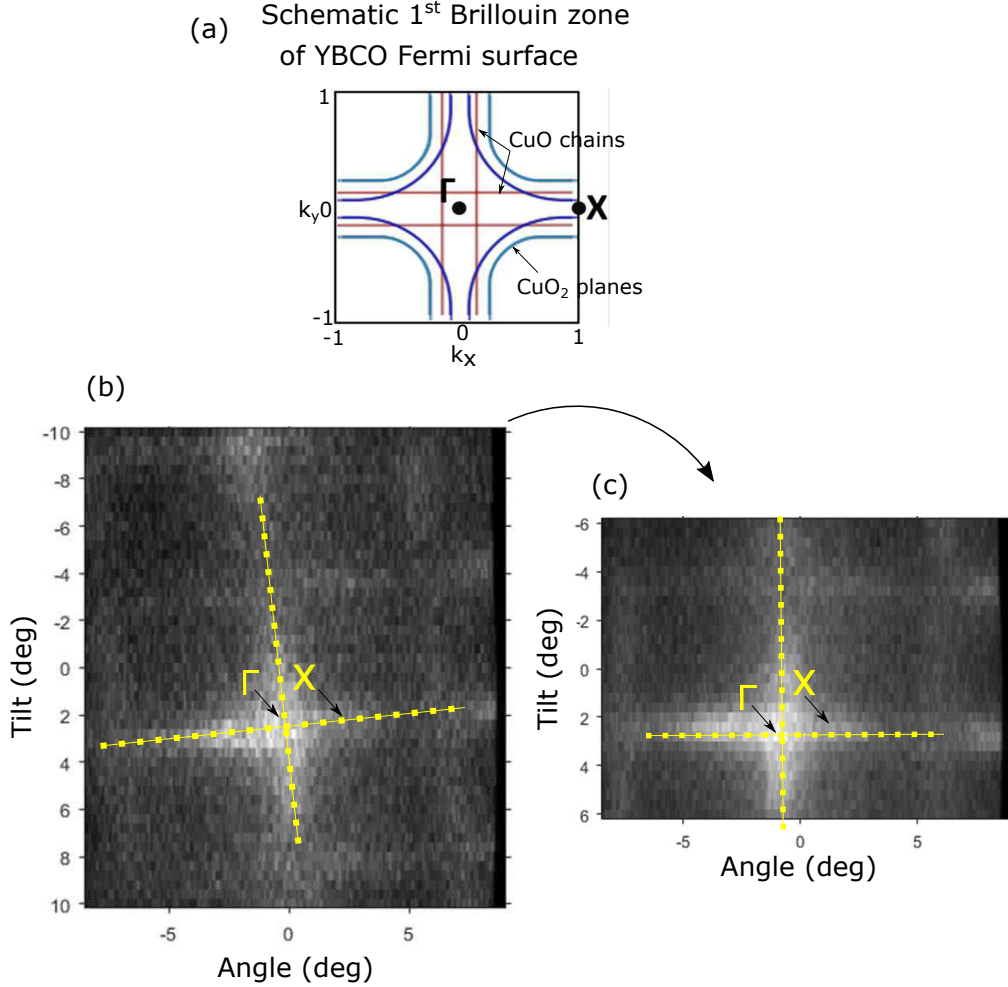


Figure 3.18: (a) Schematic of the YBCO FS from ref. 81 (b) Rapid FS scan with low data acquisition time for the sample alignment. CuO-chain related signal (marked by the yellow dashed line) is not parallel to the x and y axes which indicates misalignment of the sample with respect to the x-y plane of the detector. (c) Rapid FS scan after alignment procedures. In this case the 2 observed lines are parallel to x-y axes.

These alignment procedures continue by changing sample orientation and repeating rapid scan of the FS till the Γ -X direction became parallel to the k_x direction, as in fig. 3.18 (c).

The alignment was performed for all the YBCO and the STO/YBCO samples, measured at synchrotron radiation. The selection criteria of samples for synchrotron investigation and obtained results are discussed in chapter 4.

XAS and ResPES across Ti L_{2,3}

The ADDRESS beamline is equipped to perform X-ray absorption spectroscopy (XAS) by the total electron yield detection mode. In this way, we could also investigate the STO/YBCO interface by means of XAS across the Ti L_{2,3} absorption edge and compare the results with the corresponding resonant photoemission spectroscopy (ResPES) spectra. In the XAS experiments, photons excite core electrons to the unoccupied states of the solid. In the case of STO, the electronic structure of Ti is schematically shown in fig. 3.19. Here, photons with resonant energy (~ 450 eV) will induce photo absorption and electron transition from populated $2p$ level to unoccupied $3d$ levels. The $2p$ levels split into $p_{1/2}$ and $p_{3/2}$ levels by spin-orbit interaction, therefore, in Ti edge, two resonant transitions take place:

i) $2p_{3/2} \rightarrow 3d$

ii) $2p_{1/2} \rightarrow 3d$

The $3d$ band of Ti also splits into two levels (t_{2g} and e_g) because of the STO cubic crystal field. For that reason, each $2p \rightarrow 3d$ transitions have contributions from the t_{2g} (d_{xz} , d_{yz} , and d_{xy}) and e_g (d_{z^2} and $d_{x^2-y^2}$) levels and in total, four absorption signals are expected. This description is valid when the $3d$ levels are totally empty, as in the case of SrTiO₃ where Ti has the 4+ valence state. In presence of doping (e.g. oxygen vacancies) or of an electronic reconstruction, Ti changes its valence state to 3+, with the $3d$ levels now partially occupied. This will be then reflected in the XAS spectrum where, although still dominated by the Ti⁴⁺ ions in the STO bulk, a tiny admixture of the Ti³⁺ signal will appear between the Ti⁴⁺ peaks. The presence of other valence states in Ti and in particular, the presence of electronic states at the Fermi level, can be well evidenced by ResPES, which should be combined with the XAS experiment.

In the ResPES measurement, we collect photoelectrons emitted after resonant absorption, $2p_{3/2} \rightarrow 3d$, promoted by photons with exactly that energy. In ResPES we measure not only the photoelectron intensity, but also the binding energy of emitted electrons. This allowed us to obtain a 3D map (Incident photon energy vs Binding energy vs Emitted electrons intensity), where we can clearly visualize presence of electronic states at the Fermi level or in-gap states which

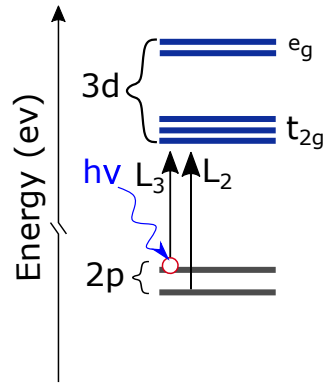


Figure 3.19: Schematic energy diagram of the Ti⁴⁺ ion.

can be caused by defects, oxygen vacancies in STO or some special interaction at the interface. This method was used to clearly demonstrate presence of an electronic state at Fermi level in the case of buried LAO/STO interface⁸².

Investigation of the STO/YBCO interface by synchrotron radiation

In this chapter, I report the synchrotron radiation investigation of the electronic structure of YBCO. The Fermi surfaces of bare YBCO and buried under few STO layers were measured by soft X-ray ARPES. We observed that the presence of an STO cap layer modifies the YBCO Fermi surface, which can be explained by a 2×1 reconstruction. The XAS and ResPES measurements at the Ti $L_{2,3}$ edge also evidences the presence of a 2×1 reconstruction in STO at the interface. DFT calculations are also presented and compared with the experimental results.

4.1 Fermi surface of the YBCO

The Fermi surface (FS) of YBCO was measured for the first time by Campuzano et al. using angle resolved photoemission spectroscopy (ARPES) in the twinned crystal using 50 eV photon energy⁸³. Later, more intensive investigations were performed on cleaved single crystal⁸⁴⁻⁹⁰. These studies show that the FS is composed of three components: (1) Bonding (B), (2) Antibonding (AB) bands in CuO_2 plane and (3) CuO chains (CH). A simplified Fermi surface of single crystal YBCO, extracted from ref. 81, is shown in fig. 4.1 (a). Here, B and AB states appear as arcs at the corner of the first Brillouin zone (BZ) and CuO chains as

2 parallel lines along Γ -X direction. In the case of twinned samples, the bands corresponding to CuO chains appear 90° rotated with respect to each other, as shown schematically in fig. 4.1 (b). Additionally, the top surface of YBCO always shows heavily over-doped features despite nominal doping^{81,86,90}, which represent the so-called "surface states". Moreover, cleavage in YBCO single crystals is possible, but the absence of a well-defined cleavage plane in YBCO always produces mixture of CuO chains and BaO planes termination^{91,92}.

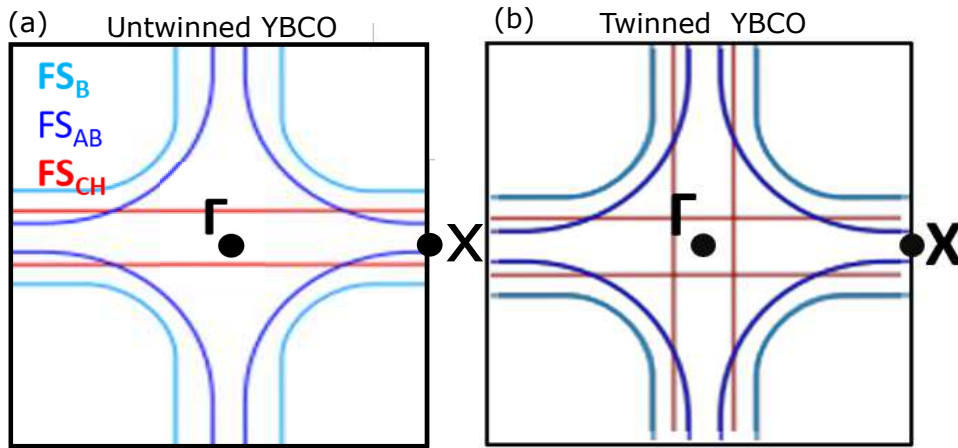


Figure 4.1: (a) Schematic Fermi surface of single crystal of YBCO, adapted from ref. 81. It is composed of three components: (1) Bonding (B), (2) Antibonding (AB) bands in CuO₂ plane, and (3) CuO chains (CH). (b) Schematic Fermi surface of the twinned YBCO film where chain bands are 90° rotated from each other.

In order to perform an ARPES experiment, clean surfaces are required and cleaved crystals are normally preferred compared to thin films. For this reason, many investigations of cleaved crystals are available in literature⁸⁴⁻⁹⁰, while in the case of thin films only one investigation is reported by Sassa et al.⁴² at $h\nu=70$ eV. They succeeded in measuring the FS of thin-film YBCO thanks to a special photoemission beamline coupled to a PLD setup^{42,93}. In their investigation, YBCO thin films were transferred in-situ to the ARPES chamber directly after growth, without breaking the vacuum thus preserving the clean surface from deposition. All the ARPES measurements reported so far for YBCO, single crystals or thin films, were performed using low energy photons, typical for a standard ARPES experiment. In this way better energy resolution is achieved. However, the probing depth is limited to the very last surface layer requiring extremely clean surfaces

or in-situ transfer.

Soft X-rays ($h\nu > 100\text{eV}$) have the advantage with respect to the standard ARPES energy range ($< 100\text{eV}$), of increasing the escape depth of photo-electrons. This allows the measurement of films produced ex-situ and even to probe photoemission in buried interfaces such as LAO/STO^{33,94}. Because of this unique capability, we applied soft X-ray radiation to measure the FS of the YBCO films and STO/YBCO buried interfaces

In the next section, a short description of the film selections for soft X-ray spectroscopic investigation will be reported.

4.1.1 Selection of STO/YBCO films for SX-ARPES experiments

In order to perform SX-ARPES experiments, thin films of YBCO with and without STO cap layers were prepared by PLD. As described in chapter 3, all these samples were characterized by AFM, XRD, and resistivity measurements. The thickness of all the YBCO films was fixed to $\sim 11\text{ nm}$ (10 u.c. YBCO) because for reduced thicknesses T_c is suppressed, and for increased thicknesses the surface roughness increases (see chapter 3).

In order to probe a buried YBCO layer by photoelectron spectroscopy, the thickness of the material above should be less than the escape depth of photo-electrons for a given photon beam energy. Therefore, the number of STO cap layers that we can place on the top of YBCO is limited. According to the Beer-Lambert law (equation 4.1), damping of the photo-electron intensity across a material can be characterized by the inelastic mean free path (IMFP), λ (ref. 95):

$$I = I_0 e^{-\lambda/d} \quad (4.1)$$

Where I is the final photo-electron intensity, d is the thickness of the solid crossed by the electrons and I_0 is initial intensity.

The IMFP parameter is defined as the traveling length of the electron beam across the material, after which its initial intensity decays to $1/e$ due to scattering

and interactions inside the solid. The value of λ for different materials can be calculated by TPP (Tanuma, Powell and Penn, ref. 96) equation:

$$\lambda = \frac{E}{E_p^2 [\beta \ln(\gamma E) - (C/E) + (D/E^2)]} \quad (4.2)$$

Where E is electron energy (in eV), $E_p = 28.8 (N_v \rho / M)^{1/2}$ is free electron plasmon energy (in eV), ρ is the bulk density (in g cm⁻³), N_v is the number of valence electrons per molecule, M is the atomic weight and β , γ , C and D are parameters reported in the literature for various chemical elements⁹⁶⁻¹⁰⁰.

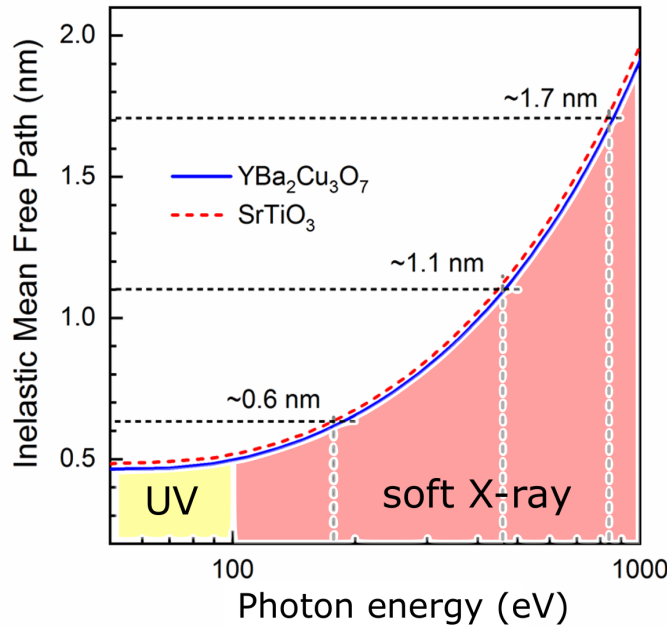


Figure 4.2: Calculated inelastic mean free path for different photon energies in STO and YBCO. Standard UV and soft X-ray energy ranges are marked by yellow and pink regions, respectively. High photon energy of the soft-X-ray increases the IMFP of photoelectrons upto more than 1 nm and allows to probe buried YBCO interface.

The IMFPs of STO and YBCO, calculated for different energies, are reported in fig. 4.2. According to these calculations, in the photon energy range between 800-900 eV, λ for both compounds should stay in the range between 1.5-1.7 nm, which corresponds to about 4 STO layers. Due to this limitation in probing depth, in our experiments we selected the following structures:

- YBCO(10)/STO(substrate)

- $\text{STO}(2)/\text{YBCO}(10)/\text{STO}(\text{substrate})$
- $\text{STO}(4)/\text{YBCO}(10)/\text{STO}(\text{substrate})$
- $\text{STO}(10)/\text{YBCO}(10)/\text{STO}(\text{substrate})$

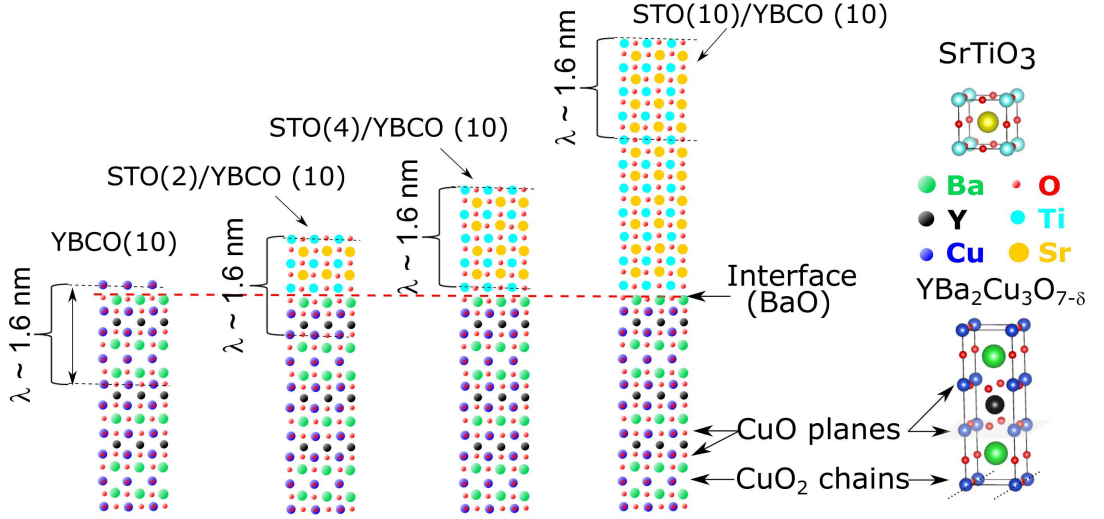


Figure 4.3: Schematic STO/YBCO heterostructures. The IMFP for 800 eV ($\lambda=1.6$ nm) is indicated. This photon energy allows to probe YBCO interface buried under 2 and 4 STO layers.

Schematics of the selected structures are shown in fig. 4.3. Due to the high photon energy range that we are using (800-900 eV), we expect to measure signals coming from about 2 to 3 layers of YBCO below the top surface. However, in the presence of cap layers, the screening effect of STO is expected to reduce the sensitivity to about one YBCO layer at the interface. In the extreme case of 10 u.c. STO cap layers, the screening effect should limit the signal entirely to STO.

We prepared 40 films for these experiments and after pre-characterization, we selected 9 of them which showed high crystallinity and low roughness, to be investigated at the ADDRESS beamline. All the selected samples were deposited less than about three months before beam time and stored in vacuum, in order to reduce surface contamination and ageing effects.

We measured similar samples multiple times to confirm the results. In table 4.1 we report a full list of the samples analyzed by synchrotron radiation. To avoid surface contamination, the T_c of the examined films was measured only

Sample	structure: YBCO(n)/STO(substrate)	SX-ARPES	XAS	ResPES
I	n = 10	✓	✗	✗
II	n = 10	✓	✗	✗
III	n = 21	✓	✗	✗
Sample	structure: STO(n)/YBCO(10)/STO(substrate)	SX-ARPES	XAS	ResPES
IV	n = 2	✓	✗	✓
V	n = 2	✓	✗	✓
VI	n = 2	✓	✓	✓
VII	n = 4	✓	✓	✓
VIII	n = 4	✓	✓	✓
IX	n = 10	✗	✓	✓

Table 4.1: List of selected samples for SX experiments.

after beamtime. The interface was further analyzed in selected samples by transmission electron microscopy.

4.2 ARPES on the bare YBCO film

The first part of our investigation is dedicated to studying YBCO films without STO cap layer by SX-ARPES. Untwinned cleaved YBCO single crystals measured by SX-ARPESS have been reported for the first time by Zabolotnyy et al.⁸⁷. They observe typical features (B and AB bands) of the YBCO FS at 176 eV photon energy, while by increasing the beam energy to a maximum of 920 eV they mainly observe features of CuO chain states. The momentum intensity distribution at the Fermi level measured by 870 eV photons, extracted from ref. 87 is reported in fig. 4.4(a). Here one can clearly identify features along the k_x direction indicated in the figure by the arrow. Compared to these states, bonding and anti-bonding band related arcs are less pronounced. We can assume that the photo-excitation cross-section for the chain states is enhanced at higher photon energy with respect to the photo-emission signal coming from CuO₂ planes⁸⁷. Cleaved YBCO single

crystals present a double surface termination with a mixture of charged (positive) CuO chains and neutral BaO planes. On one hand, the presence of CuO chains on the top surface of a cleaved crystal give rise to corresponding signals in the FS measurement. On the other hand, the coexistence of charged CuO chains and uncharged BaO terraces on the surface causes an electronic reconstruction and modifies the charge distribution on top of YBCO⁹⁰.

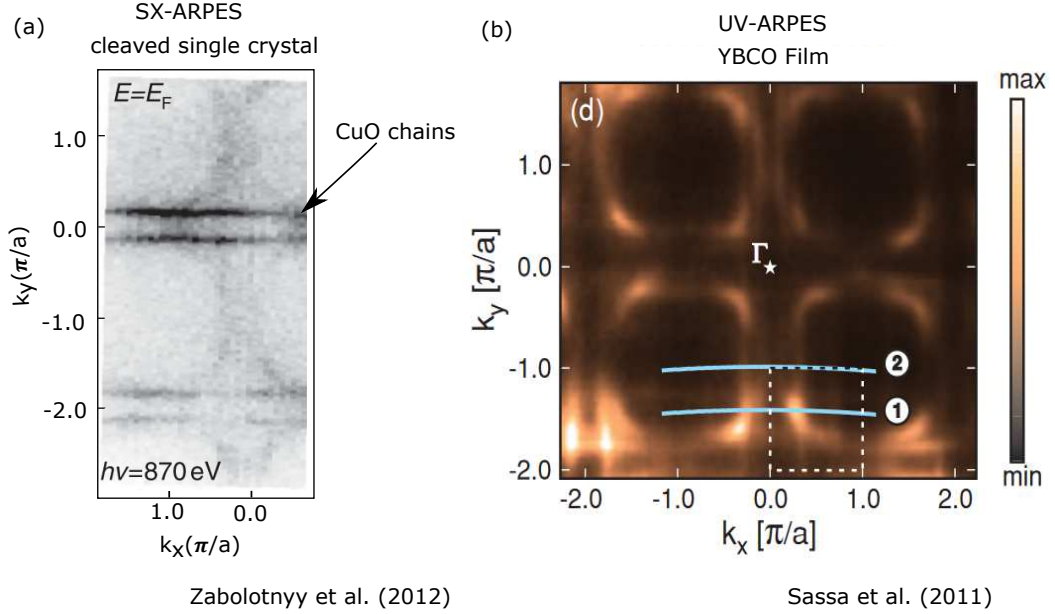


Figure 4.4: (a) Fermi surfaces of cleaved YBCO crystal measured by SX at 870 eV (extracted from ref. 87) and (b) YBCO film, measured by low energy photons at 70 eV (extracted from ref. 42). The two solid lines mark two specific cuts ① and ② in k -space, which are discussed in ref. 42

In contrast with cleaved crystals, YBCO films have a well-defined surface termination, which is a CuO chain in the case of epitaxial growth on TiO₂ terminated STO substrates. Therefore, the FS of a YBCO film should evidence a clear CuO chain band contribution.

As we mentioned in section 4.1, the only ARPES measurement in YBCO films is reported by Sassa et al.⁴². These measurements were performed at 70 eV photon energy, i.e. in the UV-range. This energy value was chosen from photon energy dependent measurements, to maximize the intensity contribution from the CuO₂ planes, while the CuO chains signal is suppressed at this energy⁴². The FS obtained is reported in fig.4.4 (b). Since the excitation energy was specially selected to favor CuO₂ plane contribution, the FS obtained mainly exhibits B

and AB arcs.

In case of SX-ARPES of YBCO film, greater contribution from CuO chain bands is expected, because of two factors. Firstly, as previously mentioned, the YBCO film is CuO chain terminated and therefore the main contribution to the total ARPES intensity is expected from the chains. Secondly, as reported by Zabolotnyy et al.⁸⁷, CuO chain states are more pronounced when using high photon energy (600÷900 eV).

In order to properly select the excitation energy which gives a higher SX-ARPES signal, we performed photon-energy dependent measurements (see appendix, fig. 6.1), which show the highest signal at $h\nu=840$ eV. The corresponding FS measured in our YBCO film is reported in fig. 4.5. The FS is composed of horizontal and vertical parallel lines, which represent CuO chains. These features are equivalent along the in-plane x and y directions, due to the twinning imposed by the cubic substrate. CuO₂ plane related arcs are not resolved (and not visible) by SX-ARPES. Notably, the ability to clearly observe CuO chain states in the FS indicates that SX-ARPES can successfully overcome the surface contamination problem on ex-situ prepared thin films, thanks to its increased λ .

We notice that the FS ARPES intensity signal in the reciprocal space is not homogeneous everywhere. This is a very common effect, widely observed in ARPES experiments: the photoemission intensity strongly depends on matrix elements (see 3.5).

In order to better visualize our FS, we performed a symmetrization of the ARPES signal in the FS in the first BZ . The raw data of the YBCO FS in the first BZ and the symmetrized FS are shown in fig. 4.6 (a) and (d) respectively.

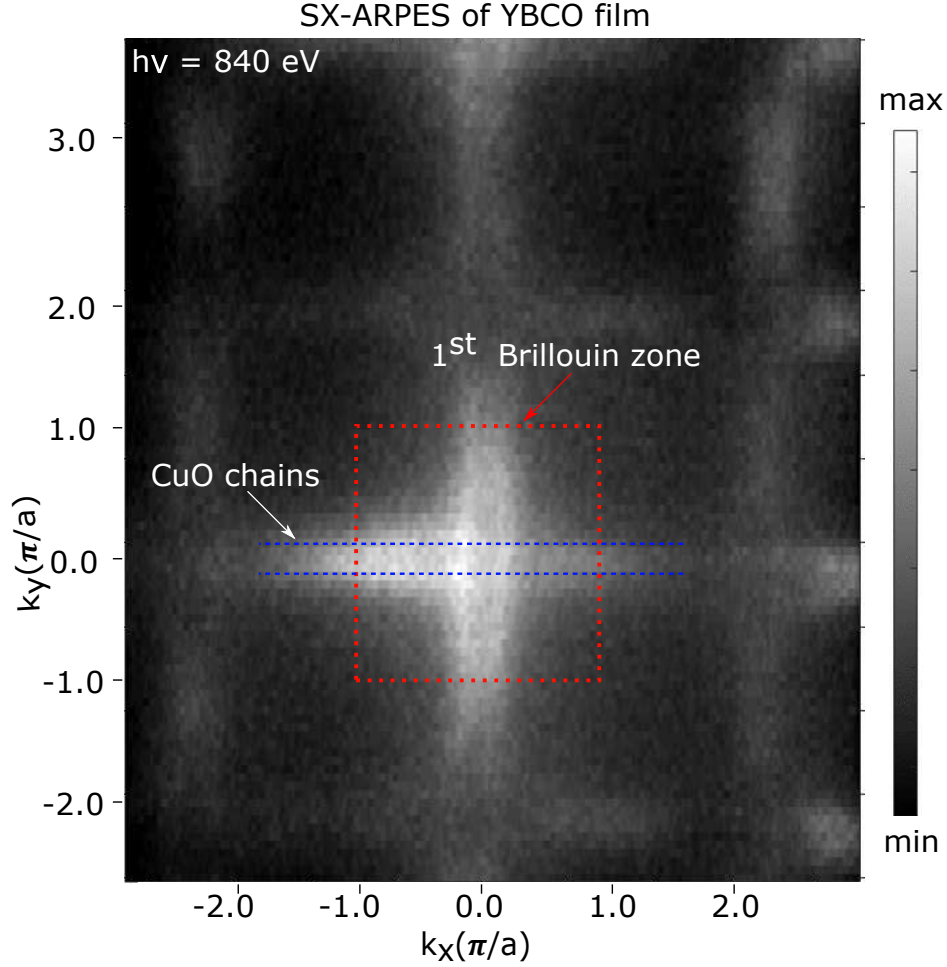


Figure 4.5: Fermi surface of our YBCO film, measured by soft X-ray at 840 eV photon energy. The 1st BZ is indicated by red dashed square. Horizontal CuO chain bands are marked by blue dashed lines. Because of the film twinning 90 degree rotated chain bands are also observed along the k_y direction.

4.3 ARPES on buried YBCO: STO/YBCO interface

The FS of the YBCO covered by 2 u.c. STO is reported in fig. 4.6 (b) (raw data) and fig. 4.6 (e) (symmetrized). The FS at the STO/YBCO interface appears considerably different to the FS of a bare YBCO film. In contrast with the FS of YBCO (fig. 4.6(a)), the ARPES signal associated with the CuO chains is no longer observed in the STO/YBCO interface. Instead the measured FS exhibits high intensity regions localized at the Γ point and at four other points on the edges of the BZ: (-1,0), (1,0) (0,1) (0,-1). Similar features although less

intense, are also visible in the STO(4)/YBCO(10) sample (fig. 4.6(c) and (f)). The reduced ARPES signal observed is due to the higher thickness of the STO cap layer which attenuates the photoemission signal. Further increasing the STO thickness to 10 u.c. completely damped the ARPES signal from YBCO. Indeed, it was not possible to collect any FS signal for the STO(10)/YBCO(10) sample. This result indicates that the STO cap layer is totally insulating and no ARPES intensity contribution is observed from STO. In order to validate this finding, we performed ResPES measurements at the Ti L_{2,3} absorption edge (see section 4.5). No signal was detected at the Fermi level at any photon energy ruling out any contribution of STO to the FS signal. Therefore, we can conclude that all the features observed fig. 4.6 are not related to STO and describe the real electronic modification of the YBCO film at the STO interface.

The four highest intensity regions observed on the four sides of the BZ are located at a distance of π/a with respect to the Γ point. This corresponds to half u.c. in the reciprocal space and two u.c. in real crystal structure. This affects the YBCO periodicity which is doubled and translates into a 2×1 reconstruction, indicating a different periodic atom rearrangement observed on the YBCO surface in contact with STO. Due to the twinning, a similar change of periodicity is observed along both k_x and k_y directions.

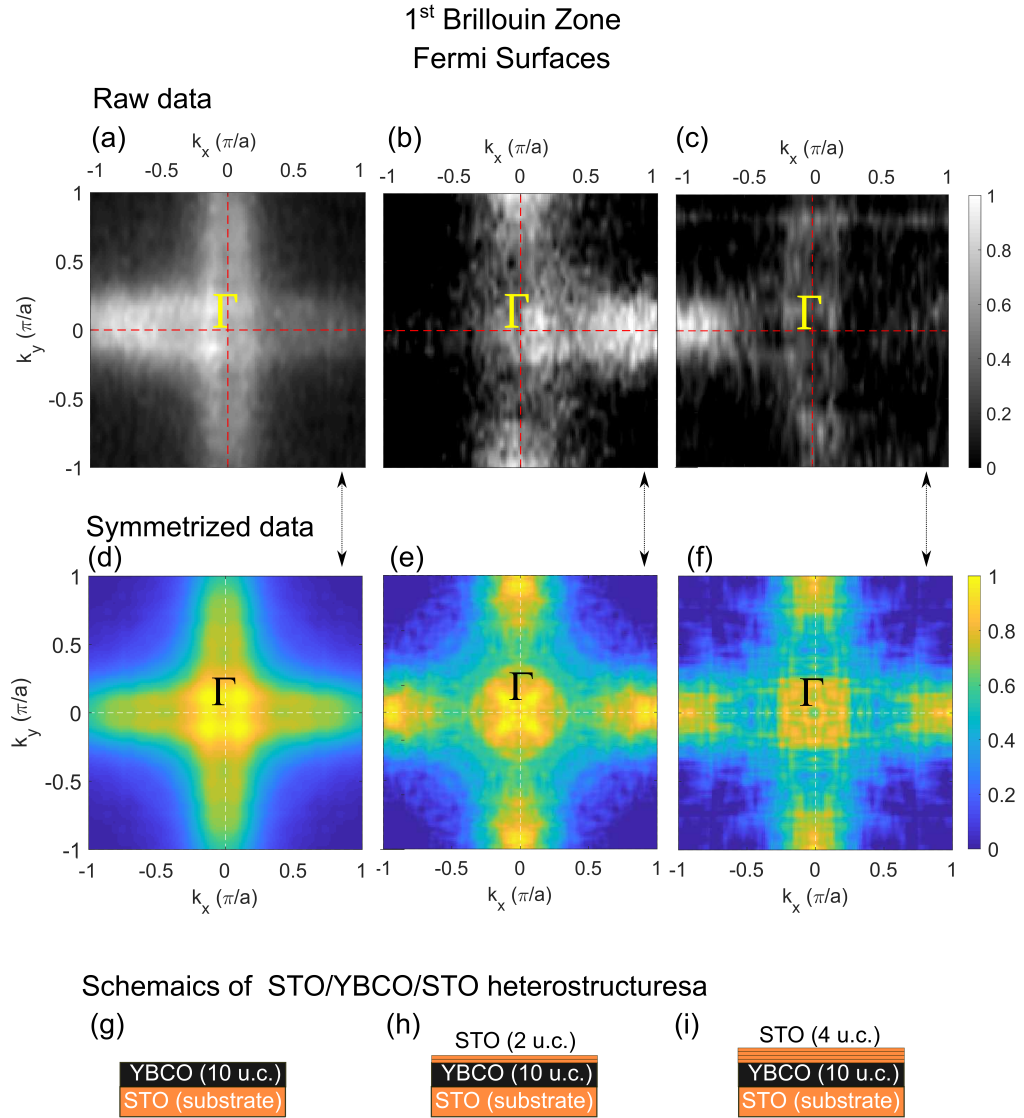


Figure 4.6: Experimental raw data of Fermi surfaces of (a) bare YBCO, (b) YBCO buried under 2 u.c. of STO, and (c) YBCO buried under 4 u.c. of STO. (d-f) These Fermi surfaces after numerical symmetrization and (g-i) schematic structures of these samples.

4.4 DFT calculations of YBCO Fermi surface

The Fermi surface of YBCO and STO/YBCO heterostructures were calculated by applying density functional theory (DFT) by the Atomistic Simulations Group (led by Dr. Daniele Passerone) of the nanotech surfaces laboratory at Empa, Dübendorf. The calculations were performed using the Quantum ESPRESSO code^{101,102}, and the projector augmented wave method (PAW)¹⁰³ was used for electron-ion interactions. The ex-change-correlation was approximated by the PBE functional¹⁰⁴.

Ideal YBCO should have an orthorhombic cell of $3.824 \times 3.888 \times 118.35 \text{ \AA}^3$. However, in order to include the strain induced by the substrate a distorted tetragonal cell with dimensions $3.905 \times 3.905 \times 118.35 \text{ \AA}^3$ was used which matches the STO cell in-plane parameters.

The numbers of layer used in all the DFT calculations reported here, have been chosen with a structure thick enough to ensure that it exhibits bulk-like behavior for the YBCO¹⁰⁵.

Two different structures were calculated:

- 1) YBCO with CuO-chain termination
- 2) YBCO with a cap layer of 3 u.c. of STO

The first structure in fig. 4.7 (a) corresponds to 3 layers of YBCO containing top and bottom vacuum interfaces with CuO- and BaO- terminations respectively. This particular structure follows the stacking sequence of epitaxial growth on TiO₂ terminated STO substrates (see 3.12) which guarantees charge neutrality of the full system.

The second structure shown in fig. 4.7 (b) was calculated in order to simulate the BaO-TiO₂ interface observed by TEM for STO/YBCO heterostructures.

CuO chain termination

A schematic of the reduced DFT cell used for calculation in the case of CuO chain termination is shown in fig. 4.8 (e). All the atomic planes which compose the YBCO layered structure are numbered from the bottom (number (nr.) 1,

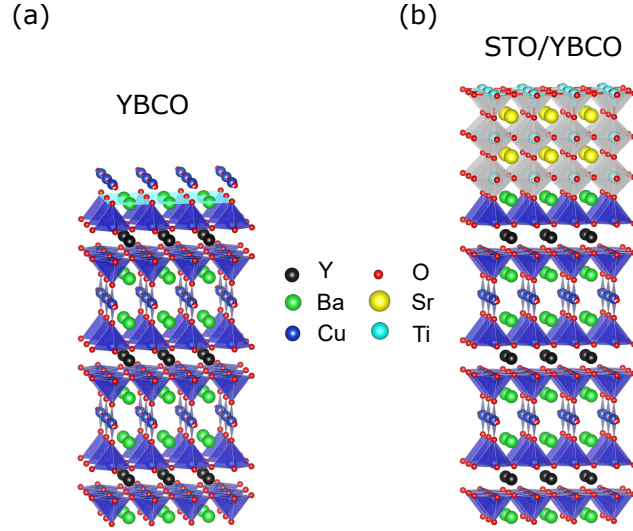


Figure 4.7: 3D view of DFT cells used for calculations, (a) 3 u.c. of YBCO with top CuO chain termination and (b) STO/YBCO structure where the interface lies between TiO_2 and BaO atomic planes. Both structures have been built on BaO planes at the bottom. This particular structure follows the stacking sequence of epitaxial growth on TiO_2 terminated STO (see 3.12).

BaO) to the top layer (nr.18, CuO chains). The FS projections to selected atomic orbitals allow the contribution of each of the planes of this structure to be mapped. Figure 4.8 (a) and (c) show FS contributions in the first BZ of the top CuO chain layer (nr.18) and a bulk chain layer (nr.12), respectively. Both projections are very similar and show an ellipsoid centred at the Γ point which has been observed experimentally in our bare YBCO film (see fig 4.5).

Typical features of bonding (B) and antibonding (AB) bands are also clearly visible in these two projections, which in the literature are assigned to the CuO_2 plane (see section 4.1). Similarly, the chain contributions are present in projections nr.16 and nr.10 which represent CuO_2 planes close to the top surface and bulk, respectively (see fig. 4.8 (b) and (d)). This is an intriguing result which points to the fact that due to the hybridization of the electronic orbitals we cannot really separate the contribution of each plane. This aspect will not be further discussed in the present thesis, but in order to compare the experimental data we will use projections of the FS which include a number of layers that compose at least one entire YBCO cell.

The comparison between surface and bulk is reported in fig. 4.9 (a) and (b),

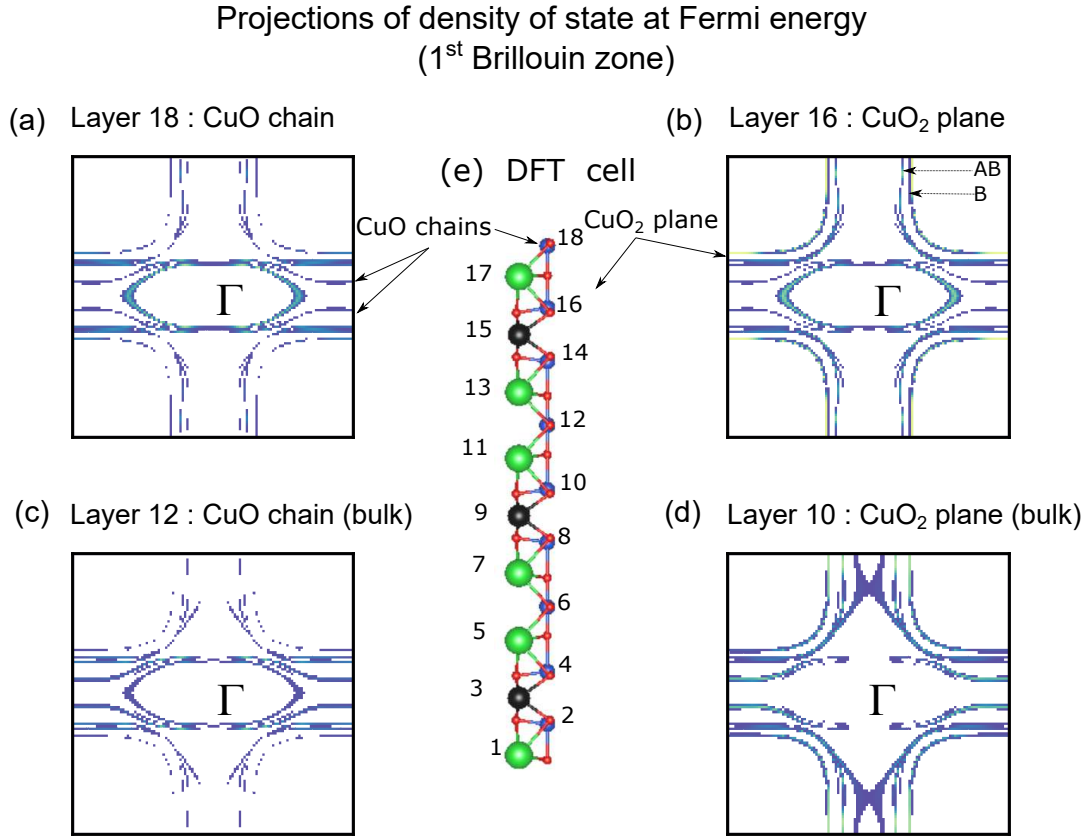


Figure 4.8: Fermi surface (FS) projections of YBCO for different atomic planes. (a) FS of the top CuO chain (nr.18, indicated by arrow), (b) FS of the CuO₂ plane close to surface (nr.16). (c) and (d) the chain (nr.12) and the plane (nr.10) FSs in the inner YBCO cell (Bulk FS). The CuO chain FSs ((a) and (c)) show an ellipsoid centred at the Γ point which has been observed experimentally in our bare YBCO film. Typical features of the bonding (B) and antibonding (AB) bands are also clearly visible in these two projections. Similarly, the chain contributions are present in the projections that represent CuO₂ planes in (b) and (d)). This result points to the fact that due to hybridization we cannot really separate the contribution of each plane. (e) DFT cell used for the numerical calculation. All the planes which compose the YBCO layered structure are numbered from bottom to the top layer (nr.18) which is the CuO termination.

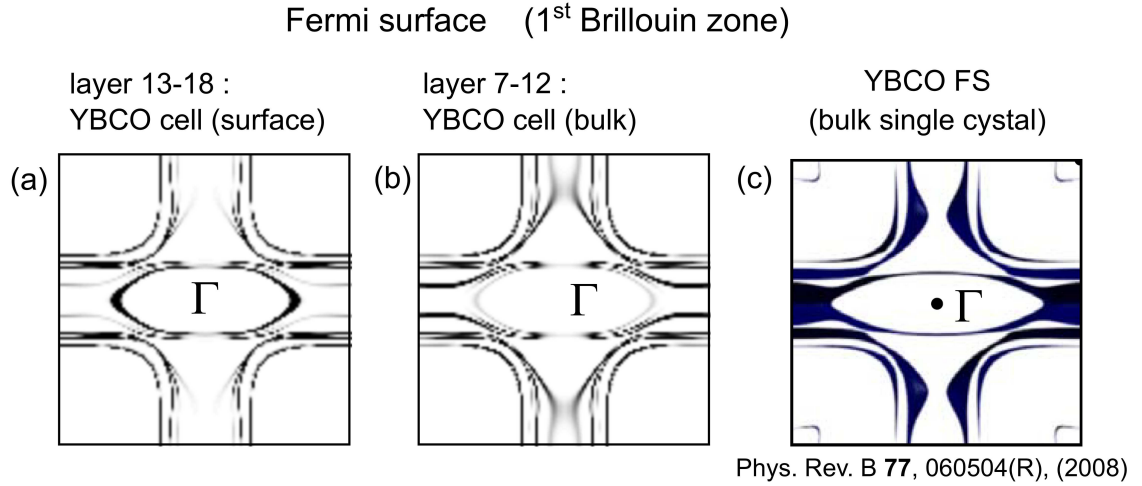


Figure 4.9: Calculated Fermi surface projections of YBCO cells: (a) top cell (layer 13-18 of DFT cell shown in fig. 4.8 (e)), (b) bulk (inner, layer 7 to 12) cell. (c) Fermi surface of the YBCO single crystal extracted from ref. 106. The results of these DFT calculations compare well to one reported in the literature. Small differences in the size of the ellipsoid and A and AB bands could be due to the fact that in the DFT performed for our investigation we used a tetragonal YBCO cell which deviates from the bulk single crystal case.

where FSs of the top YBCO cell (from layer nr.13 to nr.18) and inner cell (from layer nr.7 to nr.12) are shown. The ellipsoid produced by the CuO chain termination is clearly more evident in the top cell but most of the features are similar to the bulk case. The result of this DFT calculation compares well to one reported from literature in fig. 4.9 (c). The small difference in size of the ellipsoid and A and AB bands could originate from the fact that in the DFT performed for our investigation we used a tetragonal YBCO cell (which simulates the strain induced by the substrate) that deviates from the bulk single crystal case.

Comparison of the bare and buried YBCO

Since our film is composed of twinned domains (see chapter. 3), we simulate this distribution by superimposing two calculated FSs with 90 degree rotation. The results of these twinning are summarized in fig. 4.10 (a) and (b), where the FSs of the top YBCO cells are shown for CuO chain termination and for YBCO with a cap STO layer, respectively. The DFT for the CuO termination

reproduces well the two ellipsoids observed in our SX-ARPES of the bare YBCO (see fig. 4.5). This fact confirms the assumption of chain termination of the YBCO film proposed in literature^{57,71}. The calculation of the YBCO cell at the interface with 3 cap layers of STO reproduces FSs which are typical of YBCO bulk and cannot explain the features observed in our measurements (see fig. 4.6 (b) and (c)). The present calculation, however, exclude the fact that the change in FS symmetry observed in our buried YBCO is related to the electronic band structure due to hybridization at the BaO-TiO₂ interface. The nature of the reconstruction observed by SX-ARPES must be related to a different interaction which was not possible to calculate by DFT.

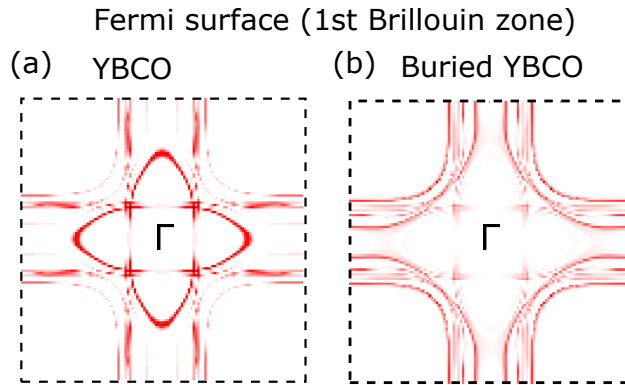


Figure 4.10: Calculated Fermi surfaces of (a) the twinned YBCO film and (b) the YBCO with a STO top layer. The DFT for the CuO termination reproduces well the two ellipsoids observed in our SX-ARPES of the bare YBCO. The DFT calculation of the YBCO cell at interface with 3 cap layers of STO reproduces FSs which are typical of YBCO bulk and cannot explain the features observed in our measurements (see fig. 4.6 (b) and (c))

4.5 ResPES and XAS across the Ti L_{2,3} absorption edge

We have investigated so far the FS of buried and non-buried YBCO where we depicted an influence of the STO interface. We now focus our attention on the STO cap layer in the STO/YBCO structure by performing XAS and ResPES analysis at the Ti L_{2,3} absorption edge. For the experiments we selected films

with STO cap layers of 2, 4 and 10 u.c. thickness, while the underlying YBCO layer was kept to 10 u.c. Resonant energies for Ti 2p \rightarrow 3d transition are in the range from 457 eV to 469 eV. The probing depth for these energies is about 1 to 2 nm (ref. 76). Therefore, in the samples with 2 u.c. and 4 u.c. STO we can definitely probe Ti ions placed at the interface with the YBCO, while, in case of 10 u.c. STO/YBCO, the total thickness of STO cap layer was \sim 2 times higher than the probing depth, not allowing the detection of any signal from Ti ions close to interface. We performed ResPES in order to detect enhancement of the signal intensity for different binding energies at some specific photon energy. ResPES across the Ti L_{2,3} absorption edge enables elemental and chemical state selectivity and gives a direct link to the orbital character of the electron states.

Figure 4.11(a) shows a ResPES intensity map of the 2 u.c. STO sample. On the x-axis, the binding energy of the emitted electrons, on the y-axis, the energy of incident photons are plotted and on the z-axis, the intensity of emitted electrons. Four resonant peaks can be clearly seen at photon energies of about: 465.8 eV, 463.5 eV, 460.5 eV, and 458 eV. These peaks represent transitions from 2p to 3d orbitals (e_g and t_{2g}), as indicated in the figure. These 4 peaks are reported in the literature and are typical for the STO Ti⁺⁴ valence state^{33,107,108}. Additional to these resonant signals, photo-electrons excited from the O 2p band¹⁰⁹ also contribute to the measured electron intensity. These electrons give rise to a background in the ResPES map. This background is shown in fig. 4.11 (b) where the electron intensity integrated for $h\nu=367.8$ eV (indicated by the red dashed line in fig. 4.11 (a)) is reported. At this photon energy, the effect of the resonant Ti signal on the background is minimized. In order to make the resonant peaks more representative, we subtracted this "background" intensity from the full ResPES intensity map.

The result obtained is shown in fig. 4.11 (c). The Fermi energy (E_f) is indicated by the red dashed line. For comparisons with the literature we report Ti ResPES adapted from A. Chickina et al.(ref. 108) in fig. 4.11 (d-f). Here, they have measured the ResPES of Ti at the LaAlO₃/SrTiO₃ interface. Electronic states at E_f are attributed to a two-dimensional electron system (2DES) which appears at the interface of these two insulating materials. Apart from

the 2DES states, fig. 4.11 (f) shows intense in-gap states which are related to Ti³⁺ obtained on purpose by special annealing procedures. In our case, at the STO/YBCO interface, neither electronic states at the Fermi level nor Ti³⁺ in-gap states are observed. The absence of Ti³⁺ or defect-related states in our sample indicate that growth and annealing conditions were sufficiently good to obtain high quality films with negligible oxygen vacancies.

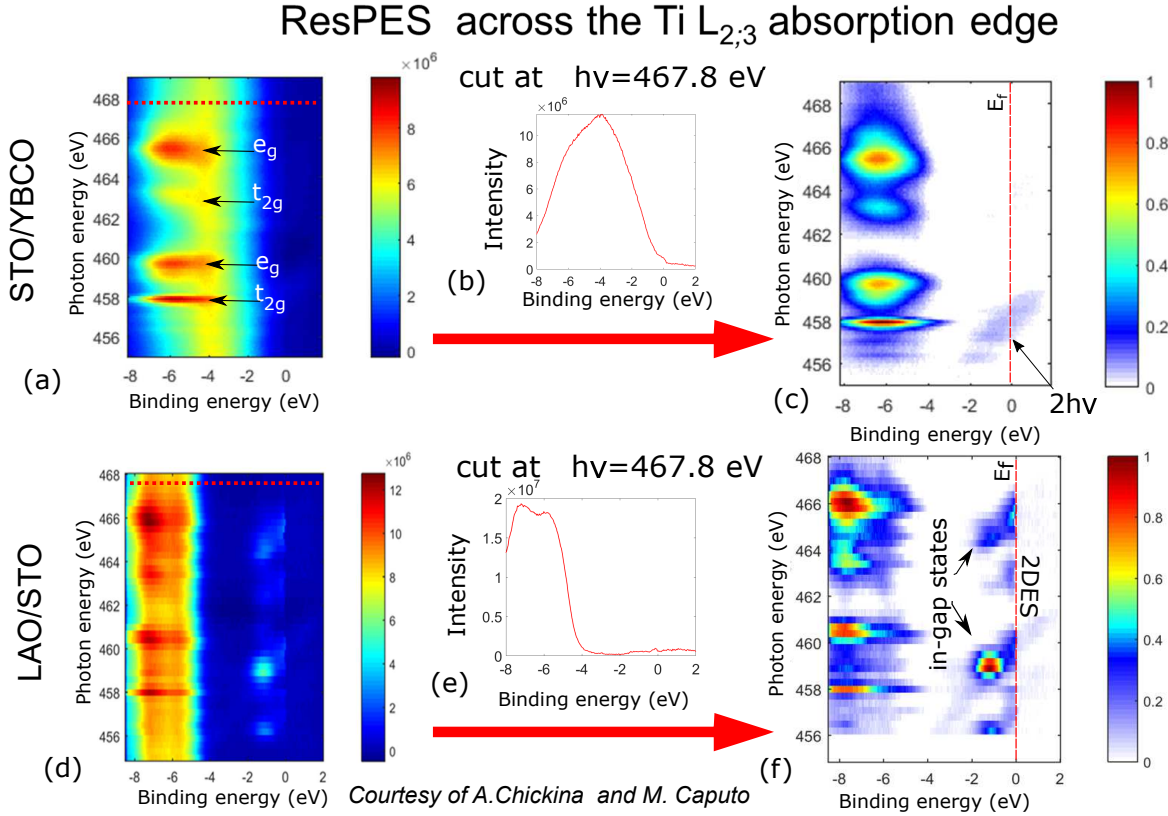


Figure 4.11: ResPES across the Ti L_{2,3} absorption edge of STO(2)/YBCO(10) sample. (b) Electron intensity vs binding energy for $h\nu = 467.8$ eV. (c) Ti⁴⁺ resonant peaks obtained by subtracting background intensity. States close to E_f at 456-459 eV are related to the second-harmonic photon contribution, which is present in this photon energy range due to the Ti 2p signal excited at $2h\nu$ (indicated by arrow on (c)). ResPES intensity map of Ti in LAO/STO system (d), background electron intensity integrated for $h\nu = 467.8$ eV (e) and ResPES after subtracting background intensity (f) (adapted from A. Chickina et. al, ref. 108).

A comparison of ResPES intensity maps for STO 2u.c., 4u.c. and 10u.c. samples are shown in fig. 4.12 (a-c) respectively. Schematic STO/YBCO/STO heterostructures are shown below each ResPES intensity map.

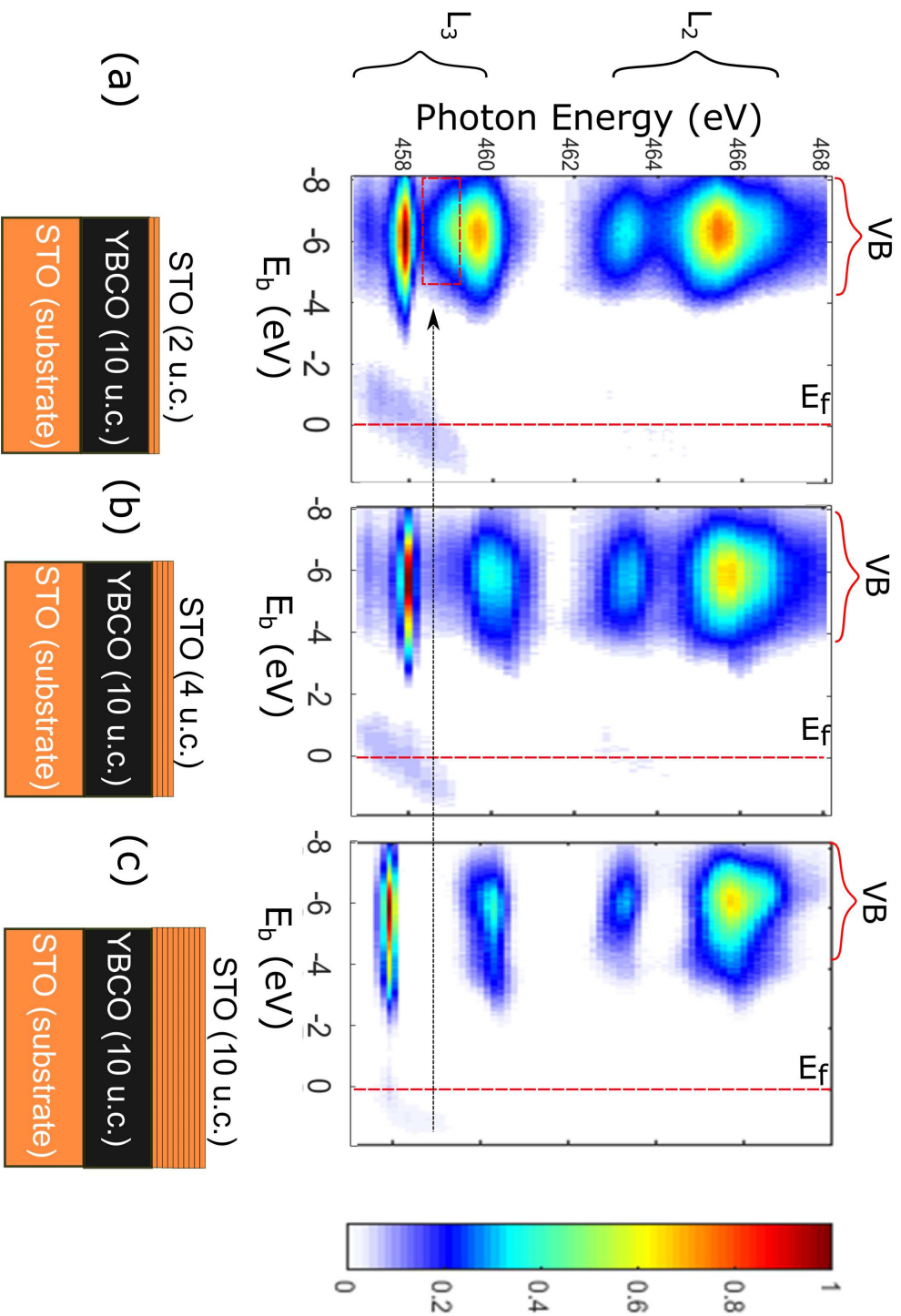
RESPES across the Ti L_{2,3} absorption edge

Figure 4.12: *ResPES* across the Ti $L_{2,3}$ absorption edge for STO films with different thickness: (a) STO(2u.c.)/YBCO(10u.c.), (b) STO(4u.c.)/YBCO(10u.c.) and (c) STO(10u.c.)/YBCO(10u.c.) Each STO/YBCO/STO heterostructures is shown schematically below the corresponding *ResPES* intensity map.

By comparing the ResPES data of the 3 samples, we notice some important differences: In the STO(2) and STO(4) samples the appearance of another signal near the e_g peak is observed exhibiting a peak shoulder in fig. 4.12(a) and (b), respectively. By increasing the thickness of STO this feature is less pronounced. It is completely absent for the STO 10 u.c. and in this case, the ResPES map is equivalent to the one of bulk STO¹⁰⁸. Therefore, we attribute this peak shoulder of the e_g signal to be an effect induced by the YBCO interface.

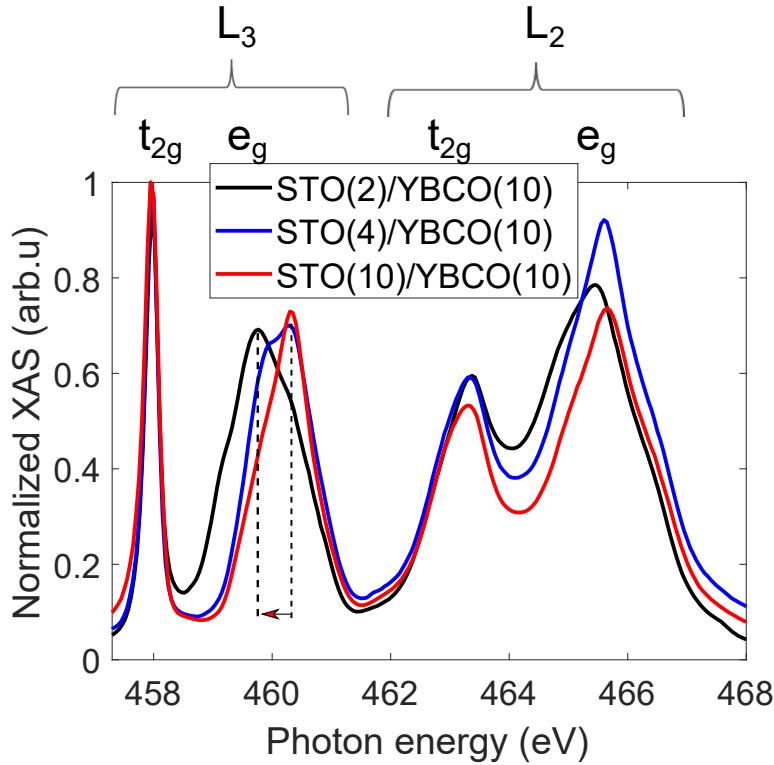


Figure 4.13: (a) XAS across the Ti $L_{2,3}$ absorption edge of STO (2 u.c.) (black), STO (4u.c.) (blue) and STO(10u.c.) (red) films grown on the YBCO(10 u.c.). The region where the shift of the e_g absorption peak is observed in the STO (2 u.c.) sample is indicated by the red rectangular.

In order to investigate the observed effect in more detail, we performed XAS across the Ti $L_{2,3}$ edge on all the samples (see **Chapter 3** for details on XAS). The measurements were performed in total electron yield mode. In this mode, the probing depth is equivalent to that of the ResPES experiment (ref. 110). Therefore we expect a strong contribution from the interface titanium ions to the absorption spectrum in case of the 2 u.c. STO, a weak contribution in the 4 u.c. STO, and almost no contribution in the 10 u.c. STO. The absorption spectra

are shown in fig. 4.13. All lines are normalized with respect to the first, most intense peak at 458 eV. As expected, the XAS on the 10 u.c. STO (shown by red line) reproduces the bulk-like absorption features reported in literature for bulk STO^{82,107,111}. Comparing all these spectra in fig. 4.13, the t_{2g} peaks are well overlapped, while the e_g peaks, similar to the ResPES measurement, exhibit shifts towards lower energy and broadening. Indeed the shift of e_g absorption peaks is observed for both, L₂ and L₃ absorption channels, but in the L₃ peak, it is more apparent.

The e_g peak shape of the STO films of 2 and 4 u.c. suggests that two contributions are present; which we tried to fit using two Gaussian functions. We identified two peaks, one with centered at 459.7(1) eV and the other at 460.5(1) eV. The first peak may represent the Ti⁴⁺ electronic states placed at interface with YBCO, while the second peak is the well-known Ti⁴⁺ state in the bulk STO^{82,107,111}.

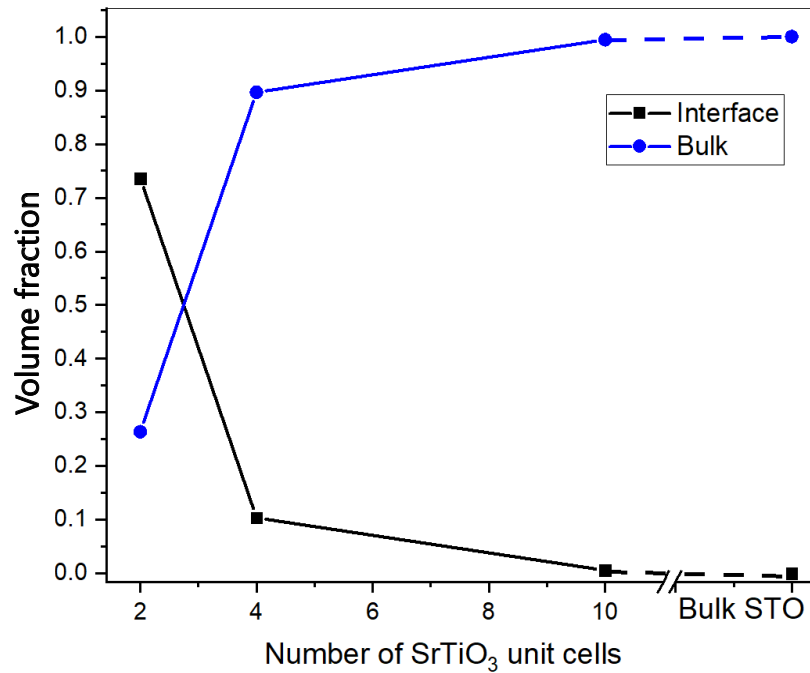


Figure 4.14: Relative contribution of the bulk (blue circles) and interface (black squares) peaks in full absorption e_g peak for different number of STO unit cells. Damping of the interface peak fraction points to the fact that the observed absorption peak occurs only close to STO/YBCO interface. The lines in the figure are guide for the eye.

In order to better visualize the fractional weight contribution of the bulk and interface components of the XAS spectra, we integrated each Gaussian function

and calculated the relative area ratio. Fig. 4.14 shows the fraction of the two components for different number of STO unit cells. Here we assume that the X-ray absorption probability is the same at the interface and in the bulk material. In this way, it is a good approximation to consider the relative integrated area ratio of these two components proportional to the volume fraction of each contribution. The thinnest STO film, where the signal is related to Ti ions placed at the STO/YBCO interface, shows that the "interface" peak, is the most intense, which drastically decreases with STO thickness. This tendency evidently shows that Ti⁴⁺ electronic states are modified at interface with YBCO.

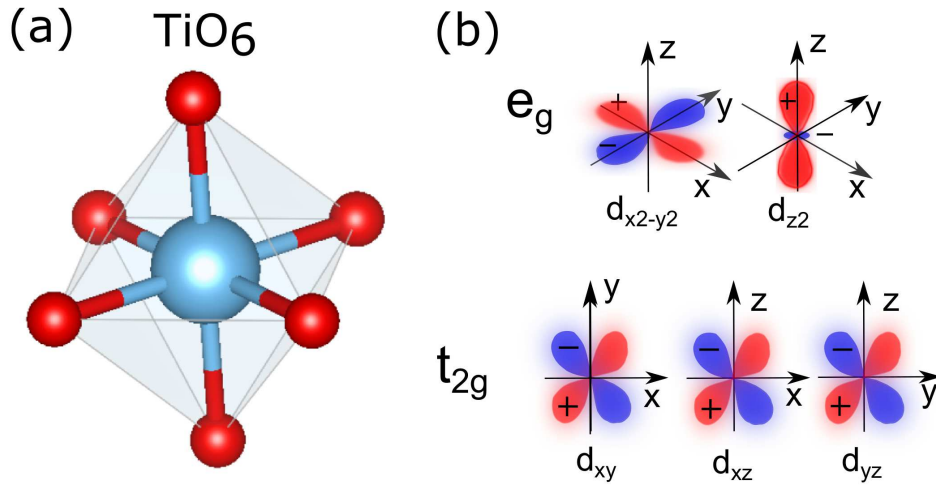


Figure 4.15: Schematic TiO_6 octahedron and (b) t_{2g} and e_g orbitals of the Ti ions. The e_g orbitals are directed towards the octahedral oxygen atoms (apical and in-plane).

In particular, the changes in e_g peaks are related to d_{z^2} and $d_{x^2-y^2}$ orbitals (fig. 4.15), which are directed towards octahedral oxygen atoms (apical and in-plane, respectively), therefore they are sensitive to the displacement of Ti or O ions. In fact, the Electron Energy Loss Spectroscopy (EELS) on the Ti $L_{2,3}$ edge in 2×1 reconstructed STO surface, also shows deviation from the bulk STO¹¹². The EELS also probes 3d levels of Ti ions, similarly to the XAS. In fig. 4.16(a) we report EELS spectra of STO bulk (black line) and surface (red line) Ti ions taken from Zhu et al.¹¹². As can be seen, in case of Ti at the surface, e_g peaks are shifted toward lower energy, similar to our case. These shifts suggest a change of atomic coordination of Ti⁴⁺ located at the surface¹¹³. Zhu et al. investigated the local atomic arrangement of the reconstructed surface using TEM at

the edge of a thin STO foil¹¹². They report that the topmost Ti–O layer shows a significant rearrangement. Figure 4.16 (b) shows an STO(001) TEM image extracted from ref. 112, where oxygen ions (green) in the top STO layer show significant displacement from their original positions. The authors claimed that these displaced atoms are located in rows along the [010] direction (TEM imaging direction). Therefore oxygen atoms are rearranged along the [100] direction without changing location along [010], providing evidences of a 2×1 reconstruction of the STO surface. This surface reconstruction changes the local crystal field environment around the Ti ions and thus the electronic states at the surface are modified.

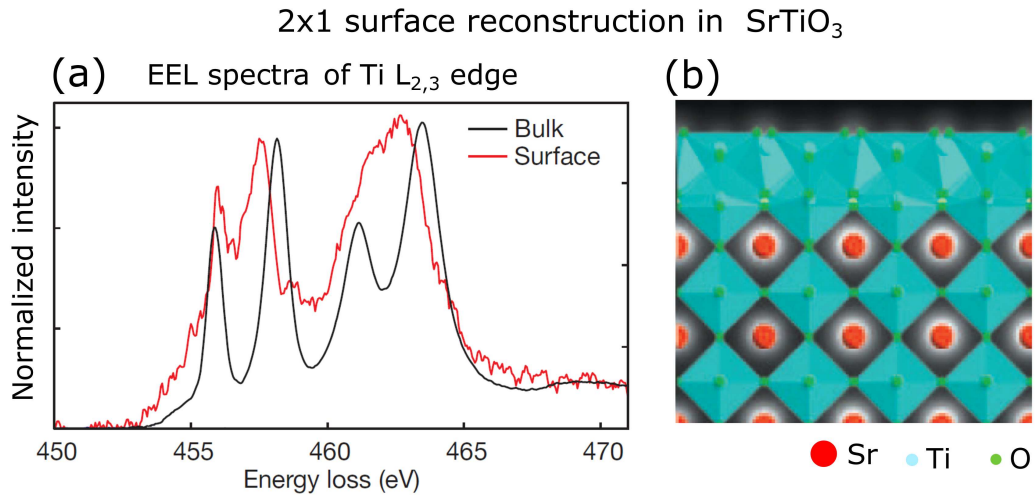


Figure 4.16: (a) EEL normalized spectra of the Ti L_{2,3} edge. (b) TEM image overlaid with a cartoon of STO. Oxygen atoms on the surface show 2×1 reconstruction. (adapted from ref. 112).

In analogy with these findings, we propose that Ti and O atoms in our STO cap layers undergo a structural reconstruction at the interface with YBCO. The observed modification of the e_g absorption peak at the STO/YBCO interface is possibly caused by a structural rearrangement, which also has an influence on the YBCO FS (see Section 4.3).

4.6 2×1 reconstruction at STO/YBCO interface

We investigated YBCO films and YBCO with STO cap layers by soft X-ray synchrotron radiation at the ADDRESS line of SLS, PSI.

In the case of bare YBCO, the FS exhibits a strong contribution from CuO chains. This result can be explained by the fact that the stacking sequence of YBCO grown on TiO₂ terminated STO is expected to produce a top layer of CuO chains^{49,71}. Our result were further confirmed by DFT calculations performed by the group of Daniele Passerone (Empa)

Thanks to the high photon energy range, we could also measure the FS of buried YBCO, which shows a change of symmetry. The observed signal can be explained by a 2×1 reconstruction which takes place at the STO/YBCO interface. XAS and ResPES across the Ti L_{2,3} edge show an energy shift of the e_g peaks of Ti at the interface, which can also be assigned to a 2×1 structural reconstruction.

Here we point to the fact that bare YBCO films have a CuO chain top surface, which guarantees charge neutrality in the film. After deposition of STO, the CuO chains are destroyed due to segregation and/or desorption of Cu (see chapter 3.) As a result, the STO grows on the charged YBCO surface. Interestingly, a similar 2×1 reconstruction has also been observed in STO grown on polar LaAlO₃⁴³. We propose that this could be a general property of high- ϵ STO grown on charged surfaces, in which a distortion of the oxygen octahedron may compensate the polar mismatch.

Importance of controlling SrTiO₃ surface termination

In this chapter I will discuss the importance of STO chemical termination for various interface phenomena. I will report the surface morphology and crystal structure of ultrathin SrO films grown onto TiO₂-terminated STO substrates.

5.1 Importance of surface termination

Epitaxial growth of thin films requires atomically flat substrates. Moreover, the role of chemical termination is important for the appearance of some interface phenomenon, for example, the formation of 2DES at the LAO/STO interface, which is generated only on TiO₂ terminated substrates⁷. Furthermore, the chemical termination of the substrate determines the stacking sequence of the deposited films^{7,114}.

For instance, YBCO deposited on the TiO₂ terminated STO substrate grows with the following stacking sequence: STO-[BaO-CuO₂-Y-CuO₂-BaO-CuO]-... (see chapter 3.4). This sequence defines the top termination of the YBCO film, which is always formed by CuO chains^{49,71}. However, upon deposition of STO on the top, the CuO chains are destroyed (due to segregation and desorption of Cu) and finally the interface lies between BaO and TiO₂ atomic planes. It is not clear what kind of interface will build up if the substrate is prepared with SrO top surface. However, while TiO₂ termination can be obtained by selectively etching

of SrO (chapter 2), until now no reproducible treatments have been reported to produce SrO termination.

In order to obtain a SrO termination, there are two common ways reported in literature: high temperature annealing⁵³ and deposition of a SrO monolayer (ML) on a TiO₂ terminated substrate^{7,115}.

It has been reported that temperature annealing above 1300°C induces Sr extrusion from the bulk to the surface of STO, and produces SrO islands with irregular shapes^{52,53,116}. Only in rare cases, it has been observed that islands smaller than 20 nm have appeared at the edges of the TiO₂ terraces^{12,117}.

Many authors considered the deposition of a SrO monolayer as a good method to impose this new chemical termination^{7,46,115,118}. They assume that this new layer maintains the same lattice parameter of the STO bulk. However, the most stable phase of strontium oxide is the rock salt structure which has a cubic lattice parameter of 0.51 nm^{119,120} which is 30% higher than STO. Therefore, during the deposition of SrO, it is expected that it will grow with a different crystal axis in order to minimize the strain with the substrate. An example of this effect was already observed in the case of SrO deposited on the (001)-oriented LaAlO₃ where the film grows with an in-plane 45° tilt with respect to the substrate principal axis¹²¹.

In this chapter, we report investigation of the surface morphology and crystal structure of SrO epitaxial ultrathin films: from 1 to about 25 layers grown onto TiO₂-terminated STO substrates. X-ray diffraction and transmission electron microscopy analysis show that SrO grows along its [111] direction with a 4% out-of-plane elongation. We found that the distance between the TiO₂ plane and the first deposited SrO layer is 0.27(3) nm, a value which is about 40% bigger than in bulk STO. We demonstrate that a single SrO-deposited layer has a different morphology compared to an ideal atomically flat chemical termination.

5.2 Deposition of SrO film

Several authors report on epitaxial growth of SrO thin films in the temperature range between 600 and 800°C^{7,115,122,123}. Some of them^{122,123} show RHEED in-

tensity oscillations during the deposition of several layers which is typical of the two-dimensional (2D) growth. However, the RHEED intensity signal reported in literature does not show a clear reproducible behaviour of the initial growth.

Figure 5.1 (a-d) shows RHEED intensity oscillations during PLD (a-b) and MBE (c-d) of SrO on a STO substrate extracted from references (115,118,122, 123). While a layer-by-layer growth is observed, some deviations are reported for the first layer. The RHEED reported in fig. 5.1 (d) shows a change in the oscillation period which was explained by a change of the lattice parameter in crystallized SrO from 0.2 nm (first layer) to 0.5 nm (adjacent layers). Here, the authors proposed that the first deposited layer adapts the STO structure, while growth continues with rock salt structure (Schematics of the crystal structures of SrTiO₃ and SrO are shown in fig. 5.1 (e), where the unit cells of each crystal are indicated.). The height of the deposited SrO island measured by scanning tunneling microscopy (STM), exported from Takahashi et al.¹²² is about 0.23 nm (fig. 5.1 (f)), longer than the distance between two adjacent planes in bulk STO, suggesting that even the first layer of SrO is expanded out-of-plane.

In order to understand initial growth of SrO on the TiO₂ surface we investigate the surface morphology and crystal structure of SrO ultra-thin films grown onto STO, with thickness range from one to about 25 layers. During the PLD growth the temperature of the substrate was fixed at 725°C with 100 mTorr oxygen pressure inside the chamber. The distance between the target and substrate was set to 45 mm for all experiments. Two different type of targets were prepared by pressing SrCO₃ (99.995 mol%, Sigma Aldrich) or SrO (99.95 mol%, abcr GmbH) powders and by sintering in air at 750°C and 300°C, respectively. These targets gave similar results for the film deposition, however the SrCO₃ target was more stable in a time range of about two months.

All films were deposited on TiO₂ terminated STO substrates, which were obtained by typical HF etching and oxygen annealing procedures (see chapter 2). The surface topology of each substrate was examined by means of AFM. Only clean crystals, with about 200 nm steps width were selected for film growth. A typical surface topography of a TiO₂ terminated STO substrate is shown in fig. 5.2 (a). The step between each of the terraces is about 0.39 nm, which is one

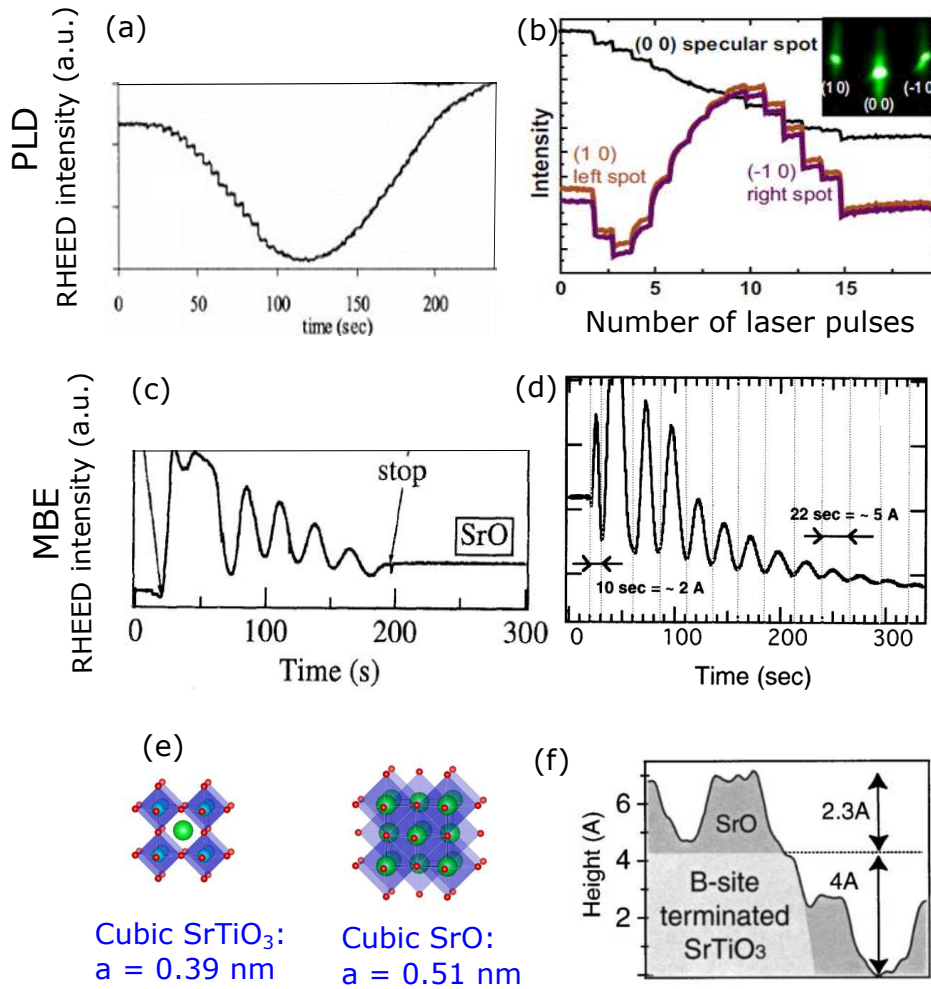


Figure 5.1: RHEED intensity oscillations during SrO deposition onto STO substrate reported in literature. (a) and (b) shows PLD growth of single SrO layer extracted from ref. (118) and ref. (115) respectively. (a) shows a clear oscillation of the specular spot for one layer deposition, while in (b) the specular spot shows continuous dumping. (c-d) RHEED oscillations observed during SrO deposition by MBE (extracted from ref. 123 and 122, respectively). The intensity oscillation of the first 1-2 layers are not reproducible. Takahashi et al. suggested that a change in the periodicity of the RHEED oscillation for the next growing layers (> 1) could be explained by the rock salt phase. (e) schematics of SrTiO₃ and SrO rock salt crystal structures. (f) Height profile of deposited SrO island measured by STM, exported from Takahashi et al.¹²².

unit cell of STO, indicating single chemical termination. The vertical line profile of the atomic step is shown on fig. 5.2 (d).

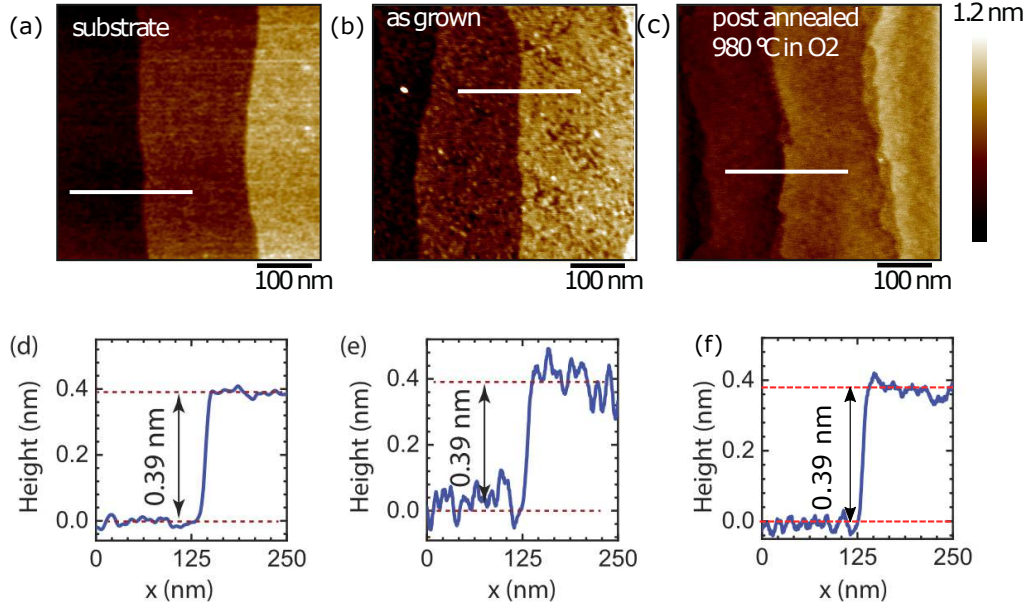


Figure 5.2: AFM surface topographies (a-c) and representative line profiles (d-f) of a TiO₂ terminated STO substrate (a), 1 ML as-grown (b) and post-annealed (c) SrO film. The substrate shows typical step-like morphology with the height of each step of about 0.39 nm. While the pristine substrate has atomically flat terraces, the surface of the as-grown film shows a granular topology. After the annealing the surface roughness reduces from 0.12(1) nm to 0.06(1) nm.

A single layer of SrO deposited at 725°C is shown in fig. 5.2 (b). This layer exhibits a randomly distributed granular surface topology with roughness of 0.12(1) nm. The rough morphology of SrO mono-layers is also reported in literature^{115,122}, which can be related to the low atomic surface diffusion.

In order to overcome this low diffusion condition, we performed post-annealing of the film at about 980°C for 5 h in oxygen. This temperature will enhance diffusion of atoms on the surface, but it is not sufficient to induce Sr desorption¹²⁴, therefore as a result of the annealing, a reorganization of the SrO surface is expected. Indeed, after annealing the surface roughness decreased from 0.12(1) nm to 0.06(1) nm (fig. 5.2 (c)).

Deposition and subsequent post annealing of the SrO films produce smooth surfaces also in case of thicker films. AFM surface topographies of 3 and 5 layers of SrO after oxygen annealing are shown in fig. 5.3 (a) and (b), respectively.

Step-like topography of the substrate is preserved in both cases.

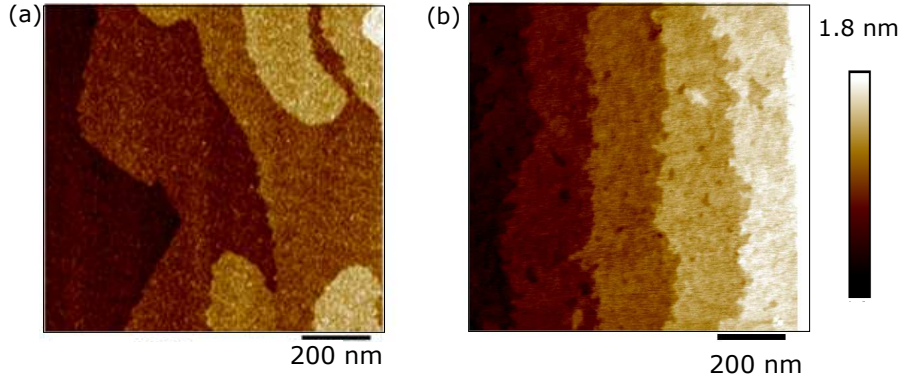


Figure 5.3: AFM topographic image of about (a) 3 and (b) 5 u.c. of SrO deposited at 725°C and post-annealed at 980°C in oxygen. Step-like topography of the substrate is preserved in both cases.

Deposition of the SrO film at 725°C and subsequent high temperature annealing (980°C, for 5 h.) results in a smoother surface topography. This observation points to the enhanced surface diffusion of strontium at high temperature, suggesting that with a partial coverage of 20% to 80% of the surface, large self-organized patterns composed by SrO islands on TiO₂ could be obtained by high temperature annealing.

In order to test this idea, we deposited an amount of SrO which covers only about 80% of the substrate. Figure 5.4 (a) shows this SrO film deposited at 725°C. AFM shows nearly homogeneous coverage of the substrate surface. The roughness of this surface is 0.12(5) nm, the same value as in case of 1 ML SrO (fig. 5.2 (b)). After annealing in oxygen, the surface topography is drastically modified, as shown in fig. 5.4 (b), and a relative smooth ($R_q = 0.08(5)$) and compact surfaces nucleates at each edge of the substrate terraces. Since the surface is covered partially, an uncoated TiO₂ area is clearly visible in the AFM z-scan. This is also confirmed by the AFM phase-contrast imaging shown in fig. 5.4 (c) where the SrO islands correspond to the dark gray and the TiO₂ are represented by the white contrast.

The topography of the obtained pattern is schematically shown in fig. 5.4 (f). Similar SrO-TiO₂ patterns have been used by other authors for the selective growth of SrRuO₃ stripes^{12,14} with a typical width of 100 to 200 nm. In case of post annealed partially coverage by SrO, we obtained narrower TiO₂ islands,

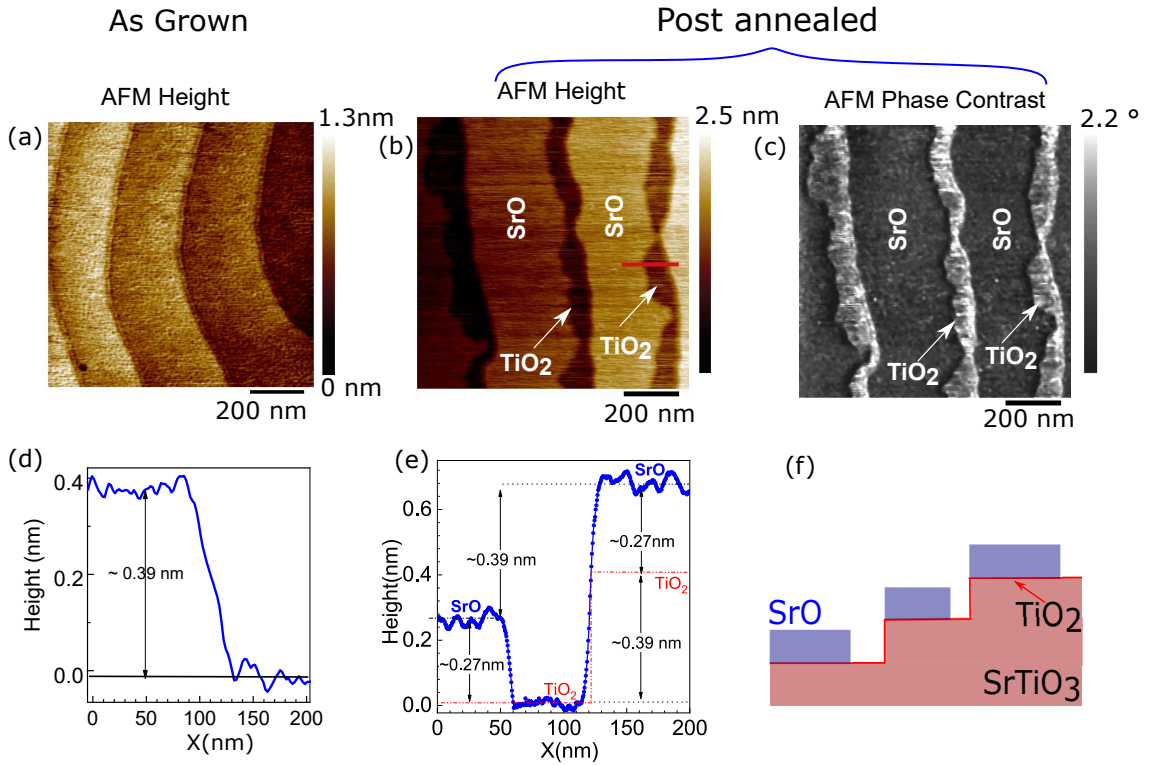


Figure 5.4: AFM topography of a SrO film with a partial coverage (80%) deposited on pristine TiO₂ termination: (a) as grown film, (b) film post annealed at 980°C in oxygen. Height profiles of of selected area of the two AFM scans are reposted in (d) and (e) respectively. (c) AFM phase contrast of post annealed film shows evidence of mixed terminations. (f) Schematic surface cross-section.

about 40 nm. Our experiment suggest that by increasing the SrO coverage one could potentially reduce the TiO₂ terraces to a few nanometres, a condition which may be used for selective growth of quasi-one dimensional nano-filaments.

These uncoated regions allow us to quantify the distance between the TiO₂ and the SrO planes, and by performing a line profile analysis across 10 different steps we found an average value of SrO 0.27(3) nm (see fig. 5.4 (e)).

An instrumental AFM offset across the two different materials (SrO and TiO₂) was estimated to be about 0.01 nm by measuring the TiO₂-SrO-TiO₂ intermediate steps in the selected substrate. These terraces are residuals of SrO that survive to a fast HF etching, similar to the cases reported in literature^{53,117} (see more details is appendix II). The low value of this offset proves that the height of the deposited SrO is about 40% bigger than in bulk STO. It is comparable to the height of 0.23 nm reported by Takahashi et al.¹²². SrO deposited on the surface

has a different morphology respect to the ideal chemical termination that one would expect and a single SrO top layer behaves differently compared to the bulk.

5.3 Structural properties of ultra-thin SrO

In order to characterize the strain of SrO with STO substrate we deposited a thicker film of about 8 nm. In this case the behavior of the rock salt phase could be different with respect to the case of one single SrO plane. However, this film allows us to measure the strain generated at the interface by means of X-ray diffraction.

The XRD θ - 2θ scan reported in fig. 5.5 (a) shows only one SrO line at 28.7°. The closest reflection line of rock salt^{119,120} is (111), therefore this is the preferential direction of the growth of SrO on the (001)-oriented substrates. From this line we could estimate (Bragg's equation) that the distance of two adjacent Sr planes along the [111] direction is about 0.3096 nm, which indicates an elongation of about 4% with respect to the unstrained case (0.298 nm). By using the Scherrer equation¹²⁵ we estimated, from the full width at half maximum of this reflection line, a film thickness of about 8-9 nm. This value was confirmed by TEM analyses, shown later in this chapter.

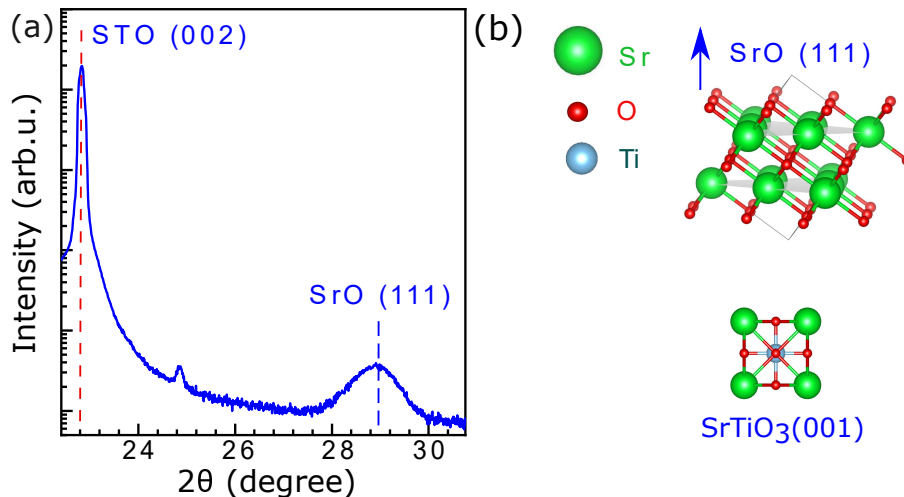


Figure 5.5: XRD θ - 2θ scan of SrO. Peak at 28.7° degree indicates (111) growth orientation. (b) Schematic structure of SrO(111) and STO(001).

Schematics of SrO(111) and STO(001) are shown in fig. 5.5 (b). In this orien-

tation the SrO structure is composed of alternating strontium and oxygen atomic planes. In fig. 5.6, we attempt to describe how the SrO rock salt structure could adapt to the STO geometry, despite the large mismatch. The [111] growth direction of SrO results in a honeycomb-like hexagonal in-plane structure (fig. 5.6 (a)). Here, rectangular periodic structures of $1.264 \times 0.365 \text{ nm}^2$ could adapt (under strain) to the $1.175 \times 0.390 \text{ nm}^2$ of the TiO₂ surface (which corresponds to 3 STO u.c., fig. 5.6(b)). The calculated pole figure of both STO and SrO undistorted lattices is shown in fig. 5.6 (c), where 3-fold symmetry of SrO(111) provides 3 spots. However, due to the fact that the in-plane configuration of the substrate has a 4-fold symmetry, each 90° rotation of the SrO with respect to STO will produce a new possible match. This is schematically explained in fig 5.6 (d). Here we represent hypothetical φ -scan of SrO(111) film. One specific in-plane orientation of SrO provides 3 peaks in φ -scan separated by 120° due to 3-fold symmetry of (111)-oriented SrO (dashed lines). However, 90° rotation also gives possible match with the substrate, therefore there are 3 more peaks shifted by 90° with respect to the original one (dash-dot lines). Other 180° and 270° rotation from the original position, also produce possible match condition (dotted and solid lines). Therefore 3 peaks are expected for each of the 4 possible matches resulting in 12 equally spaced peaks for SrO.

Experimental φ -scans of the SrO {111} and STO {111} planes are reported in fig. 5.7 where the substrate produces four intense peaks, as expected for the STO crystal structure. The SrO φ -scan, although low in intensity, show indeed a periodic intensity modulation every 30°, compatible with the 12 expected reflection lines explained above. The large lattice mismatch with the STO underneath may cause dislocation formation and compressive in-plane strain which could explain the 4% out-of-plane elongation of SrO along the [111] direction as measured by XRD. The model presented above is just a possible scenario for the in-plane alignment. However, we cannot exclude the presence of interface disorder.

In order to confirm the presence and out-of-plane elongation of these domains, we perform TEM analysis of the SrO film. A representative selected region is shown in the TEM micrograph of fig. 5.8. The lamella was imaged along the [100] direction of STO substrate as shown by the fast Fourier transform (FFT)

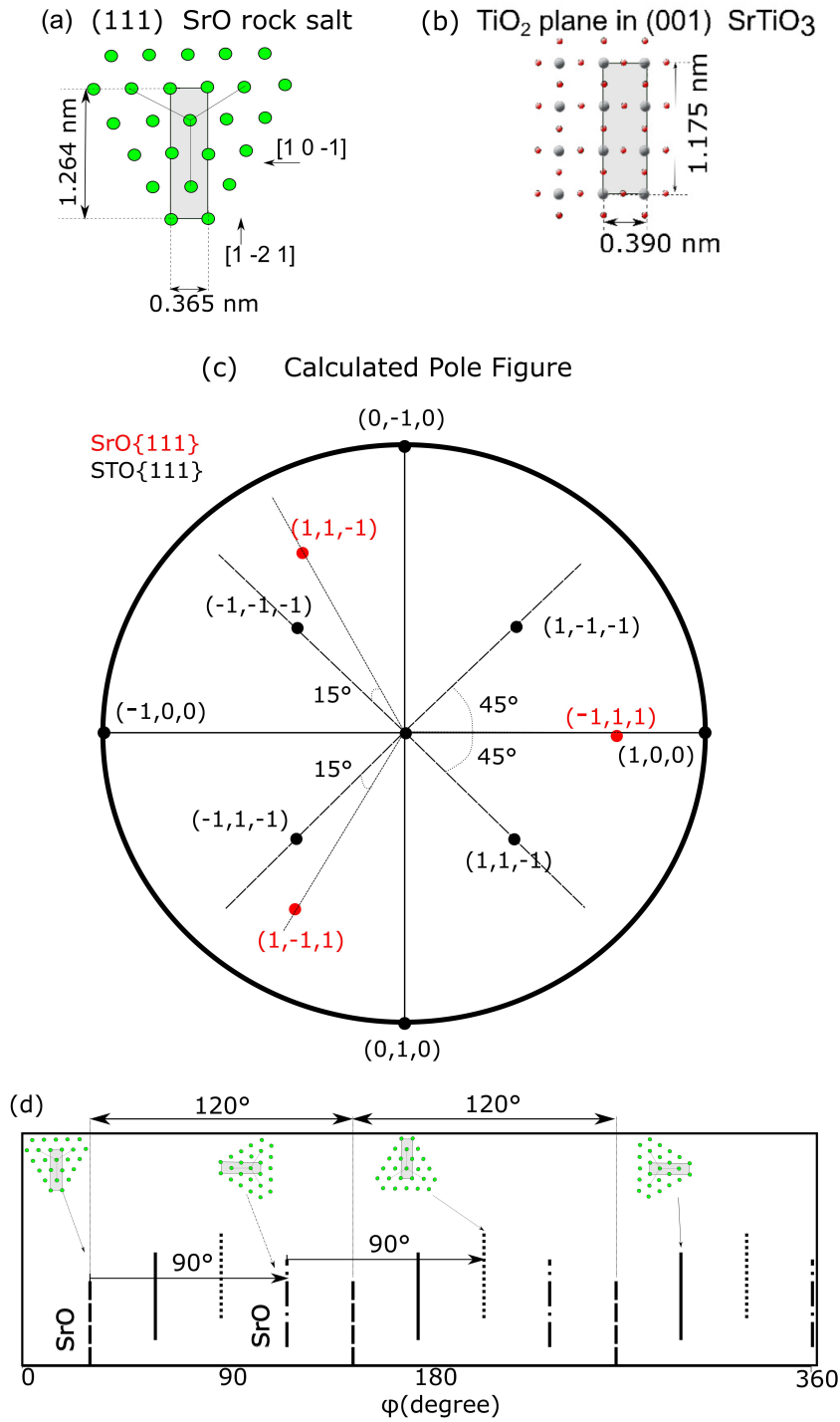


Figure 5.6: (a) Sr plane in (111) oriented SrO rock salt. Rectangular periodic structures of (a) $1.264 \times 0.365 \text{ nm}^2$ could adapt (under strain) to the $175 \times 0.390 \text{ nm}^2$ of the TiO₂ surface (b). (c) Theoretical pole figure for SrO {111} and STO {111}. (d) Ideal φ scan of SrO (111), due its 3-fold symmetry 3 peaks are expected separated by 120° (indicated by dashed line). However, a 90° degree rotated SrO(111) domain also can match with the substrate. As a result, SrO 3 peaks are repeated after 90° (dash-dot line), 180° (dotted line) and 270° (solid line) and in total 12 peaks are expected in the φ -scan measurement.

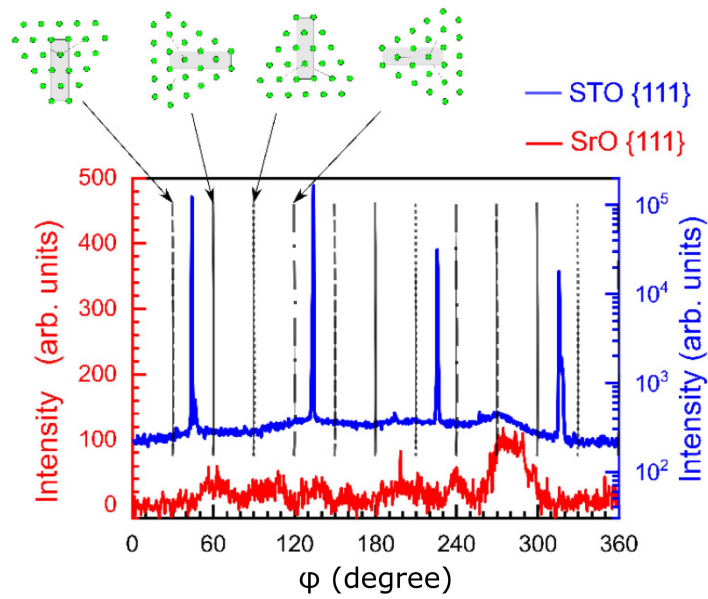


Figure 5.7: Experimental φ -scan acquired around the STO{111} reflection (in blue at a tilt angle of 54.3°) and around the SrO {111} reflection (in red at a tilt angle of 70.5°). The positions of 12 expected reflection lines of SrO {111} are indicated and schematically shown on top of the figure, which represent four different in-plane orientations of the SrO domains as indicated in fig. 5.6(d).

on the inset of fig. 5.8. The film is composed by nano-domains separated by extended defect regions like stacking faults or other dislocations. The in-plane width of the domains is about 20 to 30 nm.

Figure 5.9 shows a TEM image of a SrO film grown on STO and fast Fourier transform of TEM patterns of SrTiO₃ (b) and SrO (c) selected regions. From the FFT analysis of the film shown in fig. 5.9 (c), we estimated a distance of two adjacent Sr planes of about 0.31(2) nm, which is in agreement with the XRD measurement.

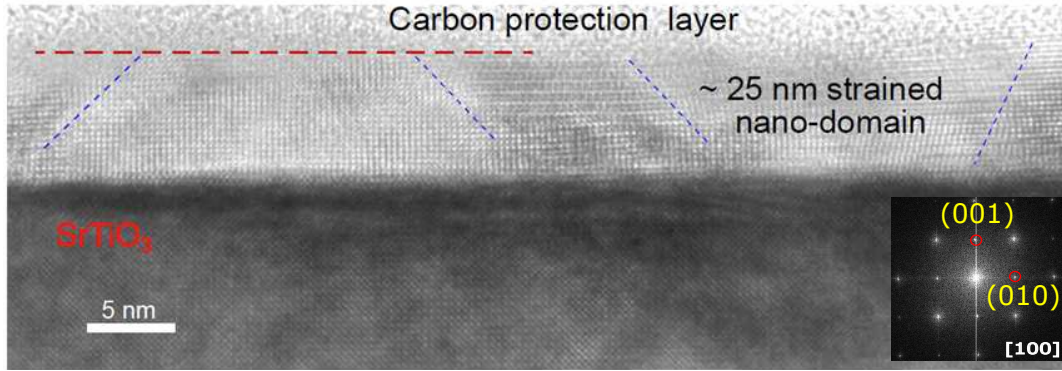


Figure 5.8: TEM image of the SrO film grown on STO. The fast Fourier transform (inset) indicates the $[100]$ zone axis of the substrate. The domain boundaries are indicated by blue dashed lines. The red dashed line indicates the interface between SrO film and the carbon protection layer deposited for the lamella preparation.

Additionally, we found the following orientation relations between the substrate and the film: out-of-plane $[0\ 0\ 1]$ STO \parallel $[1\ 1\ 1]$ SrO, and in-plane $[1\ 0\ 0]$ STO \parallel $[1\ 0\ -1]$ SrO. These orientations are in agreement with the model presented in fig. 5.6 and are consistent with the XRD pattern in fig. 5.5. Hence, we deduce that our film consists mainly of (111) oriented SrO domains. However, we can not exclude the presence of a small fraction of other domain orientations due to the lattice mismatch which could introduce interface disorder.

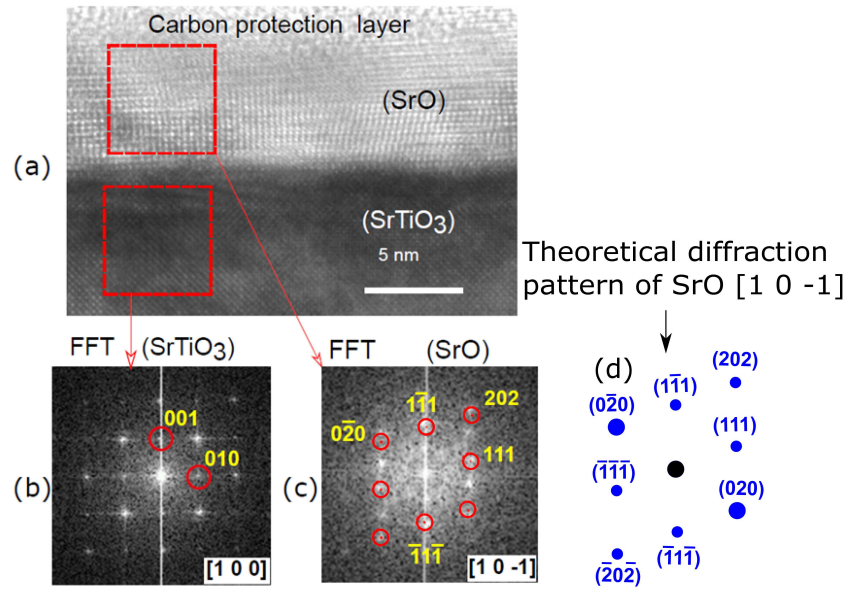


Figure 5.9: (a) TEM image of SrO film grown on STO. Fast Fourier transform of TEM pattern of SrTiO₃ (b) and SrO (c) selected regions. Here (111)-oriented SrO domain is clearly visible with the following orientation relations: out-of-plane $[001]_{STO} \parallel [111]_{SrO}$ and in-plane $[100]_{STO} \parallel [10-1]_{SrO}$. (d) Theoretical diffraction pattern of SrO $[10-1]$.

Figure 5.10 (a) shows a TEM image of the SrO film at another region and FFT of TEM patterns of selected regions of SrTiO₃ (b) and SrO (c). Here, we observe superimposed diffraction pattern of two SrO domains imaged along the $[1 0 -1]$ direction. Theoretical diffraction pattern of these two domains are shown in fig. 5.10 (e) and superposition of them in fig. 5.9 (f). Both domains fulfil out-of-plane orientation relations: $[0 0 1]_{STO} \parallel [1 1 1]_{SrO}$, in agreement with the model presented in fig. 5.6. The presences of more than one domain in TEM image is related to the thickness of the lamella (~ 100 nm) which is larger than size of each domain (~ 30 nm) and therefore we are imaging several domains at the same time.

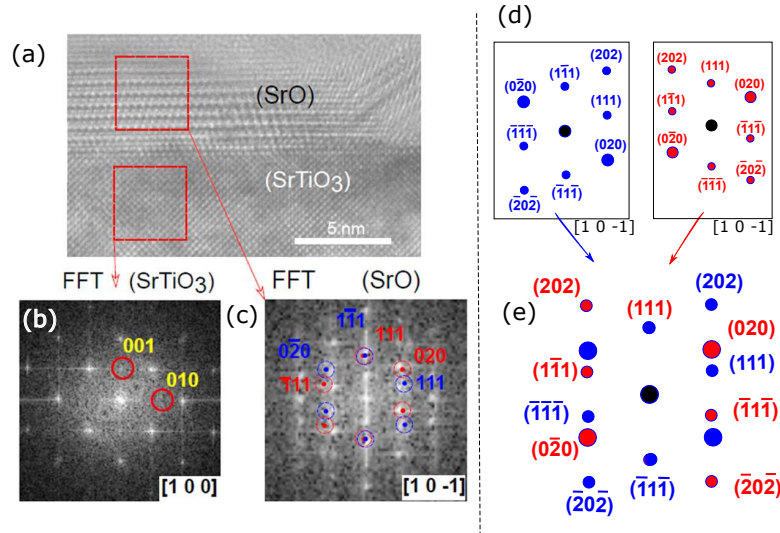


Figure 5.10: (a) TEM image of the SrO film grown on STO. (b) Fast Fourier transform of TEM patterns of SrTiO₃ and (c) SrO selected regions. Here, we observe superimposed diffraction patterns of two SrO domains imaged along $[1\ 0\ -1]$ direction (indicated by red and blue circles). (d) Theoretical diffraction pattern of these two domains with different in-plane orientation and (e) their superimposed image.

5.4 Summary

We investigate the surface morphology and crystal structure of SrO epitaxial ultrathin films: from 1 to about 25 layers grown onto TiO₂-terminated STO substrates.

We observed self organized patterns that form when we deposit less than one layer (coverage of about 80%). Here, a relatively smooth and compact surface nucleates at the edge of TiO₂ terraces and leaves empty space before the next terrace step. This particular topology allowed us to measure that the average height of deposited SrO is about 0.27(3) nm. A similar value has been observed already by Takahashi et al.¹²² and it is substantially different from 0,19 nm which is the distance between SrO-TiO₂ planes, expected in bulk STO.

XRD and TEM showed that SrO grows preferentially along its $[111]$ direction. In this orientation, the SrO lattice size matches better with the substrate. Even if lattice mismatch at the interface is reduced, an out-of-plane elongation of 4% was clearly observed by TEM and XRD along the $[111]$ direction. We propose that this large strain is also responsible for self-organized patterns formed in the

initial growth of SrO.

It has been shown that STO can be grown by depositing alternating SrO and TiO₂ monolayers¹²⁶⁻¹²⁹. In this special case the TiO₂ deposited on top of SrO forces the entire structure to organize like in the bulk STO, probably due to the strong covalent bonding of the oxygen octahedron which determine the lattice size. However, we found that a single SrO top layer is intrinsically different from the bulk case, and cannot be considered an atomically flat chemical termination. These results have been published in "Science and Technology of Advanced Materials", VOL. 20, NO. 1 2019 (see paper II in list of publication on page 106).

Conclusions and Outlook

We investigated the STO/YBCO interface in multilayer heterostructures produced by PLD. The interface which forms by depositing STO on YBCO was found to show a better crystal quality than the one with the substrate. This interface was investigated with synchrotron radiation by SX-ARPES in the photon energy range of 800 to 900 eV, which allowed to detect YBCO buried by a few STO cap layers (till about 2 nm).

The bare YBCO Fermi surface measured by SX-ARPES exhibited strong contribution from the CuO chain, expected when growing on TiO₂ terminated substrate. This result was further confirmed by DFT calculations.

Compared to the low energy ARPES experiment (below 100 eV) reported previously by Sassa et al.⁴², we have found an improved signal to noise ratio in the first BZ, which allowed a better comparison with theoretical calculations. Moreover, thanks to the higher photon energy, we could detect the complete FS in large k -space without performing numerical reconstruction. We were able to measure and to report for the first time the FS of YBCO buried underneath 2 and 4 u.c. of STO. This was possible only due to the larger IMFP of photoelectron when using soft X-ray photons.

We observed changes of the FS in buried YBCO, which are compatible with a 2×1 reconstruction at this interface. XAS and ResPES performed across Ti L_{2,3} edge confirmed this result in the STO side as well.

Therefore both YBCO and STO showed evidence of a 2×1 reconstruction when stacked on top of each other. Since a similar phenomenon has been observed

in STO grown on polar LAO⁴³, we proposed that this is a general property of high- ϵ STO grown on charged surfaces, in which a distortion of the oxygen octahedron may compensate the polar mismatch.

In the second part of this thesis we have reported a systematic investigation of a SrO-terminated STO substrates. In YBCO/STO heterostructures, the only interface reported in literature lies between BaO-TiO₂ atomic planes. One can potentially change this interface by depositing YBCO on SrO-terminated STO substrate. Until now, a reproducible chemical treatment for the SrO terminations has not yet been achieved. One possible strategy, suggested in literature, is the deposition of SrO monolayer onto previously prepared TiO₂ terminated STO substrate.

We have performed structural analysis of deposited SrO films from less than one layer up to 25 layers. We observed special self-organized patterns that form when we deposit less than 1 layer (coverage of about 80%). A relatively smooth and compact surface is nucleated at one edge of TiO₂ terraces and leaves empty space before the next terrace step in a parallel stripe island pattern. The average height of deposited SrO derived by AFM analysis was about 0.27(3) nm, substantially different from 0.19 nm, i.e. the distance between SrO-TiO₂ planes, expected in bulk STO. We found that this mismatch is due to the strain associated to the preferential growth direction of SrO along [111].

It has been reported the possibility to grow STO by depositing alternating SrO and TiO₂ planes¹²⁶⁻¹²⁹. Here, TiO₂ deposited on top of SrO forces the entire structure to organize like in the STO bulk. However, we found that a single SrO top layer is intrinsically different from the bulk case, and cannot be considered an atomically flat chemical termination.

Outlook

We observe a 2x1 reconstruction of STO at the interface with a YBCO film and propose that this could be a general property of high- ϵ STO grown on charged surfaces. To clarify the role of the dielectric constant on this effect, we suggest studying the interface of YBCO with a material having different ϵ such

as Sr_{1-x}Ca_xTiO₃¹³⁰ or KTa_{1-x}Nb_xO₃^{131,132}. In these systems, doping induces a ferroelectric transition in the 10 K-50 K and 90 K-140 K temperature ranges, respectively and enhances the value of ϵ .

We conclude that it is not possible to observe the expected enhancement of T_c at the YBCO/STO interface because here CuO chain are always destroyed upon STO deposition. This produces a charged interface as shown in chapter 3.4. Hence, we suggest to explore the interface of high- ϵ material with other cuprates. One possible candidate could be La_{2-x}Sr_xCuO₄ (LSCO), which can be stacked into a heterostructures with a better quality interface. Indeed in ultrathin films of LSCO, T_c is not suppressed¹³³⁻¹³⁵, unlike the case of YBCO. Additionally, although good quality epitaxial growth was achieved during these investigations, some problems in measuring the hole doping levels in YBCO were encountered. Since oxygen vacancies have a high mobility, it was not possible to exclude self-organization of these vacancies which would change the doping level in YBCO layers near the interface. Because of this problem, we suggest using LSCO HTS, where the hole doping is controlled chemically by the Sr content. In this case, the LSCO/high- ϵ interface could also be investigated in the underdoped regime, where an increase of T_c is predicted³⁵.

Appendix I

In this Appendix we present SX-ARPES experimental results which are not shown in main text. First, as described in chapter 4, we performed photon-energy dependent measurements (fig. 6.1) in order to select the excitation energy which gives higher SX-ARPES signal. Photon energies that we select for the FS measurement are indicated by arrows in fig. 6.1.

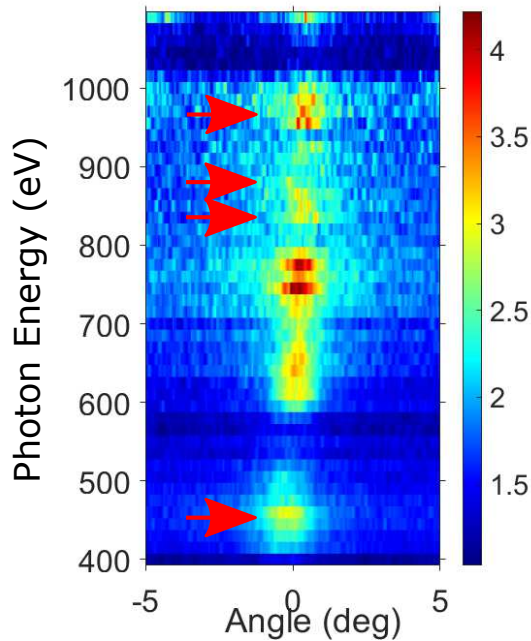


Figure 6.1: Photon energy dependence of photoelectron intensity for emission angles between -5 to 5 degree. The photon energies which were used for the FS measurements are indicated by arrows.

In section 4.1.1 we show that a photon energy higher than 600 eV is required to measure buried YBCO. However, we also perform experiments with relative

lower photon energy ($h\nu=457$ eV) on bare YBCO film (fig. 6.2). The measured FS also shows CuO-chain-related features. The ability to clearly observe CuO chain states in the FS indicates that 457 eV can successfully overcome surface contamination problems of ex-situ prepared YBCO films.

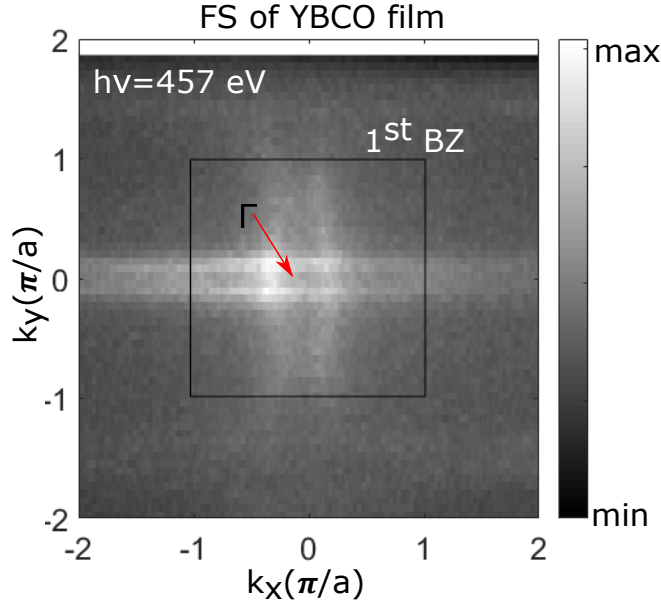


Figure 6.2: Fermi surface of a YBCO film measured at 457 eV photon energy. The 1st BZ and the Γ point are indicated in the figure. The measured Fermi surface shows CuO-chain-related features such as one measured at 840 eV (see fig. 4.5) .

YBCO films covered by 2 u.c. STO were measured by 975 eV and 870 eV photon energies. These measurements are shown in fig. 6.3 (a) and (b), respectively. Both FSs show change in symmetry compared with the FS of bare YBCO, and confirm observed reconstruction at 840 eV photon energy (discussed in chapter 4). FS measured at 870 eV photon energy (6.3 (b)) shows a small tilt due to misalignment of the sample (more details about alignment is discussed in 3.6)

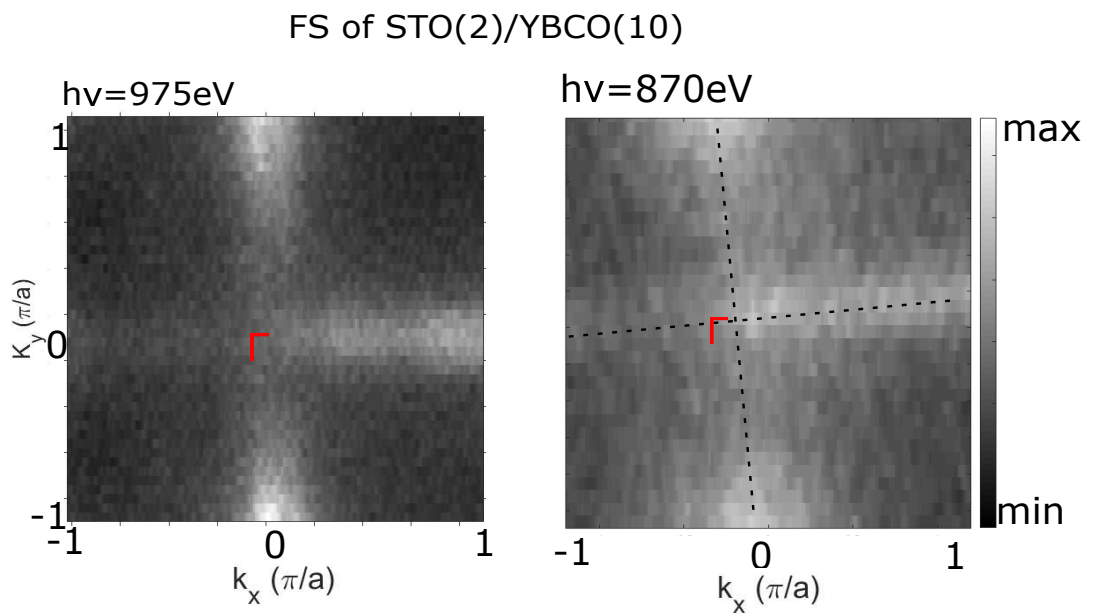


Figure 6.3: Fermi surface (FS) of buried YBCO measured at (a) 975 eV and (b) 870 eV photon energies. Both FSs show change in symmetry compared with bare YBCO and confirm the observed FS reconstruction (discussed in chapter 4).

Appendix II: AFM calibration

We use atomic force microscopy operating in tapping mode to measure the height of SrO islands deposited on STO (see chapter 5). In this mode, when the tip is crossing two different types of materials, an offset in the height response of the tip could be expected. In order to estimate this off-set, we perform height profile analyses of the $\text{TiO}_2\text{-SrO-TiO}_2$ steps which form on the substrates due to a partial chemical etching^{53,117}. This kind of intermediate terraces are residuals of SrO that survive a fast HF etching. In fig. 6.4 we report the AFM surface topography of a (001) oriented STO substrate after HF etching and oxygen annealing at 950°C. In this special case an intermediate SrO step appears as a shadow close to the step of the TiO_2 terraces.

By performing a vertical line cut analysis across 9 selected steps we measured an average height of 0.18(2)nm for these special SrO intermediate steps. Since the theoretical value of this step is half of the lattice parameter of STO (0.195 nm), we can conclude that in our set-up, the AFM offset for the two different terminations is about 0.01 nm.

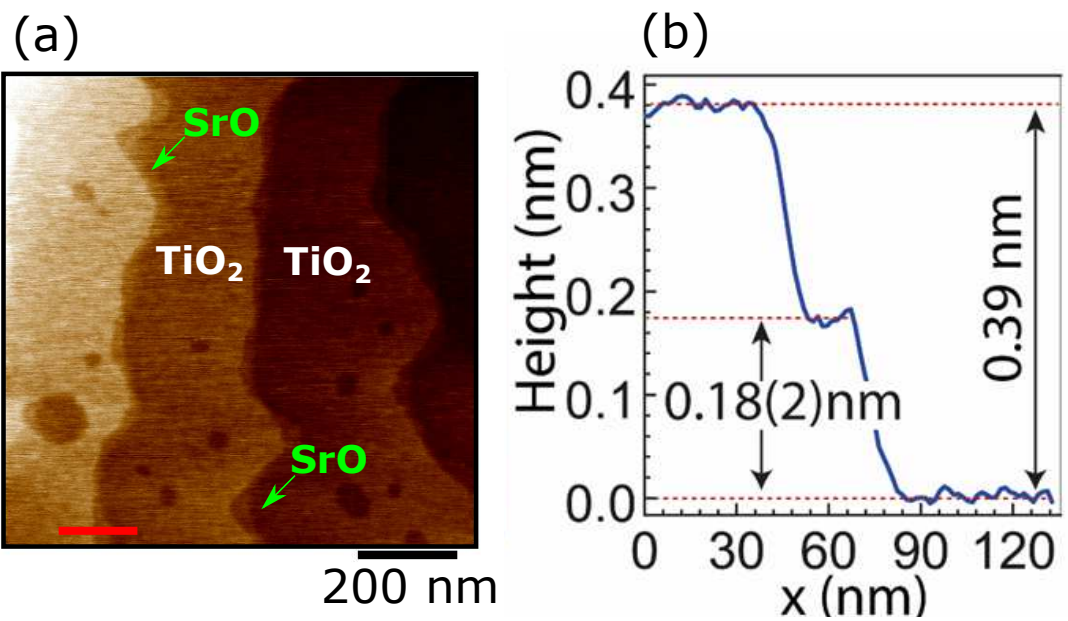


Figure 6.4: (a) AFM surface topography of a (001) oriented STO substrate after HF and oxygen annealing at 950°C. (b) Vertical profile across a selected edge (indicated by red line on (a)). In this case a partial etching (short exposure to the HF) causes a residual presence of SrO at the edge between two TiO₂ terraces.

Bibliography

- [1] R. W. Keyes, *Reports on Progress in Physics*, 2005, **68**, 2701–2746.
- [2] S. M. Sze and K. K. Ng, *Physics of Semiconductor Devices*, A JOHN WILEY & SONS, 3rd edn., 2007.
- [3] N. Z. Haron and S. Hamdioui, 2008 3rd International Design and Test Workshop, 2008, pp. 98–103.
- [4] J. Mannhart and D. G. Schlom, *Science*, 2010, 1607–11.
- [5] M. Lorenz, M. S. Ramachandra Rao, T. Venkatesan, E. Fortunato, P. Barquinha, R. Branquinho, D. Salgueiro, R. Martins, E. Carlos, A. Liu, F. K. Shan, M. Grundmann, H. Boschker, J. Mukherjee, M. Priyadarshini, N. Dasgupta, D. J. Rogers, F. H. Teherani, E. V. Sandana, P. Bove, K. Rietwyk, A. Zaban, A. Veziridis, A. Weidenkaff, M. Muralidhar, M. Murakami, S. Abel, J. Fompeyrine, J. Zuniga-Perez, R. Ramesh, N. A. Spaldin, S. Ostanin, V. Borisov, I. Mertig, V. Lazenka, G. Srinivasan, W. Prellier, M. Uchida, M. Kawasaki, R. Pentcheva, P. Gegenwart, F. Miletto Granozio, J. Fontcuberta and N. Pryds, *Journal of Physics D: Applied Physics*, 2016, **49**, 433001.
- [6] M. Coll, J. Fontcuberta, M. Althammer, M. Bibes, H. Boschker, A. Calleja, G. Cheng, M. Cuoco, R. Dittmann, B. Dkhil, I. El Baggari, M. Fanciulli, I. Fina, E. Fortunato, C. Frontera, S. Fujita, V. Garcia, S. Goennenwein, C.-G. Granqvist, J. Grollier, R. Gross, A. Hagfeldt, G. Herranz, K. Hono, E. Houwman, M. Huijben, A. Kalaboukhov, D. Keeble, G. Koster,

- L. Kourkoutis, J. Levy, M. Lira-Cantu, J. MacManus-Driscoll, J. Mannhart, R. Martins, S. Menzel, T. Mikolajick, M. Napari, M. Nguyen, G. Niklasson, C. Paillard, S. Panigrahi, G. Rijnders, F. Sánchez, P. Sanchis, S. Sanna, D. Schlom, U. Schroeder, K. Shen, A. Siemon, M. Spreitzer, H. Sukegawa, R. Tamayo, J. van den Brink, N. Pryds and F. M. Granozio, *Applied Surface Science*, 2019, **482**, 1–93.
- [7] A. Ohtomo and H. Y. Hwang, *Nature*, 2004, **427**, 423.
- [8] B. R. K. Nanda and S. Satpathy, *Physical Review B*, 2010, **81**, 224408.
- [9] Y. Hotta, T. Susaki and H. Y. Hwang, *Physical Review Letters*, 2007, **99**, 236805.
- [10] D. G. Schlom, L.-Q. Chen, C.-B. Eom, K. M. Rabe, S. K. Streiffer and J.-M. Triscone, *Annual Review of Materials Research*, 2007, **37**, 589–626.
- [11] J. H. Haeni, P. Irvin, W. Chang, R. Uecker, P. Reiche, Y. L. Li, S. Choudhury, W. Tian, M. E. Hawley, B. Craigo, A. K. Tagantsev, X. Q. Pan, S. K. Streiffer, L. Q. Chen, S. W. Kirchoefer, J. Levy and D. G. Schlom, *Nature*, 2004, **430**, 758–761.
- [12] R. Bachelet, F. Sánchez, J. Santiso, C. Munuera, C. Ocal and J. Fontcuberta, *Chemistry of Materials*, 2009, **21**, 2494–2498.
- [13] J. E. Kleibeuker, G. Koster, W. Siemons, D. Dubbink, B. Kuiper, J. L. Blok, C. H. Yang, J. Ravichandran, R. Ramesh, J. E. Ten Elshof, D. H. Blank and G. Rijnders, *Advanced Functional Materials*, 2010, **20**, 3490–3496.
- [14] B. Kuiper, J. L. Blok, H. J. Zandvliet, D. H. Blank, G. Rijnders and G. Koster, *MRS Communications*, 2011, **1**, 17–21.
- [15] H. Zheng, J. Wang, L. Mohaddes-Ardabili, M. Wuttig, L. Salamanca-Riba, D. G. Schlom and R. Ramesh, *Applied Physics Letters*, 2004, **85**, 2035–2037.
- [16] H. Zheng, F. Straub, Q. Zhan, P. Yang, W. Hsieh, F. Zavaliche, Y. Chu, U. Dahmen and R. Ramesh, *Advanced Materials*, 2006, **18**, 2747–2752.

- [17] P. Moetakef, T. A. Cain, D. G. Ouellette, J. Y. Zhang, D. O. Klenov, A. Janotti, C. G. Van de Walle, S. Rajan, S. J. Allen and S. Stemmer, *Applied Physics Letters*, 2011, **99**, 232116.
- [18] C. He, T. D. Sanders, M. T. Gray, F. J. Wong, V. V. Mehta and Y. Suzuki, *Physical Review B*, 2012, **86**, 081401.
- [19] W. Siemons, G. Koster, H. Yamamoto, W. A. Harrison, G. Lucovsky, T. H. Geballe, D. H. A. Blank and M. R. Beasley, *Physical Review Letters*, 2007, **98**, 196802.
- [20] G. Herranz, M. Basletić, M. Bibes, C. Carrétéro, E. Tafra, E. Jacquet, K. Bouzehouane, C. Deranlot, A. Hamzić, J.-M. Broto, A. Barthélémy and A. Fert, *Physical Review Letters*, 2007, **98**, 216803.
- [21] Y. Li, S. N. Phattalung, S. Limpijumnong, J. Kim and J. Yu, *Physical Review B*, 2011, **84**, 245307.
- [22] A. Kalabukhov, R. Gunnarsson, J. Börjesson, E. Olsson, T. Claeson and D. Winkler, *Physical Review B*, 2007, **75**, 121404.
- [23] M. Yazdi-Rizi, P. Marsik, B. P. P. Mallett, K. Sen, A. Cerreta, A. Dubroka, M. Scigaj, F. Sánchez, G. Herranz and C. Bernhard, *Physical Review B*, 2017, **95**, 195107.
- [24] N. Nakagawa, H. Y. Hwang and D. A. Muller, *Nature Materials*, 2006, 204–209.
- [25] A. Savoia, D. Paparo, P. Perna, Z. Ristic, M. Salluzzo, F. Miletto Granozio, U. Scotti di Uccio, C. Richter, S. Thiel, J. Mannhart and L. Marrucci, *Physical Review B*, 2009, **80**, 075110.
- [26] M. L. Reinle-Schmitt, C. Cancellieri, D. Li, D. Fontaine, M. Medarde, E. Pomjakushina, C. W. Schneider, S. Gariglio, P. Ghosez, J. M. Triscone and P. R. Willmott, *Nature Communications*, 2012, **3**, 932.
- [27] N. Reyren, S. Thiel, A. D. Caviglia, L. F. Kourkoutis, G. Hammerl, C. Richter, C. W. Schneider, T. Kopp, A.-S. Rüetschi, D. Jaccard,

- M. Gabay, D. A. Muller, J.-M. Triscone and J. Mannhart, *Science*, 2007, **317**, 1196–1199.
- [28] E. Pfeiffer and J. Schooley, *Physics Letters A*, 1969, **29**, 589–590.
- [29] J. F. Schooley, W. R. Hosler, E. Ambler, J. H. Becker, M. L. Cohen and C. S. Koonce, *Physical Review Letters*, 1965, **14**, 305–307.
- [30] W. Qing-Yan, L. Zhi, Z. Wen-Hao, Z. Zuo-Cheng, Z. Jin-Song, L. Wei, D. Hao, O. Yun-Bo, D. Peng, C. Kai, W. Jing, S. Can-Li, H. Ke, J. Jin-Feng, J. Shuai-Hua, W. Ya-Yu, W. Li-Li, C. Xi, M. Xu-Cun and X. Qi-Kun, *Chinese Physics Letters*, 2012, **29**, 037402.
- [31] J.-F. Ge, Z.-L. Liu, C. Liu, C.-L. Gao, D. Qian, Q.-K. Xue, Y. Liu and J.-F. Jia, *Nature Materials*, 2015, **14**, 285–289.
- [32] J. J. Lee, F. T. Schmitt, R. G. Moore, S. Johnston, Y.-T. Cui, W. Li, M. Yi, Z. K. Liu, M. Hashimoto, Y. Zhang, D. H. Lu, T. P. Devereaux, D.-H. Lee and Z.-X. Shen, *Nature*, 2014, **515**, 245–248.
- [33] C. Cancellieri, A. S. Mishchenko, U. Aschauer, A. Filippetti, C. Faber, O. S. Barišić, V. A. Rogalev, T. Schmitt, N. Nagaosa and V. N. Strocov, *Nature Communications*, 2016, **7**, 10386.
- [34] J. Zaanen, *Nature*, 2014, **515**, 205–206.
- [35] K. A. Müller and A. Shengelaya, *J. Supercond Nov. Magn.*, 2013, **26**, 491.
- [36] K. A. Müller, *Journal of Physics: Condensed Matter*, 2007, **19**, 251002.
- [37] H. Keller, A. Bussmann-Holder and K. A. Müller, *Materials Today*, 2008, **11**, 38–46.
- [38] H. Keller and A. Bussmann-Holder, *Advances in Condensed Matter Physics*, 2010, **2010**, 1–17.
- [39] A. Shengelaya and K. A. Müller, *Europhysics Letters*, 2015, **109**, 27001.
- [40] D. Mihailovic, V. V. Kabanov and K. A. Müller, *Europhysics Letters*, 2002, **57**, 254–259.

- [41] L. Keldysh, *Pis'ma Zh. Eksp. Teor. Fiz.*, 1979, **29**, 716.
- [42] Y. Sassa, M. Radović, M. Månsson, E. Razzoli, X. Y. Cui, S. Pailhès, S. Guerrero, M. Shi, P. R. Willmott, F. Miletto Granozio, J. Mesot, M. R. Norman and L. Patthey, *Physical Review B*, 2011, **83**, 140511.
- [43] M. Caputo, M. Boselli, A. Filippetti, S. Lamal, D. Li, A. Chickina, C. Cancellieri, T. Schmitt, J.-M. Triscone, P. Ghosez, S. Gariglio and V. N. Strocov, *arXiv*, 2019, 1.
- [44] C. Ma and C. Chen, in *Advanced Nano Deposition Methods*, ed. Y. Lin and X. Chen, Wiley-VCH, 2016, ch. ch.1, pp. 1–25.
- [45] W. Wunderlich, *Metals*, 2014, **4**, 410–427.
- [46] G. J. Rijnders, G. Koster, D. H. Blank and H. Rogalla, *Materials Science and Engineering: B*, 1998, **56**, 223 – 227.
- [47] M. Kawasaki, K. Takahashi, T. Maeda, R. Tsuchiya, M. Shinohara, O. Ishiyama, T. Yonezawa, M. Yoshimoto and H. Koinuma, *Science*, 1994, **266**, 1540–1542.
- [48] G. Koster, B. L. Kropman, G. J. H. M. Rijnders, D. H. A. Blank and H. Rogalla, *Applied Physics Letters*, 1998, **73**, 2920–2922.
- [49] J. Huijbregtse, J. Rector and B. Dam, *Physica C: Superconductivity*, 2001, **351**, 183.
- [50] F. Gellé, R. Chirita, D. Mertz, M. V. Rastei, A. Dinia and S. Colis, *Surface Science*, 2018, **677**, 38.
- [51] K. Szot and W. Speier, *Physical Review B*, 1999, **60**, 5909–5926.
- [52] Y. Liang and D. A. Bonnelli, *Surface Science*, 1994, **310**, 128 – 134.
- [53] R. Bachelet, F. Sánchez, F. J. Palomares, C. Ocal and J. Fontcuberta, *Applied Physics Letters*, 2009, **95**, 141915.
- [54] J. A. Greer, *Journal of Vacuum Science & Technology A: Vacuum, Surfaces, and Films*, 1992, **10**, 1821–1826.

- [55] G. J. H. M. Rijnders, G. Koster, D. H. A. Blank and H. Rogalla, *Applied Physics Letters*, 1997, **70**, 1888–1890.
- [56] G. Rijnders, S. Currás, M. Huijben, D. H. A. Blank and H. Rogalla, *Applied Physics Letters*, 2004, **84**, 1150–1152.
- [57] M. Huijben, G. Koster, D. H. A. Blank and G. Rijnders, *Phase Transitions*, 2008, **81**, 703.
- [58] A. Walkenhorst, C. Doughty, X. X. Xi, S. N. Mao, Q. Li, T. Venkatesan and R. Ramesh, *Applied Physics Letters*, 1992, **60**, 1744–1746.
- [59] G. Koster, in *In Situ Characterization of Thin Film Growth*, ed. G. Koster and G. Rijnders, Woodhead Publishing, 2011, ch. 1, pp. 3 – 28.
- [60] C. Buzea and K. Robbie, *Reports on Progress in Physics*, 2005, **68**, 385–409.
- [61] M. Birkholz, *Thin Film Analysis by X-Ray Scattering*, Wiley VCH, 2005, p. 191.
- [62] B. Warren, *X-Ray Diffraction*, addison wesley, 1969.
- [63] J. Ye and K. Nakamura, *Physical Review B*, 1993, **48**, 7554–7564.
- [64] R. Liang, D. A. Bonn and W. N. Hardy, *Physical Review B*, 2006, **73**, 180505.
- [65] C. Cancellieri, *Ph.D. thesis*, École polytechnique fédérale de Lausanne, 2008.
- [66] X.-Y. Zheng, D. H. Lowndes, S. Zhu, J. D. Budai and R. J. Warmack, *Physical Review B*, 1992, **45**,.
- [67] G. Koster, J. Heutink, B. L. Kropman, G. J. H. M. Rijnders, D. H. A. Blank and H. Rogalla, *Inst. Phys. Conf. Ser.*, 1997, 181.
- [68] L. van der Pauw, *Philips Res. Rep.*, 1958, **13**,.
- [69] I. Miccoli, F. Edler, H. Pfnür and C. Tegenkamp, *Journal of Physics: Condensed Matter*, 2015, **27**, 223201.

- [70] J. Garcia-Barriocanal, A. M. Perez-Muñoz, Z. Sefrioui, D. Arias, M. Varela, C. Leon, S. J. Pennycook and J. Santamaria, *Physical Review B*, 2013, **87**, 245105.
- [71] J. G. Wen, C. Traehold and H. W. Zandbergen, *Physica C*, 1993, **205**, 354.
- [72] S. Kevan, *Angle-Resolved Photoemission, Theory and Current Applications*, Elsevier Science, 1992.
- [73] S. Hüfner, *Photoelectron Spectroscopy*, Springer, 1996.
- [74] Z.-X. Shen, D. S. Dessau, B. O. Wells, D. M. King, W. E. Spicer, A. J. Arko, D. Marshall, L. W. Lombardo, A. Kapitulnik, P. Dickinson, S. Doniach, J. DiCarlo, T. Loeser and C. H. Park, *Phys. Rev. Lett.*, 1993, **70**, 1553–1556.
- [75] A. Damascelli, Z. Hussain and Z.-X. Shen, *Review of Modern Physics*, 2003, **75**, 473.
- [76] M. P. Seah and W. A. Dench, *Surf. Inter. Anal.*, 1979, **1**, 2–11.
- [77] J. Yeh and I. Lindau, *Atomic Data and Nuclear Data Tables*, 1985, **32**, 1 – 155.
- [78] P. Willmott, in *An Introduction to Synchrotron Radiation: Techniques and Applications*, John Wiley and Sons, Ltd, 2011, ch. 3, p. 39.
- [79] V. N. Strocov, T. Schmitt, U. Flechsig, T. Schmidt, A. Imhof, Q. Chen, J. Raabe, R. Betemps, D. Zimoch, J. Krempasky, X. Wang, M. Grioni, A. Piazzalunga and L. Patthey, *J. Synch. Rad.*, 2010, **17**, 631–643.
- [80] V. N. Strocov, X. Wang, M. Shi, M. Kobayashi, J. Krempasky, C. Hess, T. Schmitt and L. Patthey, *J. Synch. Rad.*, 2014, **21**, 32–44.
- [81] M. A. Hossain, J. D. F. Mottershead, D. Fournier, A. Bostwick, J. L. McChesney, E. Rotenberg, R. Liang, W. N. Hardy, G. A. Sawatzky, I. S. Elfimov, D. A. Bonn and A. Damascelli, *Nature Physics*, 2008, **4**, 527–531.

- [82] C. Cancellieri, M. L. Reinle-Schmitt, M. Kobayashi, V. N. Strocov, T. Schmitt, P. R. Willmott, S. Gariglio and J.-M. Triscone, *Physical Review Letters*, 2013, **110**, 137601.
- [83] J. C. Campuzano, G. Jennings, M. Faiz, L. Beaulaigue, B. W. Veal, J. Z. Liu, A. P. Paulikas, K. Vandervoort, H. Claus, R. S. List, A. J. Arko and R. J. Bartlett, *Physical Review Letters*, 1990, **64**, 2308–2311.
- [84] M. C. Schabel, C.-H. Park, A. Matsuura, Z.-X. Shen, D. A. Bonn, R. Liang and W. N. Hardy, *Physical Review B*, 1998, **57**, 6090–6106.
- [85] D. H. Lu, D. L. Feng, N. P. Armitage, K. M. Shen, A. Damascelli, C. Kim, F. Ronning, Z. X. Shen, D. A. Bonn, R. Liang, W. N. Hardy, A. I. Rykov and S. Tajima, *Physical Review Letters*, 2001, **86**, 4370–4373.
- [86] K. Nakayama, T. Sato, K. Terashima, H. Matsui, T. Takahashi, M. Kubota, K. Ono, T. Nishizaki, Y. Takahashi and N. Kobayashi, *Physical Review B*, 2007, **75**, 1–7.
- [87] V. B. Zabolotnyy, S. V. Borisenko, A. A. Kordyuk, J. Geck, D. S. Inosov, A. Koitzsch, J. Fink, M. Knupfer, B. Büchner, S. L. Drechsler, H. Berger, A. Erb, M. Lambacher, L. Patthey, V. Hinkov and B. Keimer, *Physical Review B*, 2007, **76**, –6.
- [88] K. Nakayama, T. Sato, K. Terashima, T. Arakane, T. Takahashi, M. Kubota, K. Ono, T. Nishizaki, Y. Takahashi and N. Kobayashi, *Physical Review B*, 2009, **79**, 2–5.
- [89] V. B. Zabolotnyy, A. A. Kordyuk, D. Evtushinsky, V. N. Strocov, L. Patthey, T. Schmitt, D. Haug, C. T. Lin, V. Hinkov, B. Keimer, B. Büchner and S. V. Borisenko, *Physical Review B*, 2012, **85**, 064507.
- [90] H. Iwasawa, N. B. M. Schröter, T. Masui, S. Tajima, T. K. Kim and M. Hoesch, *Physical Review B*, 2018, **98**, 081112.
- [91] H. L. Edwards, J. T. Markert and A. L. de Lozanne, *Physical Review Letters*, 1992, 2967–2970.

- [92] M. Maki, T. Nishizaki, K. Shibata and N. Kobayashi, *Journal of the Physical Society of Japan*, 2001, **70**, 1877–1880.
- [93] Y. Sassa, *Ph.D. thesis*, Institut de Physique de l'Universite de Neuchatel, 2011.
- [94] C. Cancellieri, M. L. Reinle-Schmitt, M. Kobayashi, V. N. Strocov, P. R. Willmott, D. Fontaine, P. Ghosez, A. Filippetti, P. Delugas and V. Fiorentini, *Physical Review B*, 2014, **89**, 121412.
- [95] A. Jablonski and C. J. Powell, *Surface and Interface Analysis*, 1993, **20**, 771–786.
- [96] S. Tanuma, C. Powell and D. Penn, *Surface Science*, 1987, **192**, 849–857.
- [97] S. Tanuma, C. J. Powell and D. R. Penn, *Surf. Inter. Anal.*, 1991, **17**, 911–926.
- [98] S. Tanuma, C. J. Powell and D. R. Penn, *Surf. Inter. Anal.*, 1994, **21**, 165–176.
- [99] S. Tanuma, C. J. Powell and D. R. Penn, *Surface and Interface Analysis*, 2011, **43**, 689–713.
- [100] C. J. Powell and A. Jablonski, *NIST Electron Inelastic-Mean-Free-Path Database - Version 1.2*, National Institute of Standards and Technology, 2010.
- [101] P. Giannozzi, S. Baroni, N. Bonini, M. Calandra, R. Car, C. Cavazzoni, D. Ceresoli, G. L. Chiarotti, M. Cococcioni, I. Dabo, A. Dal Corso, S. de Gironcoli, S. Fabris, G. Fratesi, R. Gebauer, U. Gerstmann, C. Gougoussis, A. Kokalj, M. Lazzeri, L. Martin-Samos, N. Marzari, F. Mauri, R. Mazzarello, S. Paolini, A. Pasquarello, L. Paulatto, C. Sbraccia, S. Scandolo, G. Sclauzero, A. P. Seitsonen, A. Smogunov, P. Umari and R. M. Wentzcovitch, *J. Phys.: Conden. Matter*, 2009, **21**, 395502.
- [102] P. Giannozzi, O. Andreussi, T. Brumme, O. Bunau, M. Buongiorno Nardelli, M. Calandra, R. Car, C. Cavazzoni, D. Ceresoli, M. Cococcioni,

- N. Colonna, I. Carnimeo, A. Dal Corso, S. de Gironcoli, P. Delugas, R. A. DiStasio, A. Ferretti, A. Floris, G. Fratesi, G. Fugallo, R. Gebauer, U. Gerstmann, F. Giustino, T. Gorni, J. Jia, M. Kawamura, H.-Y. Ko, A. Kokalj, E. Küçükbenli, M. Lazzeri, M. Marsili, N. Marzari, F. Mauri, N. L. Nguyen, H.-V. Nguyen, A. Otero-de-la Roza, L. Paulatto, S. Poncé, D. Rocca, R. Sabatini, B. Santra, M. Schlipf, A. P. Seitsonen, A. Smogunov, I. Timrov, T. Thonhauser, P. Umari, N. Vast, X. Wu and S. Baroni, *J. Phys.: Condens. Matter*, 2017, 465901.
- [103] A. Dal Corso, *Computational Materials Science*, 2014, **95**, 337–350.
- [104] J. P. Perdew, K. Burke and M. Ernzerhof, *Physical Review Letters*, 1996, **77**, 3865–3868.
- [105] Z. Wang, S. Tsukimoto, M. Saito and Y. Ikuhara, *Journal of Applied Physics*, 2009, **106**, 093714.
- [106] I. S. Elfimov, G. A. Sawatzky and A. Damascelli, *Physical Review B*, 2008, **77**, 060504.
- [107] N. Plumb, M. Kobayashi, M. Salluzzo, E. Razzoli, C. Matt, V. Strocov, K. Zhou, M. Shi, J. Mesot, T. Schmitt, L. Patthey and M. Radović, *Applied Surface Science*, 2017, **412**, 271 – 278.
- [108] A. Chikina, F. Lechermann, M.-A. Husanu, M. Caputo, C. Cancellieri, X. Wang, T. Schmitt, M. Radovic and V. N. Strocov, *ACS Nano*, 2018, **12**, 7927–7935.
- [109] S. Hüfner, in *Photoelectron Spectroscopy*, Springer, 2003, ch. 5, p. 244.
- [110] T. Iyasu, K. Tamura, R. Shimizu, M. A. Vlaicu and H. Yoshikawa, *Applied Surface Science*, 2006, **252**, 4335–4339.
- [111] M. Salluzzo, J. C. Cezar, N. B. Brookes, V. Bisogni, G. M. De Luca, C. Richter, S. Thiel, J. Mannhart, M. Huijben, A. Brinkman, G. Rijnders and G. Ghiringhelli, *Physical Review Letters*, 2009, **102**, 166804.
- [112] G.-z. Zhu, G. Radtke and G. A. Botton, *Nature*, 2012, **490**, 384–387.

- [113] T. Höche, M. Grodzicki, F. Heyroth and P. A. van Aken, *Physical Review B*, 2005, **72**, 205111.
- [114] F. Sánchez, C. Ocal and J. Fontcuberta, *Chem. Soc. Rev.*, 2014, **43**, 2272–2285.
- [115] C. Baeumer, C. Xu, N. Raab, R. A. Heinen, A. Koehl, R. Dittmann and F. Gunkel, *Scientific Reports*, 2015, 11829.
- [116] O. E. Dagdeviren, G. H. Simon, K. Zou, F. J. Walker, C. Ahn, E. I. Altman and U. D. Schwarz, *Physical Review B*, 2016, **93**, 195303.
- [117] K. Iwahori, S. Watanabe, M. Kawai, K. Mizuno, K. Sasaki and M. Yoshimoto, *Journal of Applied Physics*, 2000, **88**, 7099–7103.
- [118] G. Rijnders, G. Koster, V. Leca, D. H. Blank and H. Rogalla, *Applied Surface Science*, 2000, **168**, 223 – 226.
- [119] W. Gerlach, *Zeitschrift für Physik*, 1922, **9**, 184–192.
- [120] W. Primak, H. Kaufman and R. Ward, *Journal of the American Chemical Society*, 1948, **70**, 2043–2046.
- [121] O. Maksimov, V. D. Heydemann, P. Fisher, M. Skowronski and P. a. Salvador, *Applied Physics Letters*, 2006, **89**, 4–7.
- [122] R. Takahashi, Y. Matsumoto, T. Ohsawa, M. Lippmaa, M. Kawasaki and H. Koinuma, *Journal of Crystal Growth*, 2002, **234**, 505 – 508.
- [123] S. Migita, Y. Kasai and S. Sakai, *Journal of Low Temperature Physics*, 1996, **105**, 1337–1342.
- [124] D. Li, S. Gariglio, C. Cancellieri, A. Fête, D. Stornaiuolo and J.-M. Triscone, *APL Materials*, 2014, **2**, 012102.
- [125] S. P, *Chemische Technologie in Einzeldarstellungen*, 1918, 98–100.
- [126] J. H. Haeni, C. D. Theis and D. G. Schlom, *Journal of Electroceramics*, 2000, **4**, 385–391.

- [127] A. Herklotz, K. Dörr, T. Z. Ward, G. Eres, H. M. Christen and M. D. Biegalski, *Applied Physics Letters*, 2015, **106**, 131601.
- [128] D. J. Groenendijk and S. Gariglio, *Journal of Applied Physics*, 2016, **120**, 225307.
- [129] H. Y. Sun, Z. W. Mao, T. W. Zhang, L. Han, T. T. Zhang, X. B. Cai, X. Guo, Y. F. Li, Y. P. Zang, W. Guo, J. H. Song, D. X. Ji, C. Y. Gu, C. Tang, Z. B. Gu, N. Wang, Y. Zhu, D. G. Schlom, Y. F. Nie and X. Q. Pan, *Nature Communications*, 2018, **9**, 2965.
- [130] J. G. Bednorz and K. A. Müller, *Phys. Rev. Lett.*, 1984, **52**, 2289.
- [131] R. Kind and K. A. Müller, *Communications on Physics*, 1976, **1**, 223.
- [132] J. Toulouse, X. M. Wang, L. A. Knauss and L. A. Boatner, *Physical Review B*, 1991, **43**, 8297–8302.
- [133] J.-P. Locquet, J. Perret, J. Fompeyrine, E. Mächler, J. W. Seo and G. Van Tendeloo, *Nature*, 1998, **394**, 453–456.
- [134] M. Abrecht, D. Ariosa, D. Cloetta, S. Mitrovic, M. Onellion, X. X. Xi, G. Margaritondo and D. Pavuna, *Phys. Rev. Lett.*, 2003, **91**, 057002.
- [135] D. Cloetta, D. Ariosa, C. Cancellieri, M. Abrecht, S. Mitrovic and D. Pavuna, *Phys. Rev. B*, 2006, **74**, 014519.

Acknowledgement

I would like to thank all the people who helped me in the realization of this work.

First, I would like to thank to Prof. Gian-Luca Bona, who gave me the opportunity to do this PhD and who was always charging me with encouragement and motivation. I thank to Urs Sennhauser and Michel Calame for giving me possibility to do experiments at the Transport at Nanoscale Interfaces Laboratory, at Empa, Dübendorf.

I would like to express my sincere thanks to Fabio La Mattina who was always next to me in all stages of my PhD. He was teaching me everything in science and beyond. Fabio, thank you for all you have done for me. I am also grateful to Claudia Cancellieri, for being always ready to help me and actually doing this.

I would express thanks to Prof. Karl Alex Müller and Dr. Georg Bednorz, for their interest in this topic, and I thank to Prof. Alexander Shengelaya, who was my mentor from my first year in physics course at Tbilisi State University, until my master, and who strongly contributed to my PhD study as well.

I thank to "ARPES people", Vladimir Stokov, Alla Chikina and Marco Caputo, for their support in conducting experiments at the synchrotron beamline and understanding data. I would like to thank to Daniele Passerone, Carlo Pignedoli and Marta Bon for DFT calculations, Marta Rossel and Rolf Erni for TEM and André Kupferschmid and Rico Muff, for providing LabVIEW software for RHEED and dielectric measurements. I thank to Ronald Grundbacher and Steffen Reidt for their help in BRNC clean room.

I want to thank to Ivan Shorubalko, who has a magical talent in motivating people (at least, it worked for me), and "Ivan's group": Rolf, Huan, Gökhan,

Matthias and Dominik. I thank to Huan for TEM and SEM analysis. Gökhan, Matthias and Rolf for their help in translating abstract to German and for the correction of the thesis text. Further, I thank to my past and present officemates: Donat, Lorenzo, Davide, and in particular Elena and Nadia, who brought new life to our office. I am grateful to all the people from lab 405 for the pleasant years we spent together.

I also want to thank to the users of Forum.ge, physics.stackexchange.com and other Q&A sites. The people I have never met but who helped me a lot in understanding many unclear phenomena of solid-state physics.

Here I have to mention my friends in Georgia: Sandro, Vakho, Giorgi, Mamuka who were continuously asking me if I have discovered room temperature superconductor. Special thanks to Sandro for shearing his experience and cheering me up 24/7.

Finally, I must express my gratitude to my family in Georgia, to my parents and to my wife, Salome, for providing me constant support and continuous encouragement throughout my years of PhD study.

Curriculum vitae

Tornike Gagnidze

Date of birth: 22. 01. 1991

Place of birth: Tbilisi, Georgia

Nationality: Georgian

Education

2015-... , PhD student, Transport at nanoscale interfaces laboratory, Empa, Dübendorf

2012-2014 , Master of Physics, Ivane Javakhishvili Tbilisi State University, Georgia

2008-2012 , Bachelor of Physics, Ivane Javakhishvili Tbilisi State University, Georgia

Summer Schools and Internships

2016 Intensive course in Electron microscopy, Empa Thun, Switzerland

2015 School of Superconductivity in Iron-Based Materials, Salerno, Italy

2013 -2014 Junior Engineer, Institute of Micro and Nano Electronics, Tbilisi, Georgia.

2010 Intern researcher, Centre for Research on Adaptive Nanostructures and Nanodevices, Dublin, Ireland

Conferences:

2018 October: International Workshop on Oxide Electronics, Les Diablerets, Switzerland.

Poster: Study of structural properties of ultrathin SrO films deposited on SrTiO₃

2018 August: Swiss Workshop on Materials with Novel Electronic Properties, Les Diablerets, Switzerland

Poster: Highly Strained SrO Nano-domains

2017 Gettering and Defect Engineering in Semiconductor Technology - GADEST.

Poster: Study of fully epitaxial YBa₂Cu₃O_{7-δ} /SrTiO₃ heterostructures.

List of Publications:

1. Paper I: T. Gagnidze, H. Ma, C. Cancellieri, G-L. Bona and F. La Mattina, "Structural properties of ultra-thin SrO film deposited on SrTiO₃", Sci. Tech. Adv. Mater.,20,456, 2019
2. Paper II: H. Ma, T. Gagnidze, B. Walfort, M. D. Rossell, C. Cancellieri, I. Shorubalko, F. La Mattina Direct-epitaxial growth of SrAl₂O₄:Eu,Dy thin films on Al₂O₃ substrate by pulsed laser deposition, Applied Surface Science. 491, 53, (2019)
3. Paper III: T. Gagnidze, C. Cancellieri, H. Ma, A. Filippetti, V. Strocov, A. Chikina, M. Caputo, R. Erni, M. Rossel, M. Bon, C. Pigendoli, D. Passarone, A. Shengelaya, G-L Bona, and F. La Mattina, "Structural reconstruction at buried SrTiO₃/YBa₂Cu₃O_{7-δ} interface" (in preparation)